universität wien

DISSERTATION / DOCTORAL THESIS

Titel der Dissertation /Title of the Doctoral Thesis

„Molecular anions as a coolant for antimatter experiments“

verfasst von / submitted by

Julian Valentin Fesel, MSc

angestrebter akademischer Grad / in partial fulfilment of the requirements for the degree of

Doktor der Naturwissenschaften (Dr. rer. nat.)

Wien, 2019 / Vienna 2019

Studienkennzahl lt. Studienblatt / degree programme code as it appears on the student record sheet:	A 796 605 411
Dissertationsgebiet lt. Studienblatt / field of study as it appears on the student record sheet:	Physik
Betreut von / Supervisor:	Univ.-Prof. Dr. Markus Aspelmeyer Dr. Michael Doser

This page is actually not completely blank.

Abstract

The topics of this thesis describe the effort that was made towards laser cooling of anions, with the goal to use them as a sympathetic coolant for antiprotons in a Penning trap. It covers a theoretical analysis of the requirements and the expected performance of different cooling schemes, as well as a report on efforts towards an experimental realisation. The focus is on the molecular anion species C_2^-, which was chosen due to a recent survey of possible molecular candidates and the challenges which arise in the use of atomic anions (Yzombard et al., 2015).

After an introduction to the topic, some general properties of anionic molecules are discussed, including their electronic level structure. The theory behind the interaction of light with molecules is presented, to the extent relevant for the later sections. This then leads to a more detailed presentation of the specific case of C_2^-, with a focus on the levels and transitions which are interesting for laser cooling. Simulations of different laser cooling schemes are then presented. These were done on the basis of a GPU accelerated C++ code, which is designed for the simulation of particles in a Penning trap (Van Gorp et al., 2011; Van Gorp and Dupre, 2013), and which was customised to include the interaction of the molecules with the laser. The simulations led to two publications (Fesel et al., 2017; Gerber et al., 2018), which are reproduced in sections 2.5.1 and 2.5.2. A discussion and comparison of the results which were found is presented in section 2.6. The discussion aims at giving the reader an overview of the challenges and prospects, which are to be expected with laser cooling of C_2^-.

Chapter 3 then describes the experimental work that was done. The main topic is the setup for a C_2^- source which was built. This is based on the use of a commercial supersonic expansion valve (SSEV) and a subsequent dielectric barrier discharge (DBD) (Even, 2015). The DBD is then used to ionise a gas mixture of acetylene in a noble carrier. The produced anions are accelerated and then mass selected with the help of a Wien filter. A detailed description of the setup is given (see figure 3.1 for an overview), followed by a presentation of the results. Here, a mass spectrum is presented, showing the successful production of anions with a mass of 24 u, which corresponds to C_2^-.

Additionally, the setup foresees a possibility for photodetachment spectroscopy on the produced anions. To this end, an optical resonator was built, which allows to enhance the light intensity of a 399 nm laser, while also allowing the transmission of 2.54 µm light. This allows for resonant stimulation of C_2^-. The optical setup for the frequency stabilisation of the laser to the resonator is presented (see figure 3.6 for an overview), followed by a presentation of the experimental results on the device. This includes a determination of the resonators finesse to $\mathcal{F} = (12800 \pm 700)$ and a verification of the stability of the laser lock during the operation of the C_2^- source. Finally in chapter 4, a conclusion is given, which summarises the work described by this thesis and includes

an outlook on the upcoming steps.

Acknowledgements

Even though it is not always visible in the text, I enjoyed substantial support while performing the work for this thesis. I therefore want to use this section, to give credit to at least some of the people who helped me along the way. For this, I created a small list of all the names that came to my mind, alongside a short description of some of their good deeds. I hope, that these people take delight in finding their names in this section, together with "*best wishes and many thanks*" from my side.

Markus Aspelmeyer: For accepting the responsibility of being the university based supervisor in an unusual constellation (on short notice!) and for helpful advice.

Ruggero Caravita: For several helpful discussions.

Giovanni Cerchiari: For his help with choosing the right FPGA.

Daniel Comparat: For many helpful discussions and several enlightening emails.

Hao Cui: For his help in extending the Simbuca code, all the interesting questions and for teaching me some Chinese.

Uros Delic: For his help with the optical resonator.

Michael Doser: For offering me the chance to work at CERN, a lot of helpful advice and "lightning–speed signing" of my orders.

Martin Fuchs: For his enthusiastic teaching, which led me to study physics.

Sebastian Gerber: For his pragmatic attitude, always pushing me and the project forward and for proofreading this thesis.

Stefan Haider: For all his advice and help with the technical problems of the setup, as well as the free coffee.

Alexander Hinterberger: For all the times where he was "the man doing the heavy lifting".

Nikolai Kiesel: For his help in designing the optical resonator.

Emanuel Oswald: For his help in understanding the mass spectrum, as well as many heated discussions about stock markets.

Forgotten Person: For forgiving me that I forgot to mention him/her here and of course for all the help.

Jacky Rochet: For his help with the mechanical design of the C_2^- source.

Pauline Yzombard: For helpful discussions.

Christian Zimmer: For proofreading this thesis, which led to a significant improvement of the text, as well as for opening the window after cooking in the microwave.

Table of contents

1. Introduction and motivation

CERN, Europe's largest institution for fundamental particle research, is host to a range of experiments on antimatter, based at the so–called *antimatter factory* on its main campus. The goal is to shed light on the observed lack of antimatter in our universe. It is the general assumption, that this stems from an asymmetry in the laws of nature on the level of elementary particle interaction, which is substantiated by the already discovered violations of parity (P) and charge–parity (CP) invariance. Nevertheless, the findings so far are not sufficient to explain the baryon density observed in the universe. For this reason, there is an ongoing search for further asymmetries, with violations of charge–parity–time (CPT) invariance being among the possible candidates (Canetti et al., 2012; Vargas, 2018). The validity of this invariance in physical theories is called the CPT–theorem, and one of its consequences is that particles and their associated antiparticles must have the same mass and lifetime, while having a magnetic moment and charge of opposite sign and equal absolute value. By measuring and comparing these properties one can therefore search for violations of the CPT–theorem (Griffiths, 2008). At CERN's antimatter factory this is done with a focus on antiprotons and antihydrogen. The research is enabled by the unique infrastructure present at CERN. A pre–accelerator of the Large Hadron Collider (LHC) provides high energy protons, which are shot at an Iridium target and create antiprotons via pair production:

$$\underbrace{\mathrm{p}}_{26\,\mathrm{GeV}} + \underbrace{\mathrm{p}}_{\mathrm{Ir-target}} \rightarrow \mathrm{p} + \mathrm{p} + \mathrm{p} + \bar{\mathrm{p}}. \tag{1.1}$$

The emerging antiprotons have an energy around 3.6 GeV and need to be slowed down in order to be useful for precision measurements. This is done by a machine called the antiproton decelerator (AD) which is a synchrotron that, in combination with stochastic and electron cooling, is able to reduce the antiproton kinetic energy to 5.3 MeV. A bunch of $> 3 \times 10^7$ antiprotons every 100 s is then distributed to one of the connected experiments. By trapping the antiprotons in Penning traps, several important milestones have already been achieved at this facility. This includes the first production of low energy antihydrogen by the ATHENA and ATRAP collaborations (Amoretti et al., 2002; Gabrielse et al., 2002), the first observation of the 1S–2S transition of antihydrogen by the ALPHA collaboration (Ahmadi et al., 2018a; Ahmadi et al., 2018b), spectroscopy on antiprotonic helium by the ASACUSA collaboration (Hori et al., 2016) and precision measurements on antiprotons by the BASE collaboration (Sellner et al., 2017; Smorra et al., 2017; Ulmer et al., 2015). Given that there is so far no combined theory of gravity and quantum mechanics, tests of the weak equivalence principle (WEP) using antimatter are a further topic of interest. The WEP demands that the inertial and gravitational mass of a particle are equal. This can be tested by a direct gravity measurement of antimatter

particles in the gravitational field of earth, which is currently being pursued with a focus on antihydrogen by the AE$\bar{g}$IS (Doser et al., 2018; Kellerbauer et al., 2016; Kellerbauer et al., 2008), GBAR (Debu, 2012; Perez and Sacquin, 2012) and ALPHA collaborations (Bertsche, 2018). The research at CERN's antimatter factory will experience a boost in the coming years, due to the full commissioning of the ELENA ring. This is an additional small synchrotron, which is used as a second step after the AD, and allows to reduce the antiproton kinetic energy further from 5.3 MeV to 100 keV (Bartmann et al., 2018). For a comprehensive review of the research at the AD see (Bertsche et al., 2014; Hori and Walz, 2013; Madsen, 2018).

An important parameter for experiments on antihydrogen is the temperature at which it can be produced. This determines not only the fraction which can be trapped in shallow magnetic traps, but also the precision that can be achieved in e.g. spectroscopy and gravity measurements. The most successful scheme for antihydrogen production up to now is via three–body recombination (TBR), also called mixing. Here, antiprotons and positrons are brought in close proximity to each other by creating a nested trap. Antihydrogen is then mainly formed in three–body collisions:

$$\bar{\mathrm{p}} + \mathrm{e}^+ + \mathrm{e}^+ \rightarrow \bar{\mathrm{H}} + \mathrm{e}^+, \tag{1.2}$$

where the excess energy of the bound state is removed by the additional positron. TBR was used for the first successful production of low energy antihydrogen (Amoretti et al., 2002). Another important method is based on resonant charge exchange (RCE). Here, a cloud of antiprotons is irradiated with Rydberg positronium and antihydrogen created by the reaction:

$$\bar{\mathrm{p}} + \mathrm{Ps}^* \rightarrow \bar{\mathrm{H}}^* + \mathrm{e}^-. \tag{1.3}$$

This was demonstrated by (Storry et al., 2004) and is planned to be used for the gravity measurements of AE$\bar{g}$IS and GBAR. In comparison with TBR, this scheme has the advantage that no additional manipulations of oppositely charged plasmas in the trap are needed. Due to the large mass difference of its constituents, the temperature of the produced antihydrogen is dominated by the temperature of the antiprotons. Therefore, RCE can in principle reach much lower antihydrogen temperatures, since the antiprotons can be prepared at cryogenic temperatures before overlapping them with positronium.

The cooling of antiprotons as preparation for RCE is the main motivation for the topic of this thesis. The currently routinely used method at the AD is based on mixing the antiprotons with electrons inside a cryogenic Penning trap. Since electrons couple strongly to thermal radiation when placed in a magnetic field, they thereby thermalise the entire mixed plasma from the initial trapping energies in the kV regime, down to $\sim 100\,\mathrm{K}$ in around 60 s. A number of further cooling techniques can be employed, including adiabatic, resistive and evaporative cooling (see (Rolston and Gabrielse, 1989) for a theoretical overview and discussion), with the lowest reported value reached experimentally being 10 K (Andresen et al., 2010). Nevertheless, the precision gravity measurements planned by AE$\bar{g}$IS and GBAR require much lower temperatures. While GBAR plans to achieve this via the intermediate step of $\bar{\mathrm{H}}^+$ formation, which might be sympathetically coolable by laser cooled Beryllium ions, AE$\bar{g}$IS aims at initialising

antiprotons below 100 mK for RCE (Doser et al., 2012). For this, there are currently two methods under investigation: Using a dilution refrigerator in combination with electron cooling and active laser cooling of an anionic particle species, which in turn can sympathetically cool the antiprotons (Kellerbauer and Walz, 2006). This thesis concentrates on the second approach.

Since their first experimental realisation, laser cooling techniques for ions (Neuhauser et al., 1978; Wineland et al., 1978) and neutral atoms (Andreev et al., 1981; Ertmer et al., 1985) have been developed to a state, where they are now considered standard experimental tools (Phillips, 1998). The advent of this technology has led to new achievements in a number of areas in physics, including atomic clocks and Bose–Einstein condensation. Applying laser cooling to molecular species turned out to be much harder than for atoms. This is largely due to their intricate level structure, which makes repumping for a closed cooling cycle challenging. It was only in 2010 that the first direct laser cooling of the molecular species SrF was reported (Shuman et al., 2010), which up to this day has been extended to the two other diatomic molecules YO and CaF (Hummon et al., 2013; Zhelyazkova et al., 2014). Despite the overall success of laser cooling it has so far never been achieved for atomic or molecular anions. Given the slow progress in neutrals this is not surprising for the molecular case. For atomic anions on the other hand, the main hurdle is a lack of suitable candidates. Unlike in the case of molecular anions, where dipole moments can create strong bonds, the electrons in atomic anions are held by a mixture of induced dipole moments and correlation effects between the electron and the atom hull (Pegg, 2004). These only lead to shallow and short–range trapping potentials and typically only to a single bound state. Even though cases with excited bound states can be found, these are usually dipole forbidden and therefore of small interest for laser cooling.

Currently, only three anion species are under closer investigation in this regard: Os^-, Ce^- and La^-. Os^- was the first species in which a bound–bound dipole transition was found experimentally (Bilodeau and Haugen, 2000). A later refined investigation showed that this transition is spin–forbidden and therefore on the weaker end of dipole transitions. Doppler cooling for 4 K pre–cooled Os^- down to the Doppler limit was estimated to be possible within 300 s (Warring et al., 2009). Ce^- was the second species for which bound–bound dipole transitions were confirmed to exist (Walter et al., 2011). Even though there are no estimates on the prospects of laser cooling itself, the spin–forbidden nature of the transitions should make this challenging. The remaining species La^- is still under investigation. It seems to be a promising candidate for laser cooling and the transition strengths have recently been confirmed to be as high as theoretically predicted (Cerchiari et al., 2018; E. Jordan et al., 2015; O'Malley and Beck, 2010; Walter et al., 2014). See (Cerchiari, 2018; J. E. Jordan, 2015) for a detailed discussion of La^- and an overview of laser cooling with atomic anions.

Given the importance that cold anions have for antimatter research, the difficult nature of laser cooling atomic anions has led to an investigation into molecular anions. A detailed study by members of the AEgIS collaboration has singled out $C_2{}^-$ as a promising candidate (Yzombard et al., 2015), with the result that there is now a subgroup of AEgIS attempting to laser cool $C_2{}^-$. This group is called the BOREALIS project and is the

environment in which the work for this thesis was done. The initial tasks were to analyse the performance and the requirements of the cooling, as well to construct a source for C_2^-, which can provide a sufficiently large number of the anions in their ground state. These topics are also the content of this thesis and the results can therefore be divided into a theoretical and an experimental part. In the beginning of chapter 2, the internal dynamics and properties of diatomic molecules are discussed, and the molecule C_2^- with its level structure and transitions is introduced. The rest of the chapter is devoted to theoretical simulations on different laser cooling schemes and a discussion of their respective merits and complications. Chapter 3 then covers the experimental work and describes a C_2^- source that was built and the results which were acquired from it. In chapter 4 a conclusion on the presented work is drawn and an outlook given on the next steps that are necessary for successful laser cooling of molecular anions.

2. Theoretical discussion of possible cooling schemes

2.1. The internal dynamics of diatomic molecules

The intention of this section is to give an overview of the most important dynamics of diatomic molecules, with a special focus on the relations needed for the upcoming sections. Given the complexity of the matter, even for the restricted case of a diatomic molecule, the main goal is to motivate and summarise practically important formulas. Lengthy derivations have been omitted and the reader is instead referred to the literature. An introduction to the topic can be found in (Demtröder, 2016), while (Haken and Wolf, 2006; Lefebvre-Brion and Field, 2004) provide a more detailed discussion. The notation follows largely the convention in the literature (see A.1 for a summary).

2.1.1. The level structure of diatomic molecules

With the exception of the H_2^+ ion, where electron–electron interaction does not occur, analytic solutions for the molecular orbitals of diatomic molecules can not be found. An established method is to numerically approximate the molecular orbitals as a linear combination of atomic orbitals $\psi_n = \sum_i c_i \phi_i$. Treating the atom cores as fixed and their distance R from each other as an adjustable parameter, the coefficients can be optimised to minimise the energy of the state. This is referred to as the *Born–Oppenheimer approximation* and justified by the observation, that the dynamics of the cores happen on a timescale which is orders of magnitude larger than the dynamics of the electrons. This procedure leads to potential curves $E_n(R)$ of the different energy levels, which are very useful for the description of the dynamics in diatomic species. Bound states are characterised by a distinctive minimum denoted as R_e. The electronic states found in this way are usually classified according to the following features:

- The "energy" $T_\mathrm{e}(n) = \frac{E_n(R_\mathrm{e})}{hc}$ of the electronic state in cm^{-1}.
- The total electronic orbital angular momentum of the state $\mathbf{L} = \sum_i \mathbf{l}_i$ and its projection on the molecular axis $|L_z| = \hbar\Lambda$.
- The total electron spin of the state $\mathbf{S} = \sum_i \mathbf{s}_i$ and its projection on the molecular axis $S_z = \hbar M_S$.
- The symmetry of the wave function with respect to inversion at the origin:[1]

$$\psi_\mathrm{g}(-\mathbf{r}) = \psi_\mathrm{g}(\mathbf{r}) \qquad \psi_\mathrm{u}(-\mathbf{r}) = -\psi_\mathrm{u}(\mathbf{r}).$$

[1] The subscripts stem from the german *gerade* (even) and *ungerade* (uneven).

- The symmetry of the wave function with respect to reflection orthogonal to the molecular axis:

$$\psi^+(-x,y,z) = \psi^+(x,y,z) \qquad \psi^-(-x,y,z) = -\psi^-(x,y,z).$$

In the literature the electronic states are usually referenced in the form $N\,{}^{2S+1}\mathrm{L}^{+/-}_{\mathrm{g/u}}$. Here, N takes on letters, with a conventional X for the ground and a subsequent alphabetical ordering A, B, $C\ldots$ for the excited states. S denotes the total spin angular momentum and L the orbital angular momentum, which is represented by the symbols for the electronic states Σ, Π, Δ, ... See figure 2.1 for an example.

The energy shifts due to the dynamics of the atom cores, which lead to vibration and rotation of the molecule, can be deduced from the potential curves $E_n(R)$. In practice these curves are either calculated numerically or approximated by empirically deduced functions, which can be defined by spectroscopic constants (Jenč, 1996; Vanderslice et al., 1959). There are several different functions in use (Steele et al., 1962; Varshni, 1957; Zavitsas, 1991). A simple and instructive empirical approximation for the $E_n(R)$ curves is the *Morse* potential:

$$E_{\mathrm{M}}(R) = E_{\mathrm{D}}\left(1 - e^{-a(R-R_{\mathrm{e}})}\right)^2, \tag{2.1}$$

where E_{D} is the dissociation energy of the molecule. For this special choice of potential, the Schrödinger equation for the vibration of a diatomic molecule can be solved analytically. By introducing the reduced mass $\mu = M_{\mathrm{A}} \times M_{\mathrm{B}}/(M_{\mathrm{A}} + M_{\mathrm{B}})$ of the two atom cores A and B, the following expression for the vibrational energy levels can be found:

$$E_{\mathrm{vib}}(\nu) = \hbar\omega\left(\nu + \frac{1}{2}\right) - \frac{\hbar^2\omega}{4E_{\mathrm{D}}}\left(\nu + \frac{1}{2}\right)^2 \qquad \omega = a\sqrt{\frac{2E_{\mathrm{D}}}{\mu}}, \tag{2.2}$$

with ν being the vibrational quantum number. In the literature this relation is usually given in cm^{-1} as:

$$G(\nu) = \frac{E_{\mathrm{vib}}(\nu)}{hc} = \omega_{\mathrm{e}}\left(\nu + \frac{1}{2}\right) - \omega_{\mathrm{e}}x_{\mathrm{e}}\left(\nu + \frac{1}{2}\right)^2, \tag{2.3}$$

with experimentally determined values for ω_e and x_e. The energy contribution due to a rotation of the cores can be written as:

$$F(J_{\mathrm{rot}}) = \frac{E_{\mathrm{rot}}(J_{\mathrm{rot}})}{hc} = B_\nu J_{\mathrm{rot}}(J_{\mathrm{rot}}+1) - D_\nu\left[J_{\mathrm{rot}}(J_{\mathrm{rot}}+1)\right]^2 \tag{2.4}$$

$$B_\nu = B_{\mathrm{e}} - \alpha_{\mathrm{e}}\left(\nu + \frac{1}{2}\right) \qquad B_{\mathrm{e}} = \left(\frac{\hbar^2}{2}\right)\left(\frac{1}{hc}\right)\left(\frac{1}{\mu R_{\mathrm{e}}^2}\right). \tag{2.5}$$

Against conventional notation, J_{rot} is used here to indicate the quantum number of the rotational angular momentum. The constants B_{e}, α_{e} and D_ν are usually determined experimentally. The first term in (2.4) can be deduced by treating the two cores as a rigid rotator with the inertial moment $I = \mu R_{\mathrm{e}}^2$. The second term reflects a correction

which arises since the centrifugal force of the rotation increases the distance R_e of the cores and thereby the potential energy. As indicated by the subscript, B_ν and D_ν depend on the vibrational excitation of the molecule. This coupling is a result of the vibration's influence on the inertial moment, which results in a change of the rotational energy. Since the dynamics of the vibration are two orders of magnitude faster than the rotation, equation (2.4) incorporates the average of this effect.

In summary, the energy levels of a diatomic molecule are given by the equation:

$$T(n, \nu, J_\mathrm{rot}) = T_\mathrm{e}(n) + G(\nu) + F(J_\mathrm{rot}) \tag{2.6}$$

and are defined by the five constants ω_e, x_e, B_e, α_e and D_ν.

2.1.2. Selection rules and transition strengths of diatomic molecules

The strength of the radiative transition between two states i and j of a diatomic molecule is in first order described by the transition dipole moment:

$$\mathbf{M}_{ij} = \int \Psi_i^* \mathbf{p} \Psi_j d\mathbf{r}_\mathrm{e} d\mathbf{R}_\mathrm{N}, \tag{2.7}$$

where $\mathbf{r}_\mathrm{e}$ and $\mathbf{R}_\mathrm{N}$ are the coordinates of the electrons and the atom cores, and $\mathbf{p} = -\sum_i e\mathbf{r}_{\mathrm{e},i} + e\left(Z_\mathrm{A}\mathbf{R}_{\mathrm{N,A}} + Z_\mathrm{B}\mathbf{R}_{\mathrm{N,B}}\right) = \mathbf{p}_\mathrm{e} + \mathbf{p}_\mathrm{N}$ the dipole moment operator. By looking at the structure of (2.7), a first important selection rule can be deduced. Since the integral of an antisymmetric function is zero, and the dipole operator $\mathbf{p}$ is antisymmetric, it follows that the product of the wave functions $\Psi_i^*\Psi_j$ must be antisymmetric as well. Put in another form, this means that *the transition must be between two states of unlike parity.*

The wave function can be separated into a contribution of the electrons $\psi_i(\mathbf{r}_\mathrm{e})$ and the cores $\phi_i(\mathbf{R}_\mathrm{N})$, resulting in: $\Psi_i = \psi_i(\mathbf{r}_\mathrm{e})\phi_i(\mathbf{R}_\mathrm{N})$. Using this, the expression for the transition dipole moment can be rewritten:

$$\mathbf{M}_{ij} = \int \phi_i^* \left(\int \psi_i^* \mathbf{p}_\mathrm{e} \psi_j d\mathbf{r}_\mathrm{e} \right) \phi_j d\mathbf{R}_\mathrm{N} + \int \phi_i^* \mathbf{p}_\mathrm{N} \left(\int \psi_i^* \psi_j d\mathbf{r}_\mathrm{e} \right) \phi_j d\mathbf{R}_\mathrm{N}. \tag{2.8}$$

At this point it is useful to differentiate between two cases: rotation–vibration (ro–vib) transitions within the same electronic state and transitions between two different electronic states.

In the **first case**, the integral of $\psi_i^* \mathbf{p}_\mathrm{e} \psi_j \propto \mathbf{r}\left|\psi_i\right|^2$ vanishes due to symmetry. Given the normalisation of the wave function, the expression for the transition dipole moment becomes:

$$\mathbf{M}_{ij} = \int \phi_i^* \mathbf{p}_\mathrm{N} \phi_j d\mathbf{R}_\mathrm{N}. \tag{2.9}$$

The wave function describing the cores can be written as the product $\phi_i(R, \theta, \phi) = S_\nu(R) Y^M_{J_\mathrm{rot}}(\theta, \phi)$, where $S_\nu(R)$ are the solutions to the Schrödinger equation describing the vibration and $Y^M_{J_\mathrm{rot}}$ the spherical harmonics describing the rotation. Using their

known properties one can deduce the following selection rules for non–vanishing transition dipole moments:

$$\Delta\nu = 0,\ \pm 1 \qquad\qquad \Delta J_{\mathrm{rot}} = \pm 1. \tag{2.10}$$

The left term is valid for a harmonic potential, while for anharmonic potentials transitions with $\Delta\nu = 2, 3, 4\ldots$ are allowed as well, albeit much weaker. A special case arises for homonuclear diatomic molecules. Here, the dipole moment $\mathbf{p}_{\mathrm{N}}$ vanishes and therefore suppresses pure ro–vib transitions completely.

In the **second case** of $i \neq j$, the term $\int \psi_i^* \psi_j d\mathbf{r}_{\mathrm{e}}$ vanishes due to the orthogonality of the electronic wave functions. The transition dipole moment therefore becomes:

$$\mathbf{M}_{ij} = \int \phi_i^* \mathbf{M}_{ij}^{\mathrm{e}}(R) \phi_j d\mathbf{R}_{\mathrm{N}} \qquad \text{with} \qquad \mathbf{M}_{ij}^{\mathrm{e}} = \int \psi_i^* \mathbf{p}_{\mathrm{e}} \psi_j d\mathbf{r}_{\mathrm{e}}. \tag{2.11}$$

The electronic transition dipole moment $\mathbf{M}_{ij}^{\mathrm{e}}(R)$ still depends on R, the distance between the atom cores. In a first approximation the term can be evaluated at R_{e} (see subsection 2.1.1) and treated as constant. Substituting the vibrational and rotational eigenfunctions for ϕ therefore allows to write:

$$\mathbf{M}_{ij} = M_{ij}^{\mathrm{e}}(R_{\mathrm{e}}) \int S_{\nu_i} S_{\nu_j} R^2 dR \int Y_{J_{\mathrm{rot},i}}^{M_i} Y_{J_{\mathrm{rot},j}}^{M_j} \hat{\mathbf{p}} \sin\theta \, d\theta \, d\phi. \tag{2.12}$$

The probability for spontaneous transitions is proportional to the absolute square of the transition dipole moment, leading to the following definitions which are often used in the literature:

The Franck–Condon factor:

$$FC(\nu_i, \nu_j) = \left| \int S_{\nu_i} S_{\nu_j} R^2 dR \right|^2 \tag{2.13}$$

The Hönl–London factor:

$$HL(J_i, J_j) = \left| \int Y_{J_{\mathrm{rot},i}}^{M_i} Y_{J_{\mathrm{rot},j}}^{M_j} \hat{\mathbf{p}} \sin\theta \, d\theta \, d\phi \right|^2 . \tag{2.14}$$

Even though the transition strength varies, the Franck–Condon factor does not impose any general selection rule for the case of electronic transitions. From the Hönl–London factor the following two cases can be derived for allowed transitions:

$$\begin{gathered} \Delta J_{\mathrm{rot}} = \pm 1 \\ \Delta J_{\mathrm{rot}} = 0 \qquad \text{if} \qquad \Delta\Lambda = \pm 1. \end{gathered} \tag{2.15}$$

In the case that the core distance R_{e} does not differ significantly for two electronic states, transitions with $\Delta J = \pm 2$ are possible, albeit much weaker. Given the complexity of the level structure and transitions of molecules, it is common practice to use specialised software for their analysis (see section 2.3).

2.2. Semiclassical treatment of the interaction of molecules with light

The aim of this section is to state the relations for the interaction of (laser–)light with molecules, that are necessary to understand the calculations done in this thesis. Since these calculations are to a large part based on rate equations, an important part of this section is to give a summary of the simplifications leading to these equations and a justification for their use. In a first step, the optical Bloch equations will be derived for the simple case of a two–level atom. For a specific range of parameters, these can then be simplified to form rate equations, which can then be generalised for the description of multi–level species like molecules. Given its importance for one of the cooling schemes discussed in this thesis, the last part of this section is devoted to the AC Stark effect. The treatment of these topics follows closely the one given in (Foot, 2005; Höppner et al., 2012; Loudon, 2000).

2.2.1. Optical Bloch equations

The time evolution of a two–level atom in an electric field is in first order described by the Schrödinger equation:

$$i\hbar\frac{\partial}{\partial t}\Psi_{\mathrm{A}}(\mathbf{r},t) = \left(\hat{H}_{\mathrm{A}} + \hat{H}_{\mathrm{I}}(t)\right)\Psi_{\mathrm{A}}(\mathbf{r},t), \tag{2.16}$$

with $\hat{H}_{\mathrm{A}}$ being the Hamilton operator of the atom and $\hat{H}_{\mathrm{I}}$ the operator describing the light interaction, given by:

$$\hat{H}_{\mathrm{I}}(t) = e\mathbf{r}\cdot\mathbf{E}_0(t)\cos(\omega_{\mathrm{L}}t). \tag{2.17}$$

The general solution of (2.16) can be stated using the Dirac notation for the Eigenstates $|i\rangle$ of $\hat{H}_{\mathrm{A}}$:

$$|\Psi(\mathbf{r},t)\rangle = c_1(t)\,|1\rangle\,e^{-iE_1t/\hbar} + c_2(t)\,|2\rangle\,e^{-iE_2t/\hbar}, \tag{2.18}$$

with $\hat{H}_{\mathrm{A}}\,|i\rangle = E_i\,|i\rangle$ and unknown coefficients $c_i(t)$. Substituting (2.18) into (2.16) and multiplying from the left with $|1\rangle$ and $|2\rangle$ gives:

$$\begin{aligned} i\dot{c}_1 &= \Omega\cos(\omega_{\mathrm{L}}t)e^{-i\omega_0t}c_2 \\ i\dot{c}_2 &= \Omega^*\cos(\omega_{\mathrm{L}}t)e^{i\omega_0t}c_1, \end{aligned} \tag{2.19}$$

where $\omega_0 = (E_2 - E_1)/\hbar$ and the so–called *Rabi–frequency* Ω was introduced. This frequency is defined as:

$$\Omega = \frac{\langle 1|\, e\mathbf{r}\cdot\mathbf{E}_0\,|2\rangle}{\hbar} \overset{\mathrm{I}}{\simeq} \frac{e\,|\mathbf{E}_0|\,\langle 1|\,\mathbf{r}\cdot\mathbf{e}_{\mathrm{pol}}\,|2\rangle}{\hbar}, \tag{2.20}$$

where step I assumes that the electric field is homogeneous at the position of the atom and $\mathbf{e}_{\mathrm{pol}}$ is the unit vector giving the polarisation of the field. As will become evident in the next section for the case of rate equations, the squared Rabi–frequency, averaged

over different spatial orientations of the atom, is of special interest. Using (2.20) this quantity can be calculated to be:

$$\begin{aligned}\langle|\Omega|^2\rangle_{\mathrm{pol}} &= \frac{e^2\,|\mathbf{E}_0|^2}{\hbar^2}\frac{1}{4\pi}\int_0^{2\pi}\int_0^{\pi}|\langle 1|\,\mathbf{r}\cdot\mathbf{e}_{\mathrm{pol}}(\phi,\theta)\,|2\rangle|^2\sin(\theta)d\theta d\phi \\ &= \frac{e^2\,|\mathbf{E}_0|^2}{\hbar^2}\frac{|\langle 1|\,\mathbf{r}\,|2\rangle|^2}{3} \equiv \frac{|\mathbf{E}_0|^2}{\hbar^2}\frac{|M_{12}|^2}{3},\end{aligned} \tag{2.21}$$

where the absolute square of the transition dipole moment was defined as $|M_{12}|^2 = |\langle 1|\,e\mathbf{r}\,|2\rangle|^2$.

Equations (2.19) can further be translated into the density matrix formalism for the two–level system. Using the definition $\rho_{ij} = c_i c_j^*$ and $\frac{d}{dt}\rho_{ij} = \left(\frac{dc_i}{dt}\right)c_j^* + c_i\left(\frac{dc_j^*}{dt}\right)$ leads to:

$$\dot{\rho}_{22} = -\dot{\rho}_{11} = -i\cos(\omega_{\mathrm{L}}t)\left(e^{i\omega_0 t}\Omega^*\rho_{12} + e^{-i\omega_0 t}\Omega\rho_{21}\right) \tag{2.22}$$

$$\dot{\rho}_{12} = \dot{\rho}_{21}^* = i\Omega\cos(\omega_{\mathrm{L}}t)e^{-i\omega_0 t}\left(\rho_{11}-\rho_{22}\right). \tag{2.23}$$

These equations can be further simplified by substituting $\cos(\omega_{\mathrm{L}}t) = \frac{1}{2}\left(e^{i\omega_{\mathrm{L}}t} + e^{-i\omega_{\mathrm{L}}t}\right)$. This leads to terms oscillating with $\omega_0 + \omega_{\mathrm{L}}$ and $\omega_0 - \omega_{\mathrm{L}}$. Usually one is interested in the effects of light near the resonance frequency ω_0 of the transition, meaning that $\omega_0 + \omega_{\mathrm{L}} \gg \omega_0 - \omega_{\mathrm{L}}$. For this case, by expanding the ρ_{ij} in a Taylor series and integrating over time, it can be shown that the fast oscillating terms have a much smaller contribution and can be neglected. This is usually called the *rotating wave approximation* and leads to:

$$\dot{\rho}_{22} = -\dot{\rho}_{11} = -i\frac{1}{2}\left(e^{i(\omega_0-\omega_{\mathrm{L}})t}\Omega^*\rho_{12} - e^{-i(\omega_0-\omega_{\mathrm{L}})t}\Omega\rho_{21}\right) \tag{2.24}$$

$$\dot{\rho}_{12} = \dot{\rho}_{21}^* = i\frac{1}{2}\Omega e^{-i(\omega_0-\omega_{\mathrm{L}})t}\left(\rho_{11}-\rho_{22}\right). \tag{2.25}$$

In addition, it is convenient to express the equations using the new definitions: $\delta = \omega_0 - \omega_{\mathrm{L}}$, $\sigma = e^{i\delta t}\rho_{12}$ and $n = \rho_{22} - \rho_{11}$:

$$\dot{n} = -i\left(\Omega^*\sigma - \Omega\sigma^*\right) \tag{2.26}$$

$$\dot{\sigma} = -i\frac{1}{2}\Omega n + i\delta\sigma. \tag{2.27}$$

So far not included in the formalism is the spontaneous emission of radiation. This effect can not be derived from a semiclassical treatment of the light interaction and requires to quantise the light field itself. In a semiclassical treatment the effect is included via an additional damping term A_{21}, that is usually motivated with the classical analogue of a damped harmonic oscillator. Since this is out of the scope of this thesis, the end result, referred to as *optical Bloch equations*, is simply stated here:

$$\dot{n} = -A_{21}(n+1) - i\left(\Omega^*\sigma - \Omega\sigma^*\right) \tag{2.28}$$

$$\dot{\sigma} = -i\frac{1}{2}\Omega n - \underbrace{\left(\frac{A_{21}}{2} - i\delta\right)}_{=:\gamma}\sigma. \tag{2.29}$$

2.2.2. Rate equations

While (2.28) and (2.29) can now be used to calculate the wave function of a single two–level atom, often one is only interested in the average populations $\bar{\rho}_{ii}$ of an ensemble of atoms and the rate at which they change. In this case, for specific types of radiation and transitions, the optical Bloch equations can be further simplified to so–called rate equations. A detailed discussion on this topic can be found in (Höppner et al., 2012), while here the focus is on the most essential parts.

In a first step, (2.29) can be formally integrated to:

$$\sigma(t) = \underbrace{\sigma(0)e^{-\gamma t}}_{\text{transient}} - \frac{i}{2}\int_0^t \Omega(t')n(t')e^{-\gamma(t-t')}dt', \tag{2.30}$$

where the first transient term vanishes quickly and can be dropped. Substituting into (2.28) then gives:

$$\frac{dn}{dt} = -A_{21}(n+1) - \mathrm{Re}\left[\int_0^t \Omega(t)\Omega^*(t')n(t')e^{-\gamma(t-t')}dt'\right]. \tag{2.31}$$

So far this equation still describes the dynamics of a single atom. Taking the arithmetic mean $\bar{n} \equiv \langle n \rangle$ over many atoms produces:

$$\frac{d\bar{n}}{dt} = -A_{21}(\bar{n}+1) - \frac{|M_{12}|^2}{3\hbar^2}\mathrm{Re}\left[\int_0^t K(t,t')e^{-\gamma(t-t')}dt'\right], \tag{2.32}$$

where (2.21) and the new definition $K(t,t') = \langle E_0(t)E_0(t')n(t')\rangle$ was used. For commonly used light sources, the remaining time dependence of $E_0(t)$ is due to random fluctuations. It is therefore reasonable to assume that $E_0(t)$ and $n(t)$ are decorrelated, which motivates the approximation $K(t,t') \approx \langle E_0(t)E_0(t')\rangle\,\bar{n}(t')$. This relation is connected to the spectral energy density $W(\omega)$ in $\mathrm{J}\times\mathrm{s}\times\mathrm{m}^{-3}$ via the *Wiener–Khintchine theorem* $\langle E_0(t)E_0(t')\rangle = \frac{2}{\varepsilon_0}\int_{\mathbb{R}} W(\omega)e^{-i\omega(t-t')}d\omega$. Together with the definition of γ this produces:

$$\frac{d\bar{n}}{dt} = -A_{21}(\bar{n}+1) - \frac{2\,|M_{12}|^2}{3\hbar^2\varepsilon_0}\mathrm{Re}\left[\int_0^t\int_{\mathbb{R}} \bar{n}(t')W(\omega)e^{-i(\omega-\delta)(t-t')}e^{-A_{21}/2(t-t')}d\omega dt'\right], \tag{2.33}$$

where γ was replaced by the original term from (2.29). In order to further simplify this equation, it is desirable to remove $\bar{n}(t')$ from the integral. This can be done by noting that either $\int_{\mathbb{R}} W(\omega)e^{-i\omega(t-t')}d\omega$ or $e^{-A_{21}/2(t-t')}$ will be sharply centred around t, if the energy spectrum is very broad or A_{21} is very large. These assumptions allow to replace $\bar{n}(t') \to \bar{n}(t)$, which is called the *Markov approximation*. Physically this means, that $\bar{n}$

has no memory of previous times. Solving the integral, which again involves dropping a transient term, then leads to:

$$\frac{d\bar{n}}{dt} = -A_{21}(\bar{n}+1) - 2W_{21}\underbrace{\frac{\pi\left|M_{12}\right|^2}{3\hbar^2\varepsilon_0}}_{=:B_{21}}\underbrace{\left(\frac{1}{\pi W_{21}}\int\limits_{\mathbb{R}} W(\omega-\omega_\mathrm{L})\frac{A_{21}/2}{(A_{21}/2)^2+(\omega-\omega_0)^2)}d\omega\right)}_{=:\zeta_{21}}\bar{n}, \tag{2.34}$$

where $W_{21} = \int_{\mathbb{R}} W(\omega)d\omega$. B_{21} is the *Einstein coefficient* of stimulated emission which, while not done here, can be shown to be connected to the Einstein coefficient of spontaneous emission A_{21}:

$$A_{21} = \frac{1}{\tau} = \frac{\hbar\omega_0^3}{\pi^2c^3}B_{21}, \tag{2.35}$$

where τ is the natural lifetime of the excited state. The factor ζ_{21} is an overlap integral of the normalised energy spectrum of the light centred around ω_L, and a Lorentz distribution centred around ω_0, describing the light spontaneously emitted by the atom. Using the relations $\bar{n} = \bar{\rho}_{22} - \bar{\rho}_{11}$ and $\bar{\rho}_{11} + \bar{\rho}_{22} = 1$, (2.34) can be cast into two coupled equations for the populations:

$$\begin{aligned}\frac{d\bar{\rho}_{11}}{dt} &= A_{21}\bar{\rho}_{22} + W_{21}B_{21}\zeta_{21}(\bar{\rho}_{22}-\bar{\rho}_{11})\\ \frac{d\bar{\rho}_{22}}{dt} &= -A_{21}\bar{\rho}_{22} - W_{21}B_{21}\zeta_{21}(\bar{\rho}_{22}-\bar{\rho}_{11}).\end{aligned} \tag{2.36}$$

These are the general *rate equations*. While these equations are much easier to handle than the optical Bloch equations, it is important to respect the simplifying assumptions that were made in deriving them. Given a light field with Lorentzian shape and a full width half maximum (FWHM) of Δ, two necessary conditions can be derived for (2.36) to be justified:

$$A_{21} \ll \frac{A_{21}+\Delta}{2} \qquad B_{21}W_{21} \ll \frac{A_{21}+\Delta}{4\zeta_{21}}. \tag{2.37}$$

Given that these are fulfilled for each transition, (2.36) can be easily generalised to the case of a multi–level atom. Using a new notation for the populations $\Pi_i = \bar{\rho}_{ii}$ and excluding the treatment of degenerate levels, the equations become:

$$\dot{\Pi}_i = \Sigma_j\left[A_{ji}\Pi_j - A_{ij}\Pi_i + W_{ji}B_{ji}\zeta_{ji}(\Pi_j-\Pi_i)\right]. \tag{2.38}$$

2.2.3. The AC Stark effect

Using equation (2.18) one can see, that the oscillating electric field induces a dipole moment in the atom:

$$\langle\Psi(\mathbf{r},t)|\, e\hat{\mathbf{r}}\,|\Psi(\mathbf{r},t)\rangle = M_{12}\sigma^* e^{i\omega_\mathrm{L}t} + \text{c.c.} \tag{2.39}$$

This leads to an interaction energy of the dipole with the field:

$$E_\mathrm{Dip} = \frac{1}{2}e\mathbf{d}\times\mathbf{E}(\mathrm{r}) \propto |\mathbf{E}|^2 \tag{2.40}$$

that is proportional to the intensity of the light field. While the derivation is lengthy and therefore omitted, it can be shown (Dalibard and Cohen–Tannoudji, 1985; Grimm et al., 2000) that this interaction leads to a gradient force on the atom and can be described by the effective potential:

$$U_{\mathrm{dip}}(\mathbf{r}) = -\frac{\hbar\delta}{2} \ln\left(1 + \frac{\Omega^2(\mathbf{r})}{2\delta^2 + A_{21}^2/2}\right). \tag{2.41}$$

2.3. The level structure and transitions of C_2^-

In the optimal case, a species considered for laser cooling would exhibit a strong transition, where the upper state can only decay to the lower state of the transition. In nature it is usually not possible to find such a candidate, and so finding a transition involves a trade–off between, among others, the strength of the transition and the number of levels one has to repump in order to close the cooling cycle. For anionic molecules such a survey was conducted in (Yzombard et al., 2015), where C_2^- was singled out as a suitable species. This anion exhibits three bound electronic states, with an electron affinity (EA) of the ground state of EA = 3.269 eV (M. K. Ervin and Lineberger, 1991). Concerning the implementation of a laser cooling cycle it has several favourable characteristics. The lack of a hyperfine structure results in a reduction of complexity, which is advantageous for the application in high magnetic fields as e.g. found in a Penning trap. Given that it is a homonuclear species, the possible transitions are greatly restricted by the selection rules presented in chapter 2.1.2. A practical advantage is also, that the spectrum is well known and was extensively studied (Bruna and Grein, 2000; M. K. Ervin and Lineberger, 1991; Jones et al., 1980; Mead et al., 1985; Rehfuss et al., 1988; Rosmus and Werner, 1984; Royen and Zackrisson, 1992; Šedivcová and Špirko, 2006; Shan-Shan et al., 2003). Part of the data presented in this section is based on the open software PGOPHER (Western, 2017) together with an input file that was kindly provided by Prof. Daniel Comparat and is based on spectroscopic constants from the literature given above.

An overview of the electronic and vibrational level structure of C_2^- can be seen in figure 2.1. The molecule exhibits two bound excited levels $A^2\Pi_u$ and $B^2\Sigma_u^+$. Due to parity and the homonuclear character of C_2^-, transitions between these two states and pure ro–vib transitions are prohibited, which only leaves two possible electronic transitions: $B^2\Sigma \leftrightarrow X^2\Sigma$ and $A^2\Pi \leftrightarrow X^2\Sigma$. In order to minimise the population of unwanted states and maximise the transition strength, it is reasonable to choose the lowest vibrational levels for laser cooling. This leaves the two transitions[2] $B^2\Sigma(v' = 0) \leftrightarrow X^2\Sigma(v'' = 0)$ at 541 nm and $A^2\Pi(v' = 0) \leftrightarrow X^2\Sigma(v'' = 0)$ at 2.54 µm. The $B^2\Sigma(v' = 0)$ state has a lifetime of $\tau = 75$ ns and a total of eleven lower vibrational states of the $X^2\Sigma$ electronic level. The first seven transitions $B^2\Sigma(v' = 0) \leftrightarrow X^2\Sigma(v'' = 0, \ldots 6)$ are in the optical and near infrared, with wavelengths at 541, 598, 667, 753, 863, 1007 and 1206 nm. The lifetime of the $B^2\Sigma(v' = 0)$ state corresponds to a decay rate of

[2]The convention in the literature is to denote upper level quantum numbers with $'$ and lower with $''$.

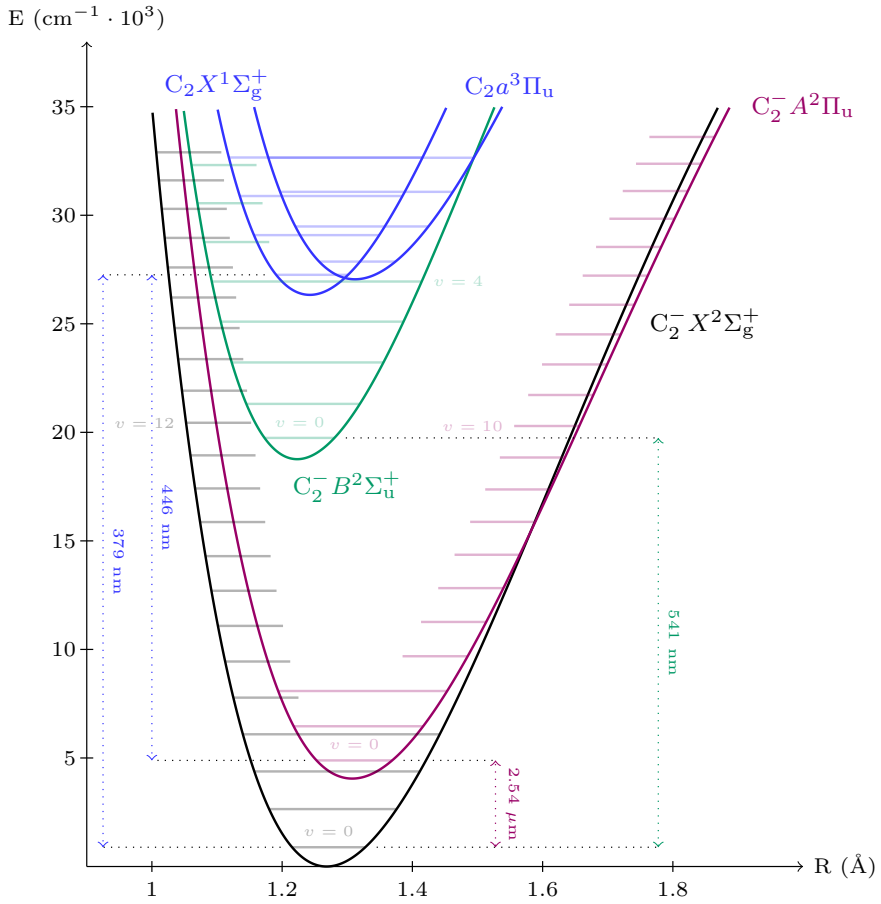

Figure 2.1.: Overview of the electronic and vibrational level structure of C_2^- and C_2. The potential curves of the molecule were calculated using the empirical function proposed in (Zavitsas, 1991), using spectroscopic parameters from (M. K. Ervin and Lineberger, 1991; Šedivcová and Špirko, 2006). For C_2 the curves where shifted by the electron affinity EA = 3.269 eV. The vibrational levels are based on equation (2.3) and constans from (M. K. Ervin and Lineberger, 1991).

$2\pi \times 2.1\,\mathrm{MHz}$, which branches to the lower states with fractions of 72, 23, 5, 0.8, 0.1, 2×10^{-4}, 3×10^{-5} and 4×10^{-6}. In comparison, the $A^2\Pi(v' = 0)$ state is much longer lived with $\tau = 51\,\mu\mathrm{s}$, corresponding to a decay rate of $2\pi \times 3.1\,\mathrm{kHz}$, and can decay to only three lower vibrational levels. The transitions $A^2\Pi(v' = 0) \leftrightarrow X^2\Sigma(v'' = 0, 1, 2)$ are at wavelengths 2.54, 4.57 and 22.1 µm and branch with the fractions 0.96, 0.04 and 3×10^{-4}.

Laser cooling on the $B^2\Sigma(v' = 0) \leftrightarrow X^2\Sigma(v'' = 0)$ transition was investigated in (Yzombard et al., 2015). In comparison to using $A^2\Pi(v' = 0)$ as excited state, the benefit is clearly the strength and the smaller wavelength of the transition, allowing for much faster cooling. On the downside there are significantly more lower vibrational levels that need to be repumped in order to close the cooling cycle. Especially given the rotational substructure of each vibrational level, this leads to a significant experimental complication. For this reason, this thesis focuses on possible laser cooling on the $A^2\Pi(v' = 0) \leftrightarrow X^2\Sigma(v'' = 0)$ transition in order to complement the work that was already done on the $B^2\Sigma(v' = 0) \leftrightarrow X^2\Sigma(v'' = 0)$ transition. The goal is to enable an informed decision, based on the merits and disadvantages of the two possibilities.

Figure 2.2 gives an overview of the $A^2\Pi(v' = 0, J' = 1/2) \leftrightarrow X^2\Sigma$ transitions and the rotational levels involved for molecules in a magnetic field of $50\,\mu\mathrm{T}$, which is the same order of magnitude as the earth magnetic field. With $\Gamma_{\mathrm{tot}} < 2\pi \times 10\,\mathrm{MHz}$ the $A^2\Pi(v' = 0, J' = 1/2) \leftrightarrow X^2\Sigma(v'' = 2)$ decay channel only becomes relevant for pumping durations of ~ 100 s and can therefore usually be neglected. For this reason its rotational substructure is omitted in the graphic, but is analogous to $v'' = 0, 1$. Given that one of the strong $A^2\Pi(v' = 0, J' = 1/2) \leftrightarrow X^2\Sigma(v'' = 0, J'' = 1/2)$ transitions is used for the cooling, this leaves eleven dark states that need to be repumped.

While the shown structure is relevant in the case of laser cooling in a Paul trap or for spectroscopy, the large magnetic fields in a Penning trap make a notable difference: figure 2.3 shows the transitions from only one of the upper levels $A^2\Pi(v' = 0, J' = 1/2, M' = +1/2) \leftrightarrow X^2\Sigma$ for a magnetic field of 1 and 5 T. The breakdown of the mixing of the angular contributions leads to additional transitions, which are forbidden in the low field case. However, the enlarged splitting of the $A^2\Pi(v' = 0, J' = 1/2, M' = \pm 1/2)$ levels allows to easily resolve them, thereby reducing the number of possible decay channels. Using $A^2\Pi(v' = 0, J' = 1/2, M' = 1/2) \leftrightarrow X^2\Sigma(v'' = 0, J'' = 1/2, M'' = 1/2)$ for cooling, then leaves a total of 15 levels that need to be repumped. The $A^2\Pi(v' = 0, J' = 1/2) \leftrightarrow X^2\Sigma(v'' = 2)$ decay channel was neglected for the same reasons as before.

2.4. Discussion of relevant dynamics in a Penning trap

This section discusses the physics of charged particles in a Penning trap, to the extent that is necessary for the understanding of the upcoming sections. Especially for the case of larger ion clouds, the dynamics become complex and the theoretical treatment cumbersome. For this reason a detailed description is out of the scope of this thesis and the reader is referred to (Dubin and O'Neil, 1999) for an overview of the topic, (Davidson, 2001) for a detailed treatment of nonneutral plasmas and (Knoop et al., 2014; Major

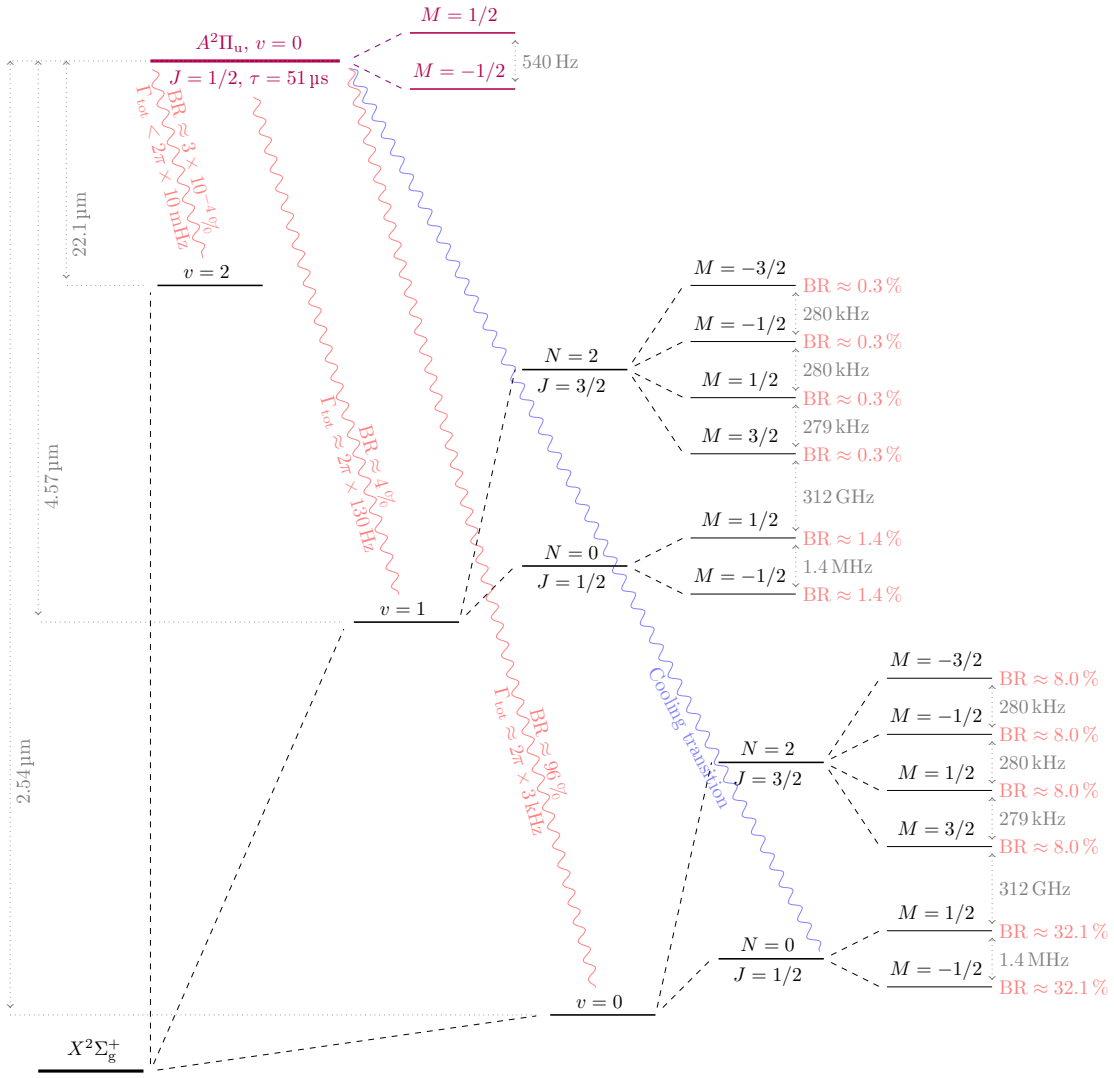

Figure 2.2.: Overview of the $A^2\Pi(v' = 0, N' = 1, J' = 1/2, M' = \pm 1/2) \leftrightarrow X^2\Sigma$ transitions in a magnetic field of 50 µT. Given the small overall branching fraction, the rotational structure of the $A^2\Pi(v' = 0, N' = 1, J' = 1/2, M' = \pm 1/2) \leftrightarrow X^2\Sigma(v'' = 2)$ transition is not shown. The two upper states are treated as degenerate due to their small splitting.

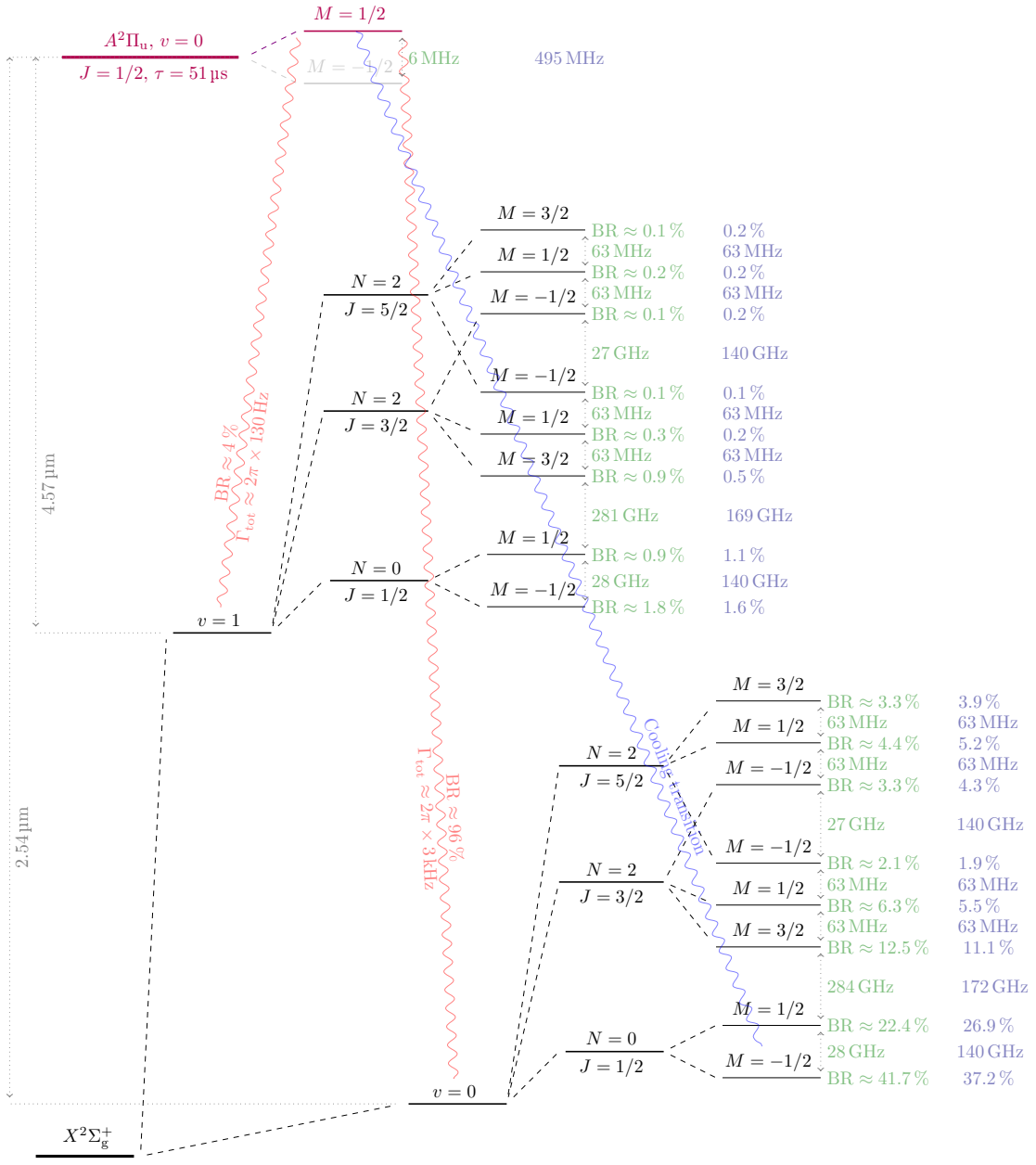

Figure 2.3.: Overview of the $A^2\Pi(v' = 0, N' = 1, J' = 1/2, M' = +1/2) \leftrightarrow X^2\Sigma(v'' = 0, 1)$ transitions for high magnetic fields. The splittings and branching ratios are given for a 1 T (green) and 5 T (blue) field. The $A^2\Pi(v' = 0, N' = 1, J' = 1/2, M' = +1/2) \leftrightarrow X^2\Sigma(v'' = 2)$ transitions are omitted due to the small branching fraction.

et al., 2005) for an introduction.

2.4.1. Confinement and conservation of angular momentum

Penning traps use the combination of an axial magnetic field for radial and an electric quadrupole field for axial confinement of charged particles. The dynamics of an ion cloud with N identical particles with charge q is described by the following Hamiltonian in cylindrical coordinates:

$$H = \sum_{j=1}^{N} \left(\frac{p_{r_j}^2}{2m} + \frac{\left[p_{\theta_j} - \frac{q}{2} B_z r_j^2 \right]^2}{2m r_j^2} + \frac{p_{z_j}^2}{2m} \right) + \sum_{j=1}^{N} q\phi_{\mathrm{T}}(r_j, z_j) + \frac{1}{2} \sum_{i \neq j} q^2 G(\mathbf{r}_i - \mathbf{r}_j). \tag{2.42}$$

Here, $\phi_{\mathrm{T}}(\mathbf{r}_j)$ is the electric quadrupole potential of the trap, $G(\mathbf{r}_i - \mathbf{r}_j)$ describes the inter–particle Coulomb interaction and the mirror charges induced in the trap electrodes and

$$p_{r_j} = m\dot{r}_j \qquad p_{\theta_j} = m r_j^2 \dot{\theta}_j + \frac{q}{2} B_z r_j^2 \qquad p_{z_j} = m\dot{z}_j \tag{2.43}$$

are the canonical momenta. Since (2.42) is time independent due to $\frac{\partial H}{\partial t} = 0$ and exhibits cylindrical symmetry, it follows that energy and the total canonical momentum are conserved:

$$H = E = \text{const} \qquad P_\theta = \sum_{j=1}^{N} p_{\theta_j} = L = \text{const}. \tag{2.44}$$

This already leads to a strong statement of particle confinement by writing:

$$L = \sum_{j=1}^{N} m r_j v_j + q A_\theta(r_j) r_j \simeq \frac{q B_z}{2} \sum_{j=1}^{N} r_j^2. \tag{2.45}$$

Here, $A_\theta(r_j) = \frac{B_z r_j}{2}$ was used. For the usual values of B_z in Penning traps, the last approximation is well justified. Conservation of angular momentum therefore acts as a statistical bound on the radial orbit that the particles can reach.

By examining the dynamics in a frame rotating at the frequency $-\omega$ around the magnetic field axis, further insights can be made. The Hamiltonian in the rotating system is simply given by $H_{\mathrm{R}} = H + \omega L$ and from now on capital letters will be used to denote the coordinates and velocities in the rotating frame. H_{R} can be expressed in velocity variables using $p_{\Theta_j} = m R_j^2 \dot{\Theta}_j + \frac{q}{2} B_z R_j^2 - \frac{m}{2} \omega R^2$. This results in (see A.2 for details):

$$H_{\mathrm{R}} = \sum_{j=1}^{N} \frac{m}{2} \mathbf{V}_j^2 + \sum_{j=1}^{N} \underbrace{q\phi_{\mathrm{T}}(R_j, Z_j) + \frac{1}{2} m\omega(\Omega_{\mathrm{c}} - \omega) R_j^2}_{=: q\phi_{\mathrm{R}}(R_j, Z_j)} + \frac{1}{2} \sum_{i \neq j} q^2 G(\mathbf{R}_i - \mathbf{R}_j). \tag{2.46}$$

Here, the *cyclotron frequency* $\Omega_\mathrm{c} = \frac{qB_z}{m}$ and the effective trap potential ϕ_R have been defined, as seen by the particle in the rotating frame. A closer inspection of ϕ_R shows, that it has three contributions: the electric trap potential ϕ_T, a centrifugal term $\propto -\omega^2 R_j^2$ and a term $\propto \Omega_\mathrm{c}\omega R_j^2$ coming from the rotation of the particles in the magnetic field. By choosing the right quadrupole potential ϕ_T and parameters in $\frac{1}{2}m\omega(\Omega_\mathrm{c}-\omega)R_j^2$, the quadratic dependence on R_j can therefore be used to create a radially confining potential.

2.4.2. Trap frequencies and dynamics

It is instructive to look at the dynamics of a single particle for the specific choice of a quadratic electric potential: $\phi_\mathrm{T}(R,Z) = \frac{m\Omega_\mathrm{z}^2}{2}(Z^2 - R^2/2)$. Here Ω_z is defined by the confinement voltage of the trap. Using this, the single particle Hamiltonian in the rotating frame becomes:

$$H_\mathrm{R} = \frac{m}{2}\left(\dot{R}^2 + R^2\dot{\Theta}^2 + \dot{Z}^2\right) + \frac{m}{2}Z^2\Omega_\mathrm{z}^2 + \frac{m}{2}R^2\left(\omega(\Omega_\mathrm{c}-\omega) - \Omega_\mathrm{z}^2/2\right). \tag{2.47}$$

It has to be pointed out, that ω is merely a parameter of our choosing, defining the rotating frame. With that in mind one can see, that for certain choices the effective potential $\frac{m}{2}R^2\left(\omega(\Omega_\mathrm{c}-\omega) - \Omega_\mathrm{z}^2/2\right)$ vanishes. These frequencies are the single particle *modified cyclotron* ω_+^s and *magnetron frequency* ω_-^s and are given by:

$$\omega_+^\mathrm{s} = \frac{1}{2}\left(\Omega_\mathrm{c} + \sqrt{\Omega_\mathrm{c}^2 - 2\Omega_\mathrm{z}^2}\right) \qquad \omega_-^\mathrm{s} = \frac{1}{2}\left(\Omega_\mathrm{c} - \sqrt{\Omega_\mathrm{c}^2 - 2\Omega_\mathrm{z}^2}\right). \tag{2.48}$$

It can be shown (Major et al., 2005) that the general radial motion of a particle in the laboratory frame is a superposition of oscillatory motions at these frequencies and an oscillation with frequency Ω_z in the decoupled axial direction:

$$\begin{aligned} x(t) &= R_+\cos(\omega_+^\mathrm{s}t + \varphi_+) + R_-\cos(\omega_-^\mathrm{s}t + \varphi_-) \\ y(t) &= -\frac{q}{|q|}\left[R_+\sin(\omega_+^\mathrm{s}t + \varphi_+) + R_-\sin(\omega_-^\mathrm{s}t + \varphi_-)\right] \\ z(t) &= R_\mathrm{z}\cos(\Omega_\mathrm{z}t + \varphi_\mathrm{z}). \end{aligned} \tag{2.49}$$

Here $R_{+;-;\mathrm{z}}$ and $\varphi_{+;-;\mathrm{z}}$ are defined by the initial conditions. The motion in the laboratory frame is illustrated in figure 2.4 for a specific set of parameters.

The treatment of the many–particle case is more difficult and often involves the use of computer simulations. An exception is a "hot" and "large" plasma, for which a mean field description of the particle–particle interaction leads to analytic results. The meaning of "hot" and "large" non-neutral plasmas will be discussed in the upcoming section, together with their dynamics in a Penning trap. In a hot plasma, the mean thermal energy of each particle is dominant over the Coulomb energy with its nearest neighbours. This is quantified by the *coupling parameter* Γ:

$$\Gamma = \left(\frac{1}{4\pi\epsilon_0}\frac{q^2}{a_\mathrm{WS}}\right)(k_\mathrm{B}T)^{-1} \qquad a_\mathrm{WS} = \left(\frac{3}{4\pi n_0}\right)^{1/3}, \tag{2.50}$$

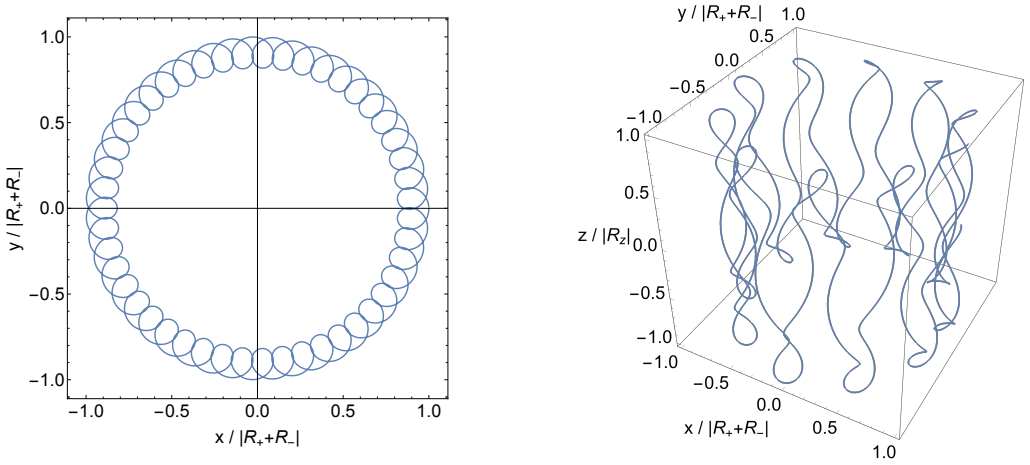

Figure 2.4.: Illustration of the single particle trajectory in a Penning trap, for a specific set of parameters: $\Omega_c = 5\Omega_z$, $R_- = 10R_+$. *Left:* Projection of the motion on the x–y plane. *Right:* 3D plot of particle motion for the same parameters.

where n_0 is the particle density of the plasma, and a_{WS} the corresponding Wigner–Seitz radius. For $\Gamma \ll 1$ correlations between particles are small and the plasma can be described by a Boltzmann distribution:

$$f(\mathbf{R}, \mathbf{V}) = \frac{N \exp\left(-\frac{1}{k_B T}\left(h + \omega p_\Theta\right)\right)}{\int d^3\mathbf{R} d^3\mathbf{V} \exp\left(-\frac{1}{k_B T}\left(h + \omega p_\Theta\right)\right)}, \tag{2.51}$$

where h is the single particle Hamiltonian

$$h = \frac{m}{2} V^2 + q\phi(\mathbf{R}) \tag{2.52}$$

and $\phi(\mathbf{R})$ the mean–field (or Vlasov) electric potential:

$$\phi(\mathbf{R}) = \phi_R(\mathbf{R}) + \underbrace{q \int d^3\mathbf{R}' d^3\mathbf{V}' f(\mathbf{R}', \mathbf{V}') G(\mathbf{R} - \mathbf{R}')}_{=:\phi_P(\mathbf{R})} \tag{2.53}$$

making (2.51) a recursive definition. In equilibrium, the charges in the plasma will arrange themselves in such a way that all electrostatic fields are shielded and (2.53) becomes constant:

$$\phi(\mathbf{R}) = \phi(R, Z) = \phi_R(R, Z) + \phi_P(R, Z) \simeq \text{const.} \tag{2.54}$$

This is where the assumption of a large plasma comes into play, where large means much bigger than fringe effects on the edge of the plasma, which are caused by the thermal

motion of the particles. The size of this region will be quantified at the end of this section. Given that this assumption holds, Poisson's equation $\triangle\phi = -\frac{q}{\epsilon_0} n(R,Z)$ can be used to relate the density of the plasma in the shielding region with the effective potential in the rotating frame:

$$\frac{q^2}{\epsilon_0} n = -q\triangle\phi_{\mathrm{P}} = q\triangle\phi_{\mathrm{R}} = 2m\omega(\Omega_{\mathrm{c}} - \omega), \tag{2.55}$$

where $\triangle\phi_{\mathrm{T}} = 0$ was used. This relation is a powerful statement about the dynamics of a plasma in equilibrium. Given a plasma density n, (2.55) determines ω:

$$\omega_{\pm} = \frac{1}{2}\left(\Omega_{\mathrm{c}} \pm \sqrt{\Omega_{\mathrm{c}}^2 - 2\Omega_{\mathrm{p}}^2}\right) \qquad \Omega_{\mathrm{p}} = \sqrt{\frac{q^2 n}{m\epsilon_0}}, \tag{2.56}$$

with the new definition of the *plasma frequency* Ω_{p}. This can be interpreted in the sense, that in the laboratory frame, the plasma is homogeneously distributed up to a certain surface of revolution and rotates without shear around the axis of symmetry. The possible frequencies are defined by (2.56) and depend on the plasma density, entering Ω_{p}, and the strength of the magnetic field, which is contained in Ω_{c}. It might be surprising that there are two possible rotation frequencies for equal plasma densities. This is explained by the fact that the two solutions correspond to different values of the total energy and angular momentum, where the angular momentum is equal but opposite in sign. Defining these, therefore also defines ω. In the rotating frame, the single particle Hamiltonian expressed for the canonical momentum and using the mean–field potential, can be cast into the shape:

$$h_{\mathrm{R}} = \frac{1}{2m}\left(p_R^2 + \frac{1}{R^2}\left[p_\Theta - \frac{mR^2}{2}\underbrace{(\Omega_{\mathrm{c}} - 2\omega)}_{=:\Omega_{\mathrm{v}}}\right]^2 + p_Z^2\right) + \left[e\phi(R,Z) + \frac{mR^2}{2}\omega(\Omega_{\mathrm{c}} - \omega)\right]. \tag{2.57}$$

Analogously to the single particle motion discussed earlier, this implies rotation with a modified cyclotron frequency, which is denoted *vortex frequency*:

$$\Omega_{\mathrm{v}\pm} = \Omega_{\mathrm{c}} - 2\omega_{\pm} = \pm\sqrt{\Omega_{\mathrm{c}}^2 - 2\Omega_{\mathrm{p}}^2}. \tag{2.58}$$

The plasma dynamics can therefore be summarised as follows: for a given density n and magnetic field B, the plasma rotates as a whole around the trap–symmetry axis with frequency $\omega_{\pm}$, where the sign is defined by the total energy and angular momentum. The individual particles perform an additional rotation at frequency $\Omega_{\mathrm{v}\pm}$, where the sign is defined by $\omega_{\pm}$. For $\omega_{\pm} = \frac{\Omega_{\mathrm{c}}}{2}$ the vortex rotation vanishes and the plasma becomes a rigid rotator. This case equally constitutes the highest possible compression of the plasma, and is called the *Brillouin limit* with the corresponding density:

$$n_{\mathrm{B}} = \frac{B^2\epsilon_0}{2m}. \tag{2.59}$$

It still needs to be quantified, to which extent the fringe effects of the plasma can be neglected. To this end, it is instructive to look at the following thought experiment. Imagine a neutral plasma of mobile negative charges of density n_n embedded in a background of fixed positive charges with equal density $n_\mathrm{p} = n_\mathrm{n}$. If a plane and perfectly transparent mesh is used to define the potential ϕ_0 at $x = 0$, the mobile negative charges will redistribute and try to shield out the newly present electric field[3]. This effort of the charges is hindered by their thermal motion which only allows perfect shielding at larges distances from the mesh. By analysing the shielding in the vicinity of the mesh, the fringe size of non–neutral plasmas can be estimated.

Again assuming a hot plasma, the negative charges are described by (2.51). While it is not shown here, it can be deduced that the equilibrium density distribution of the negative charges is given by (Chen, 1984, p.8; Dubin and O'Neil, 1999, p.95):

$$n_\mathrm{n}(x) = n_\infty \exp\left(\frac{e\phi(x)}{k_\mathrm{B}T_\mathrm{n}}\right), \tag{2.60}$$

where $n_\infty = n_\mathrm{p} = \text{const.}$ is the plasma density at infinity where $\phi(x)$ vanishes. The electric potential has to satisfy Poisson's equation:

$$\epsilon_0 \triangle\phi(x) = \epsilon_0 \frac{\partial^2\phi(x)}{\partial x^2} = -e(n_\mathrm{p} - n_\mathrm{n}(x)) \tag{2.61}$$

which after substitution of (2.60) leads to:

$$\epsilon_0 \frac{\partial^2\phi(x)}{\partial x^2} = e n_\infty \left(\exp\left(\frac{e\phi(x)}{k_\mathrm{B}T_\mathrm{n}}\right) - 1\right). \tag{2.62}$$

The fringe region is characterised by the fact, that the thermal motion dominates over the electric potential $e\phi(x) \ll k_\mathrm{B}T_\mathrm{n}$. It is therefore possible to expand the term in brackets into a Taylor series: $\exp\left(\frac{e\phi(x)}{k_\mathrm{B}T_\mathrm{n}}\right) - 1 = \frac{e\phi(x)}{k_\mathrm{B}T_\mathrm{n}} + \frac{1}{2}\left(\frac{e\phi(x)}{k_\mathrm{B}T_\mathrm{n}}\right)^2 + \ldots$. Using this leads to the approximation:

$$\frac{\partial^2\phi(x)}{\partial x^2} \simeq \frac{e^2 n_\infty}{\epsilon_0 k_\mathrm{B}T_\mathrm{n}}\phi(x). \tag{2.63}$$

This motivates the definition of the so–called *Debye length* which gives a length scale of the shielding in a plasma:

$$\lambda_\mathrm{D} = \sqrt{\frac{\epsilon_0 k_\mathrm{B}T}{ne^2}}. \tag{2.64}$$

Saying that a plasma is large, therefore refers to its dimensions being much bigger than its corresponding Debye length. This equally means, that fringe effects only affect a small region on the periphery of the plasma.

[3]It is assumed, that the mesh is isolated and no recombination with the charges can occur.

2.4.3. Centrifugal separation

While Penning traps can only confine either negatively or positively charged particles due to the dependence of (2.45) on the sign, their respective charge to mass ratios $\rho_i = \frac{q_i}{m_i}$ can vary. It is therefore possible to trap species with different ρ_i in the same trap. The interaction of the particles with each other and with the trapping field then leads to additional plasma dynamics. A practically very important effect is so–called centrifugal separation, which can occur if multiple species with varying ρ_i are confined in the same trap. While a detailed treatment is out of the scope of this thesis (see Dubin and O'Neil, 1999, p.106), it is interesting to discuss the qualitative nature of this effect.

Two particles with charge to mass ratios $\rho_1 < \rho_2$ at the same radius in the trap are rotating at different speeds. The Coulomb interaction therefore leads to a drag force that causes the species with lower ρ to move towards the center, while the other moves outward. This causes the plasma to form radial shells for each ρ_i, which, due to the long range nature of the Coulomb interaction, are separated from each other. The degree of the separation depends on the temperature and density of the plasma and is quantified by the Debye length (2.64). A pictorial example of the phenomenon can be found in section 2.5.1.

2.5. Simulation of different cooling schemes in a Penning trap

The following two subsections present simulations that were performed to evaluate different implementations of the laser cooling. They resulted in two publications, which are reproduced in subsections 2.5.1 and 2.5.2. The first one discusses Doppler selective photodetachment cooling and standard Doppler cooling on the $X^2\Sigma(v'' = 0) \leftrightarrow A^2\Pi(v' = 0)$ transitions. In addition, the effects of the centrifugal separation on the sympathetic cooling are discussed for the case of $C_2{}^-$ and antiprotons in a Penning trap. The second publication discusses a novel approach on laser cooling, using the optical dipole force exerted by a high intensity laser. It also includes a discussion of the sympathetic cooling performance of particles in the mass range of $1 - 50\,\mathrm{u}$ by $C_2{}^-$.

2.5.1. Publication: Photodetachment and Doppler laser cooling of anionic molecules

This publication is referenced as (Gerber et al., 2018). The author of this thesis contributed its main content, which are the simulations and the graphs which present their results, as well as parts of the text.

New Journal of Physics
The open access journal at the forefront of physics

Deutsche Physikalische Gesellschaft DPG
IOP Institute of Physics

Published in partnership with: Deutsche Physikalische Gesellschaft and the Institute of Physics

OPEN ACCESS

RECEIVED
10 October 2017

REVISED
22 December 2017

ACCEPTED FOR PUBLICATION
19 January 2018

PUBLISHED
7 February 2018

PAPER

Photodetachment and Doppler laser cooling of anionic molecules

Sebastian Gerber[1,3,4], **Julian Fesel**[1,3], **Michael Doser**[1] and **Daniel Comparat**[2]

[1] CERN, European Laboratory for Particle Physics, 1211 Geneva, Switzerland
[2] Laboratoire Aimé Cotton, CNRS, Université Paris-Sud, ENS Paris Saclay, Université Paris-Saclay, Bât. 505, F-91405 Orsay, France
[3] These authors contributed equally to this work.
[4] Author to whom any correspondence should be addressed.

E-mail: sebastian.gerber@cern.ch

Keywords: non neutral plasma, anionic molecules, sympathetic Doppler cooling, Penning trap

Abstract

We propose to extend laser-cooling techniques, so far only achieved for neutral molecules, to molecular anions. A detailed computational study is performed for C_2^- molecules stored in Penning traps using GPU based Monte Carlo simulations. Two cooling schemes—Doppler laser cooling and photodetachment cooling—are investigated. The sympathetic cooling of antiprotons is studied for the Doppler cooling scheme, where it is shown that cooling of antiprotons to subKelvin temperatures could becomes feasible, with impacts on the field of antimatter physics. The presented cooling schemes also have applications for the generation of cold, negatively charged particle sources and for the sympathetic cooling of other molecular anions.

1. Introduction

Atomic and molecular anions are relevant in a variety of different fields starting from the chemistry of highly correlated systems [1], the studies of planetary atmospheres [2], negative superhalogens [3] to the interstellar medium [4, 5]. The study of the processes in which the anions are involved is currently hampered by their synthesis at ultracold temperatures. Up to now, temperatures of at best several Kelvin have been achieved via supersonic expansion of anionic gas followed by resistive, buffer gas or electron cooling in cryogenic environments [6–11]. The utilization of laser cooling techniques, routinely used for neutrals, positive ions and neutral molecules (SrF, YO, CaF) [12–14], could for the first time allow the investigation of anionic systems at subKelvin temperatures. In a broader perspective, cooling even a single anion species would enable one to cool any other negatively charged particles via sympathetic cooling including e^-, atomic and molecular anions and antiprotons. The latter are relevant for antihydrogen ($\bar{H}$) experiments, since even though first spectroscopic results on the 1S–2S transition of $\bar{H}$ have been recently obtained [15], their current sensitivity to CPT violations is not yet competitive with that obtained with antiprotons [16, 17] or positrons [18]. Further, measuring the gravitational interaction between matter and antimatter with similar precisions as has been accomplished for matter experiments [19, 20] requires full control of the external and internal state of $\bar{H}$ and temperatures below mK. More generally, the precision of future $\bar{H}$ experiments strongly correlates with the temperature at which $\bar{H}$ can be prepared. Current techniques that rely on forming $\bar{H}$ by interacting $\bar{p}$ and e^+ which have been pre-cooled in a cryogenic Penning trap achieve $\bar{H}$ temperatures in the region of 10 K [15]. The creation of ultracold $\bar{H}$ via the resonant charge exchange of antiprotons with ortho-positronium (o-Ps) is potentially, limited only by the recoil limit of the constituents [21].

This goals of obtaining ultracold $\bar{H}$ has recently sparked theoretical and experimental investigations to use laser-cooled atomic anions like Os^- and La^- [10, 22–24]. As another approach to this yet-to-be-realized procedure, molecular anions are a potential candidate for laser cooling down to the mK regime and have been studied in [11]. In [25] a Sisyphus cooling scheme using optical dipole forces was investigated including the sympathetic cooling of other anions. Here, similarly to Doppler cooling, optical dipole force cooling relies on multiple lasers that repump the population of the coolant in a quasi closed cycle.

In this article, an easy-to-implement scheme relying only on two optical transitions is presented as photodetachment cooling. In this scheme, a selective fraction of C_2^- molecules with high kinetic energies can be

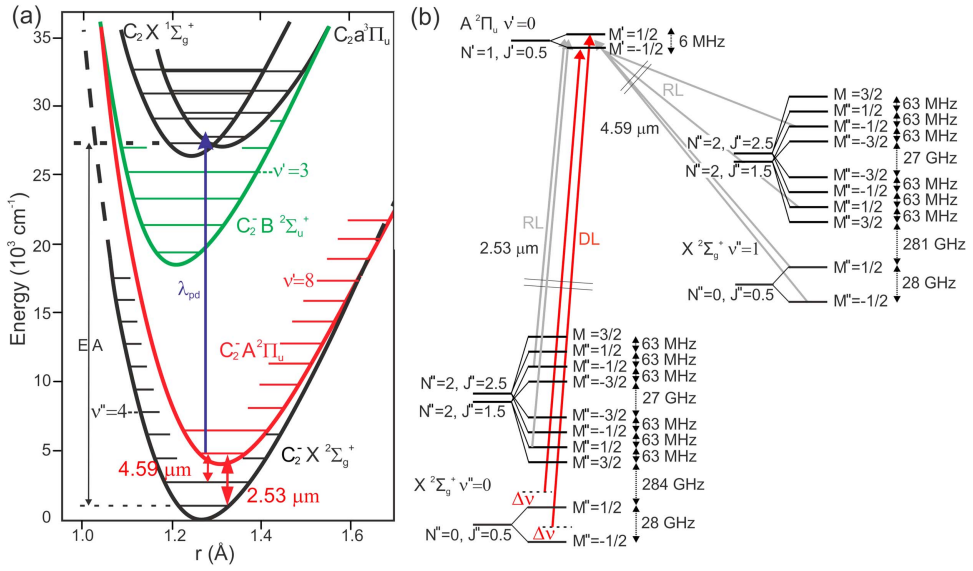

Figure 1. (a) Molecular potential energy of C_2^- versus internuclear separation with the electronic and vibrational levels including two neutral C_2 ($X^1\Sigma_g^+$, $a^3\Pi_u$) curves [37]. The *X*–*A* (red) cooling transitions and the photodetachment (blue, λ_{pd}) transition are indicated with arrows. (b) Zeeman splitted vib–rot sublevels in a 1 T field showing the laser for the Doppler cooling scheme. The electron spin $\frac{1}{2}$ is coupled to the rotational quantum number *N* to form the full angular momentum *J* and its projection *M* on the magnetic field axis. The $v'' = 0$ and $v'' = 1$ manifold of the *X* state and the excited *A* states are shown (not to scale). The two Doppler cooling lasers (DL, red) addressing the ground states at 2.54 μm are depicted with their detunings $\Delta\nu$. The six repumping lasers are sketched (RL, gray) at 2.54 μm and 4.59 μm, respectively. Reproduced from [25]. CC BY 4.0.

removed by two-stage laser induced photodetachment, hereby reducing the temperature of the remaining particles after reaching plasma equilibrium once again. While commonly applied for the spectroscopy of anionic systems [26, 27] and recently for the controlled manipulation of the internal states of molecular anions [28], photodetachment is, to our knowledge, for the first time investigated for the purpose of cooling trapped anions in Penning traps. In [29] evaporative cooling of anions in a rf trap was theoretically investigated using one laser slightly detuned below the photodetachment threshold. Further, in this article the feasibility of the sympathetic cooling of antiprotons in a Penning trap under realistic experimental conditions are discussed using the Doppler cooling method. Both studies are performed on the molecular anion C_2^-. Among many possible candidates, C_2^- has the advantage of a well-known level structure and due to its homonuclear character the $B^2\Sigma_u^+ \rightarrow A^2\Pi_u$ decay channel is forbidden [30–34]. Furthermore, it has well suited branching ratios between $B^2\Sigma(v' = 0) \leftrightarrow X^2\Sigma(v'' = 0)$ ground vibrational states of 72% and between $A^2\Pi_{1/2}(v' = 0) \leftrightarrow X^2\Sigma(v'' = 0)$ of 96%. In comparison to atomic La^-, molecular C_2^- has a similar dipole transition but exhibits no unwanted photodetachment, no hyperfine structure and can be produced at low sub-eV kinetic energies [35]. Figure 1(a) shows an overview of the electronic and vibrational level structure of C_2^- and C_2. The potential curves of the molecule were calculated using the empirical function proposed in [36], using spectroscopic parameters from [32, 37]. The vibrational levels are based on constants from [37]. For C_2 the curves where shifted by the electron affinity EA = 3.269. The rot–vib and electronic spectra of C_2^- were simulated using the program PGOPHER [38].

2. Sympathetic Doppler cooling of $C_2^-/\bar{p}$

C_2^- can be produced from plasma discharge of acetylene with internal energies in the sub-eV range at densities of 10^{13} m^{-3} [35, 39]. After selection of C_2^- in a mass spectrometer, the anions can be trapped in a Penning trap. In sequence, $\bar{p}$ can be trapped in the same Penning trap at a different axial position. Starting from typical experimental conditions that are achieved at CERN's Antiproton Decelerator facility approximately 10^5 $\bar{p}$ can be caught and initially electron-cooled to eV kinetic energies [15, 40–42]. The $\bar{p}$ can then be mixed with the C_2^- and with priorly loaded e^- using potential manipulations, similarly as demonstrated in the preparation of different charge-to-mass-ratio species plasmas [43, 44]. Using electron cooling after the mixing process and considering a 1 T Penning trap at 10 K, temperatures of the $C_2^-/\bar{p}/e^-$ ensemble around 100 K can be realized within a few tens of seconds [45]. Subsequently, by lowering the axial trapping potential confining the particles allows for additional evaporative cooling and the preparation of the mixed plasma at about 10 K [46].

In the trap the $\mathbf{E} \times \mathbf{B}$ field causes an azimuthal drift of the particles about the magnetic field axis. At a same radius the difference in mass of the two species will result in a difference in centrifugal force and with that

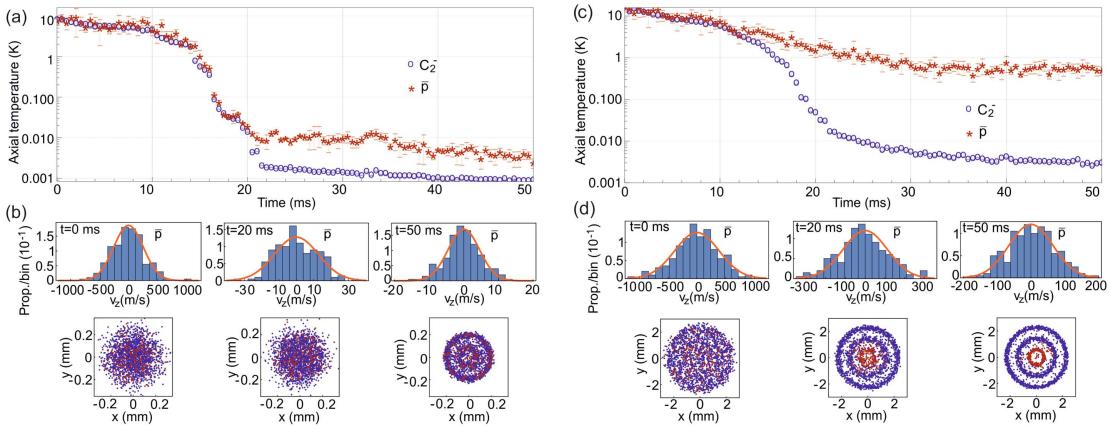

Figure 2. Simulation of sympathetic cooling in a 1 T Penning trap for a Coulomb factor of (a) $C_f = 1$ and (c) $C_f = 5000$ using a Doppler cooling force scaled by 10^4, see text for details. The confidence intervals are obtained from Boltzmannian fits to the particle velocity distributions. The temperature evolution of 1848 C_2^- (solid, red) and 200 $\bar{p}$ (dotted, blue) are calculated. In both plots the laser detunings are adjusted to the half width of the Doppler broadened Voigt profile in 4 steps from $\Delta\nu = -39$ MHz to $\Delta\nu = -3.4$ MHz using a laser linewidth of $\delta\nu = 1$ MHz. Histogram of the axial velocity distribution in (b) for $C_f = 1$ and (d) for $C_f = 5000$ together with the radial plasma profile for three corresponding times for C_2^- (red) and $\bar{p}$ (blue).

rotation rate. Collisional drag gives rise to a separation of the particles with the lighter $\bar{p}$ drifting inwards and the heavier C_2^- outwards. In thermal equilibrium the rotation of the plasma is rigid at a frequency ω_r [43]. In the limit of zero Debye length, the density n_j of species j is then determined by ω_r as $n_j = 2\epsilon_0 m_j \omega_r(\Omega_j - \omega_r)/e^2$, with m_j and Ω_j the respective mass and cyclotron frequency [43]. For the case of $\Omega_j \gg \omega_r$ the plasma will evolve to a spheroidal shape with approximately equal densities and $\omega_r = e\,n/(2\epsilon_0 B)$. Axially, the particles oscillate with a frequency $\omega_{z,j} = 2\pi \times \nu_{T,j}/2l_j$, with $\nu_{T,j} = \sqrt{kT_z/m_j}$ the thermal velocity and trapping length l_j.

In order to study the effect of sympathetic cooling, figure 2(a) shows a simulation of Doppler cooling a $C_2^-/\bar{p}$ plasma confined in a 1 T Penning trap. The Coulomb particle–particle interaction and the trapping field is simulated for a total of 1848 C_2^- and 200 $\bar{p}$ with time steps that resolve the cyclotron motion of the $\bar{p}$ including N-body space charge effects. To scale the simulation to experimentally typical particle numbers of $N_{\bar{p}} \sim 10^5$ with a particle ratio of $N_{C_2^-} \sim 10N_{\bar{p}}$ and to investigate possible geometrical plasma effects the Coulomb interaction force between the particles is increased by a factor $C_f = 5000$ without affecting the particle-trap interaction. For this case, the simulation is shown in figure 2(c). The computation is performed on a GPU running on the mass parallel platform CUDA and the N-body algorithm described in [47]. A fifth order Dormand–Prince integrator is used to calculate the force equation each time step [48].

To implement Doppler cooling in the simulation, the lasers are applied along the z-axis and parallel to the magnetic trapping field, that acts as a quantization axis. In this configuration only $\Delta M = \pm 1$ laser transitions are allowed, whereas spontaneous decays from the excited states can occur on $\Delta M = 0, \pm 1$ transitions. Figure 1(b) depicts the relevant vib–rot C_2^- levels in the 1 T field together with the lasers for Doppler cooling. The transition strength probabilities of the excited $|A,\ v' = 0,\ N' = 1\rangle$ state to the X state vibrational levels are $96, 4, 2 \times 10^{-6}$ (percentage of the Franck–Condon); the natural linewidth of the excited state is $\Gamma_{sp} = 2\pi \times 3.13$ kHz [30, 32–34, 37]. Two narrow-band lasers at 2.53 μm address the two $\left|X,\ v'' = 0,\ N'' = 0,\ M'' = \pm\frac{1}{2}\right\rangle \rightarrow \left|A,\ v' = 0,\ N' = 1,\ M' = \mp\frac{1}{2}\right\rangle$ transition. The cooling lasers are red detuned from resonance by $\Delta\nu$. In order to achieve a quasi closed transition cycle of the populations two additional 2.53 μm lasers repump the $|X,\ v'' = 0,\ N'' = 2,\ J'' = 2.5,\ 1.5\rangle$ manifolds with imprinted sideband structures at 63 MHz (The power ratios of the carrier, first and second order sideband are considered with a modulation index of 1.8 as $I0 \approx 2I1 \approx I2$). Each repump laser then addresses four $\Delta M = \pm 1$ transitions. From each of the two excited A states there are six allowed $\Delta M = 0, \pm 1$ transitions back to X into the $J'' = 1.5, 2.5$ states and two transitions into the $J'' = 0.5$ states. In a similar way, a total of four additional repump lasers at 4.59 μm are required to address the $|X,\ v'' = 1\rangle$ ro–vib levels. In total 20 laser induced transitions and 32 spontaneous decays are to be considered for the quasi closed cycle.

In the limit of $\Gamma_{sp} \ll \delta\nu$, assuming typical IR-DFB laser linewidths of a few MHz in the simulation, the average cooling force from the Doppler cooling transitions [49, 50] is calculated for each time step using Einstein's rate equations [51]. In steady-state the population is then evenly distributed between all molecular substates. Thus, molecules resonant with the detuned Doppler lasers are selected in the force equation and experience a net cooling force $F_i = lA_i\hbar k_i$ per time step, with k_i the wave vector of the respective cooling transition i. Here, A_i is the Einstein coefficient of one of the two Doppler cooling transitions and l is the fraction of the steady-state population in the excited state as $l = 1/\sum_j = 0.045$, as inverse to the number of all levels j from figure 1(b). For the simulation, the

Doppler and repumper lasers are calculated with circular polarizations and linewidths of $\delta\nu = 1$ MHz and linear polarizations and linewidths of $\delta\nu = 3$ MHz, respectively. For all lasers a power of 3 mW and a waist of 1.5 mm is used. The resulting average cooling force leads to a cooling time on the order of several seconds per Kelvin. In order to simulate the plasma evolution over a wide temperature range within practically accessible simulation times the cooling force used in the following simulations is increased by a factor of 10^4.

The particles are initialized at a temperature of ~10 K and at a density of $n = 8 \times 10^{11}$ m^{-3}. For the case of $C_f = 1$ in figure 2(a) cooling of the C_2^- together with sympathetic cooling of $\bar{p}$ is seen to temperatures of ~4 mK after 50 ms. Without the factor 10^4 increase in the cooling force and for the parameters used in figure 2, the average number of scattered photons then corresponds to 1.3×10^5, with the velocity removed per photon recoil from the two cooling transitions as $\Delta v_i = \hbar k_i / m_{C_2^-}$. Due to the unpumped $|X,\ v'' = 2\rangle$ states, after Doppler cooling a total of 26% of the anions are then expected to end up in these excited vibrational states.

For the plots in figure 2, the temperature values are obtained from Boltzmannian fits of the velocity histograms in axial z direction, pictured in figure 2(b) for $\bar{p}$ at three different times together with the corresponding radial plasma profiles in the x–y plane. At C_2^- temperatures of 1.3 mK the coupling parameter that describes the correlated system as $\Gamma = e^2/(4\pi\epsilon_0 akT)$ with the Wigner–Seitz radius $a = (3/4\pi n)^{1/3}$ approaches values of $\Gamma \sim 174$, where the first-order liquid-solid phase transition to a crystalline plasma state is expected. The crystallization process is visible in the formation of radial plasma patterns as a function of the plasma aspect ratios, density and magnetic field [52], which are precursors to the formation of bcc-lattice planes [43]. For the present trapping geometry two shells are exhibited with an outer plasma radius of $R_p = 0.2$ mm. No pronounced centrifugal separation of the two species is visible, with the separation length defined by $l_{sep} = kT/(|m_{C_2^-} - m_{\bar{p}}|\omega_r^2 R_p)$ reaching values of R_p for temperatures of $T \sim 10$ mK [43]. In figure 2(c) using $C_f = 5000$ and leaving all other parameters identical the particles attain temperatures of 3 mK and 500 mK for C_2^- and $\bar{p}$, respectively, after a simulated time of ~50 ms with the onset of a temperature difference at about 3 K. Introducing the Coulomb factor C_f effectively scales the coupling parameter $\Gamma_c = C_f^{2/3}\Gamma$ with $a_c = C_f^{1/3}a$. At 3 K Γ_c yields about 174, where the formation of three radial shells are visible for the present parameters. Here, with $l_{sep} \ll R_p$ centrifugal separation of the two species starts to be visible at a simulated cooling time of 20 ms with the lighter $\bar{p}$ predominantly concentrated in the inner shell limiting the sympathetic cooling via viscous drag to the outer C_2^-. Further, by increasing C_f close binary collisions dominate to produce equipartition of the axial and radial motions, where the equipartition rate becomes exponentially small with increasing b/r_c, the ratio of the distance of the closest approach $b = e^2/(4\pi\epsilon_0 kT_z)$ and the cyclotron radius $r_c = v_{Tj}/\Omega_j$ of the two species [53, 54]. This effect further contributes to the observed difference in final temperature between the C_2^- and $\bar{p}$.

We have further checked an intermediate simulation using $C_f = 100$ where the onset of the temperature difference occurs at about 0.2 K with the final temperatures of 30 mK for $\bar{p}$ and 10 mK for C_2^- consistent with a crystallization and the Γ_c scaling. The simulations shown in figure 2 indicate that for the typical parameters considered, sympathetic cooling of $\bar{p}$ using C_2^- is expected to work over a large range of temperatures down to subKelvin. Further, the sympathetic cooling occurs within about 1 ms in agreement with [55] on time scale much faster than the effect of the amplified Doppler cooling. This still holds for the simulation including a Coulomb factor.

3. Photodetachment cooling of C_2^-

To cool species with multilevel structures such as C_2^- using the Doppler scheme requires mastering a full set of lasers to absolute frequency precisions on the order of MHz. Additionally, for species faced with narrow dipole transitions cooling times of the order of minutes have to be considered against plasma heating rates in Penning traps [56]. As a different cooling method we shall now study photodetachment cooling relying on only two lasers. Here, a Doppler selective laser with energy $E_D = hc/2.53\ \mu$m (1 MHz, 3 mW) and a waist of 1 mm addresses the $\left|X,\ v'' = 0,\ N'' = 0,\ M'' = \frac{1}{2}\right\rangle$ ground state. By that a fraction of molecules in a velocity window resonant with the laser field is transferred to the excited state $\left|A,\ v' = 0,\ N' = 1,\ M' = \frac{1}{2}\right\rangle$; for cooling the laser frequency is chosen to select molecules with high kinetic energy. From the excited A state, a second laser at λ_{pd} then transfers the population above the photodetachment threshold, EA, splitting C_2^- into neutral C_2 and photoelectrons, see figure 1(a).

In order not to address the ground states the energy of the photodetachment laser $E_{pd} = hc/\lambda_{pd}$ must be $E_{pd} < \mathrm{EA}$. The corresponding total photodetachment cross section σ_A from the state $|A,\ v' = 0\rangle$ for varying photon energy E_{pd} can be calculated as the sum over the partial cross sections σ_p for all quantum numbers i of the C_2 states obeying energy conservation, $\sigma_A(E_{pd}) = \sum_i \sigma_p P_{FC}$ [57, 58], where σ_p is derived by Geltman for homonuclear diatomic anions in [59] and P_{FC} is the relative weight of the transition given by the Franck–Condon factor. A calculation including the molecular potential energies shown in figure 1(a) results in a lower limit of $\sigma_A/\mathrm{cm}^2 = 3.5 \times 10^{-17}$ [60, 61]. The cross section for E_{pd} close to the threshold $\mathrm{EA} - E_D$ is significantly lower reaching $\sigma_A/\mathrm{cm}^2 \sim 1 \times 10^{-19}$. The expected photodetachment rate is then given by $\Gamma_{pd} = \sigma_A I/E_{pd}$ for a laser intensity I and has to be seen in comparison to the total natural decay rate of the excited state of $\Gamma_{sp} = 19.7\ \mathrm{ms}^{-1}$ [32, 33]. Experimentally $\Gamma_{pd} > \Gamma_{sp}$ can, for example, be realized with a frequency-doubled Ti:sapphire laser system

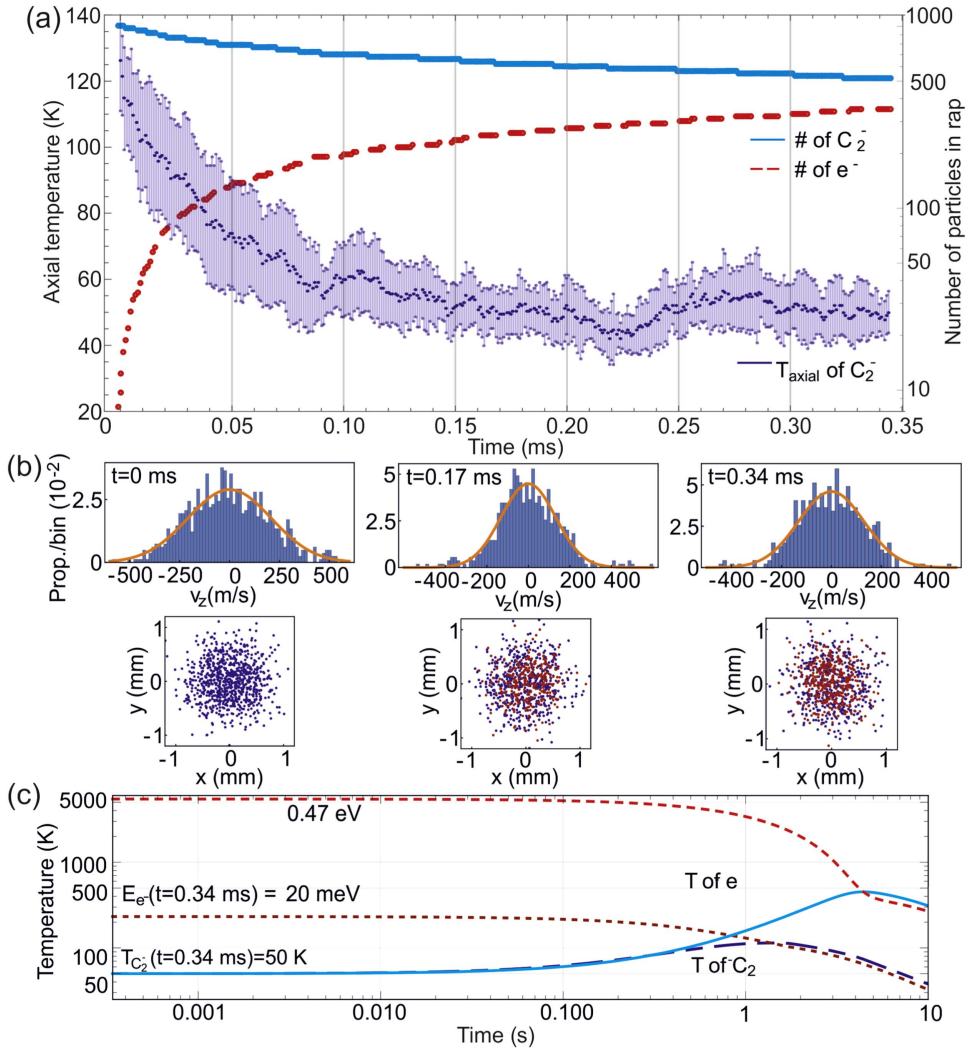

Figure 3. (a) Simulation of photodetachment cooling in a 1 T Penning trap at $C_f = 1$ and $E_{e^-} = 20$ meV, see text for detail. The temperature evolution of initially 1000 C_2^- (blue) is simulated together with the created photoelectrons. The initial laser detuning of the 2.53 μm laser is set to 1σ of the initial Doppler profile width as $\Delta\nu = 116$ MHz and is linearly swept to $\Delta\nu = 84$ MHz. (b) Velocity histograms at three different times with the corresponding radial plasma profile of C_2^- (blue) and e^- (red). (c) Calculation of the C_2^-/e^- temperature evolution caused by photoelectrons with energy $E_{e^-} = 0.46$ eV for C_2^- (solid, blue) and e^- (dashed, red) and $E_{e^-} = 20$ meV for C_2^- (dashed–dotted, dark blue) and e^- (dotted, dark red). $N_{C_2^-}/N_{e^-} = 1.5\ \eta$ and initial $T_{C_2^-} = 50$ K.

enhanced in a low finesse cavity at 380 nm (3.26 eV) close to the *EA* threshold. While the neutral C_2 molecules will escape the trapping potential after photodetachment of C_2^-, the released photoelectrons will continue to Coulomb-interact with the plasma. The photoelectrons' angular distribution hereby depends on the angular momentum of C_2^-. The distribution can be described by the Cooper–Zare model [62, 63] and for simplicity will be approximated by an isotropic character for the following simulation. The kinetic energy of the photoelectrons is dominated by the residual binding energy given by the difference between the combined photon energy and the photodetachment threshold, $E_{e^-} = E_{\mathrm{pd}} + E_D - \mathrm{EA}$, and can take values of $E_{e-} < 0.47$ eV. Only the fraction of released electrons which have a kinetic energy projection along the trap axis smaller than the axial confinement potential of the space charge plasma U will stay trapped. This can be expressed by the limit angle $\beta = \mathrm{acos}\,(\sqrt{U/E_{e^-}})$ that defines the fraction of trapped photoelectrons as $\eta = 1 - \int_0^{\beta} \sin(\phi)\,\mathrm{d}\phi$. These electrons will thus continue to equilibrate with the plasma due to Coulomb collisions and their coupling to the black-body radiation of the environment.

The described processes are simulated in figure 3(a) for 1000 C_2^- particles in a 1 T Penning trap for a photodetachment rate of $\Gamma_{\mathrm{pd}} = 85\ \mathrm{ms}^{-1}$ and an axial confinement of $U = 20$ mV. Employing Einstein's optical rate equations on all relevant transitions shown in figure 2(b), the pumping and photodetachment process is included using the Monte Carlo method. In the simulation, the plasma is first initialized at a density of $n = 5 \times 10^{12}\ \mathrm{m}^{-3}$ and $T = 120$ K, which ranges close to temperatures measured using electrostatic plasma modes [64]. The 2.53 μm laser is blue-detuned from resonance to address only the fraction of anions with a high kinetic energy before interacting with a light field at $\lambda_{\mathrm{pd}} = 442$ nm. At this wavelength $E_{e^-} = 20$ meV and all e^- are trapped, $\eta = 1$. By this, molecules with high kinetic are removed from the trapping fields. After reaching

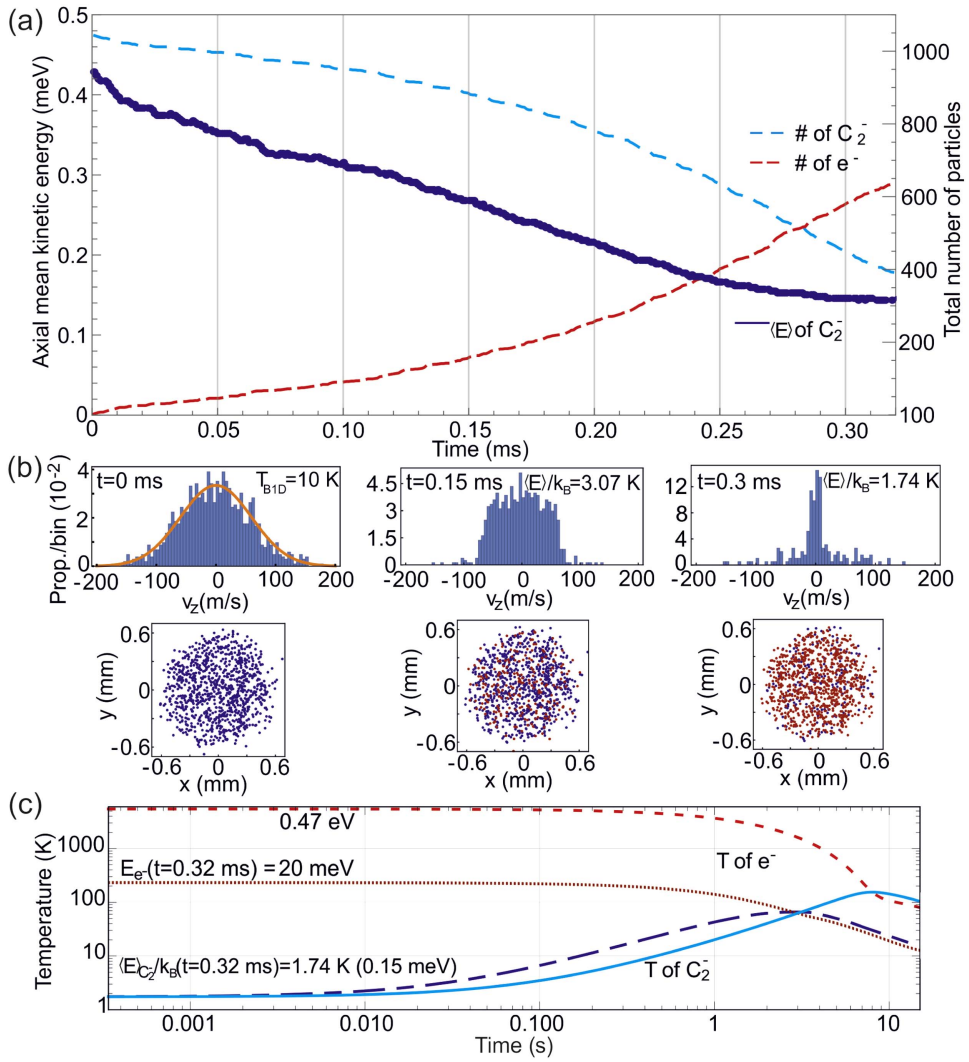

Figure 4. Photodetachment cooling simulation for C_2^- at $C_f = 1$ in a 1 T trap. (a) Evolution of the axial kinetic energy of 1100 molecules after initialization in thermal equilibrium at $T = 10$ K and $E_{e+} = 20$ meV. The detuning of the 2.53 μm laser is linearly swept from initial $\Delta\nu = 60$ MHz to $\Delta\nu = 16$ MHz. (b) Radial plasma profile of C_2^- (blue) and e^- (red) at three different times together with the velocity histograms showing the Boltzmann fit at initialization and two distributions with the corresponding mean kinetic energy in Kelvin. (c) Temperature evolution for the case of photoelectron energies of $E_{e^-} = 0.46$ eV for C_2^- (solid, blue) and e^- (dashed, red) and for $E_{e^-} = 20$ meV for C_2^- (dashed–dotted, dark blue) and e^- (dotted, dark red). $N_{C_2^-}/N_{e^-} = 0.7\ \eta$, for $\langle E\rangle_{C_2^-}/k_B = 1.74$ K.

equilibrium once again [65], the remaining C_2^-/e^- plasma are left with a mean reduced temperature. This process is very similar to evaporative cooling as performed with neutral atoms [66]. The number of C_2^- in the trap decreases until it reaches a saturation level after ~0.35 ms, which is determined by loss of C_2^- in unpumped molecular states. The confidence intervals are obtained from Boltzmannian fits to the particle velocity distribution shown in figure 3(b) together with the radial plasma profiles. The temperature evolution for longer time scales >0.35 ms caused by the released photoelectrons is shown in figure 3(c) for $\lambda_{pd} = 442$ nm and for the case of 380 nm ($E_{e^-} = 0.47$ eV, $\eta = 0.21$). Here a coupled rate equation calculation of the C_2^-/e^- plasma is performed including synchrotron radiation [45] in the trapping field. The final parameters of the GPU simulation from figure 3(a) at $t = 0.34$ ms are used as input values for figure 3(c) as the particle number ratio and the initial temperature of C_2^- and e^-. Here, the temperature of the C_2^- initially follows similar behavior for different photodetachment conditions. After approximately 2–5 s the system reaches temperatures of 100–400 K for increasing e^- energies before electron cooling dominates. From these two plots one infers that for the considered density, B field and initial C_2^- temperature the photoelectron heating occurs on a time scale about 30 times longer than the photodetachment cooling. Thus, in the overall temperature dynamics a temperature minimum is seen after ~0.35 ms at 50 K and is found to be robust for different E_{e-}. It is thus this difference of time scales of the competing processes which allows for the technique of photodetachment cooling. Measurements at cold temperature can be then performed in an experimental window of ~100 ms.

In figure 4 photodetachment cooling is studied for C_2^- at 10 K after electron cooling to the liquid helium Penning trap environment [67]. At this temperature the cooling is initialized with identical trap and laser

parameters as in figure 3. The result of the Monte Carlo simulation using 1100 C_2^- molecules is depicted in figure 4(a). The mean kinetic energy of all anions is calculated from the square of the mean velocities from the histograms shown in figure 4(b). A temperature reduction of a factor of ~5.5 is seen for a C_2^- number decrease by a factor of 2.5 after ~0.32 ms. Figure 4(c) plots the thermalization of C_2^- and photoelectrons for a longer time scale >0.32 ms using rate equations [45] for two different E_{e-}. A window of approximately 10 ms can be used to perform measurements on cold anions which is sufficient for spectroscopic analysis of C_2^- of any sympathetically cooled negative species or pulsed antihydrogen formation [21].

4. Summary

A detailed computational study including all influencing trapping and optical parameters was performed using GPU aided simulations for laser cooling of C_2^- anions and the sympathetic cooling of $\bar{p}$ stored in Penning traps. Photodetachment cooling is discussed for the first time as an accessible method to generate anions in the subKelvin regime. For the typical density and temperature range investigated, this scheme relies on a system of only two commercially available lasers and allows for an approximately 10 ms long time window at ultracold temperatures for experimental measurements. The time window is found to be robust for a wide range of photodetachment energies. Further it was shown, by investigating Doppler cooling, that C_2^- could be a suitable sympathetic coolant for $\bar{p}$ in cryogenic environments enabling their preparation at lower temperatures than currently achieved. Additionally, starting photodetachment cooling at even lower energies, e.g. after Doppler cooling or using a trap at dilution refrigerator temperatures could potentially assist in the preparation of an ensemble of mK $\bar{p}$. This step would permit the resonant charge exchange formation of ultracold antihydrogen [21] (by employing available pulsed positronium sources [68]) and thus allows sensitive studies of CPT symmetries and of the WEP with neutral antimatter systems.

Acknowledgments

We like to thank Viatcheslav Kokoouline for performing the cross section calculations for C_2^-. The research leading to these results has received funding from the European Research Council under Grant Agreement No. 277762 COLDNANO.

ORCID iDs

Sebastian Gerber https://orcid.org/0000-0001-5101-1250

References

[1] Jin D S and Ye J 2012 *Chem. Rev.* **112** 4801–2
[2] Biemann K 2006 *Nature* **444** E6
[3] Freza S and Skurski P 2010 *Chem. Phys. Lett.* **487** 19–23
[4] Li X and Paldus J 2006 *Chem. Phys. Lett.* **431** 179–84
[5] Simons J 2008 *J. Phys. Chem.* A **112** 6401–511
[6] Gerlich D 1995 *Phys. Scr.* **T95** 256
[7] Deiglmayr J, Goritz A, Best T, Weidemuller M and Wester R 2012 *Phys. Rev.* A **86** 043438
[8] Kumar S S, Hauser D, Jindra R, Best T, Geppert W D, Millar T J and Wester R 2013 *Astrophys. J.* **776** 25
[9] Gabrielse G, Khabbaz A, Hall D S, Heimann C, Kalinowsky H and Jhe W 1999 *Phys. Rev. Lett.* **82** 3198
[10] Jordan E, Cerchiari G, Fritzsche S and Kellerbauer A 2015 *Phys. Rev. Lett.* **115** 113001
[11] Yzombard P, Hamamda M, Gerber S, Doser M and Comparat D 2015 *Phys. Rev. Lett.* **114** 213001
[12] Shuman E S, Barry J F and Demille D 2010 *Nature* **467** 820–3
[13] Hummon M T, Yeo M, Stuhl B K, Collopy A L, Xia Y and Ye J 2013 *Phys. Rev. Lett.* **110** 1–5
[14] Zhelyazkova V, Cournol A, Wall T E, Matsushima A, Hudson J J, Hinds E A, Tarbutt M R and Sauer B E 2014 *Phys. Rev.* A **89** 2–6
[15] Ahmadi M 2017 *Nature* **541** 506–10
[16] Ulmer S *et al* 2015 *Nature* **524** 196–9
[17] DiSciacca J *et al* 2013 *Phys. Rev. Lett.* **110** 130801
[18] Dehmelt H, Mittleman R, Van Dyck R S and Schwinberg P 1999 *Phys. Rev. Lett.* **83** 4694–6
[19] Peters A, Chung K and Chu S 1999 *Nature* **400** 849–52
[20] Müller H, Peters A and Chu S 2010 *Nature* **463** 926–9
[21] Doser M *et al* 2012 *Class. Quantum Grav.* **29** 184009
[22] Kellerbauer A and Walz J 2006 *New J. Phys.* **8** 45
[23] Warring U, Amoretti M, Canali C, Fischer A, Heyne R, Meier J O, Morhard C and Kellerbauer A 2009 *Phys. Rev. Lett.* **102** 043001
[24] Pan L and Beck D R 2010 *Phys. Rev.* A **82** 014501
[25] Fesel J, Gerber S, Doser M and Comparat D 2017 *Phys. Rev.* A **96** 031401
[26] Trippel S, Mikosch J, Berhane R, Otto R, Weidemüller M and Wester R 2006 *Phys. Rev. Lett.* **97** 193003
[27] Kim J, Weichman M, Sjolander T, Neumark D, Klos J, Alexander M and Manolopoulos D 2015 *Science* **349** 510

[28] Hauser D et al 2015 Nat. Phys. 11 467
[29] Crubellier A 1990 J. Phys. B: At. Mol. Opt. Phys. 23 3585–607
[30] Rosmus P and Werner H J 1984 J. Chem. Phys. 80 5085
[31] Mead R D, Hefter U, Schulz P A and Lineberger W C 1985 J. Chem. Phys. 82 1723
[32] Špirko T and Šedivcová V 2006 Mol. Phys. 104 1999
[33] Jones P L, Mead R D, Kohler B E, Rosner S D, Lineberger W C, Jones P, Mead R D, Kohler B E, Rosner S D and Unebergerll W C 1980 J. Chem. Phys. 73 4419
[34] Shan-Shan Y, Xiao-Hua Y, Ben-Xia L, Kakule K, Sheng-Hai W, Ying-Chun G, Yu-Yan L and Yang-Qin C 2003 Chin. Phys. 12 745
[35] Tulej M, Knopp G, Gerber T and Radi P P 2010 J. Raman Spectrosc. 41 853–8
[36] Zavitsas A A 1991 J. Am. Chem. Soc. 113 4755–67
[37] Ervin M K and Lineberger W C 1991 J. Phys. Chem. 95 1167–77
[38] Western C M 2017 J. Quant. Spectrosc. Radiat. Transfer 186 221–42
[39] Rehfuss B D, Liu D J, Dinelli B M, Jagod M F, Ho W C and Oka T 1988 J. Chem. Phys. 89 129–37
[40] Gabrielse G et al 2008 Phys. Rev. Lett. 100 113001
[41] Amsler C and Ariga A 2016 J. Phys.: Conf. Ser. 755 011001
[42] Enomoto Y et al 2010 Phys. Rev. Lett. 105 1–4
[43] Dubin D H E and O'Neil T M 1999 Rev. Mod. Phys. 71 87
[44] Jelenković B, Newbury A, Bollinger J, Itano W and Mitchell T 2003 Phys. Rev. A 67 63406
[45] Rolston S L and Gabrielse G 1989 Hyperfine Interact. 44 233–45
[46] Andresen G B et al 2010 Phys. Rev. Lett. 105 1–5
[47] Nyland L, Harris M and Prins J F 2007 GPU Gems 3 677–96
[48] Gorp S V and Dupre P 2013 AIP Conf. Proc. 1521 300
[49] Wineland D J and Itano W M 1979 Phys. Rev. A 20 1521
[50] Eschner J, Schmidt-Kaler F and Blatt R 2003 J. Opt. Soc. Am. B 20 1003
[51] Höppner R, Roldán E, Valcárcel G J D and Optica D 2012 Am. J. Phys. 80 882
[52] Totsuji H, Tsuruta K, Totsuji C, Nakano K, Kamon K and Kishimoto T 1999 AIP Conf. Proc. 498 77–82
[53] Jensen M J, Hasegawa T, Bollinger J J and Dubin D H E 2005 Phys. Rev. Lett. 94 025001
[54] Dubin D H E 2005 Phys. Rev. Lett. 94 025002
[55] Anderegg F, Driscoll C F and Dubin D H E 2010 Phys. Plasmas 17 55702
[56] Andresen G et al 2007 Phys. Rev. Lett. 98 023402
[57] Blumberg W A M, Itano W M and Larson D J 1979 Phys. Rev. A 19 139–48
[58] Barrick J B and Yukich J N 2016 Phys. Rev. A 93 023431
[59] Geltman S 1958 Phys. Rev. 112 176–8
[60] Douguet N, Kokoouline V and Greene C H 2008 Phys. Rev. A 77 064703
[61] Kokoouline V 2016 private communication
[62] Sanov A 2014 Annu. Rev. Phys. Chem. 65 341–63
[63] Surber E, Mabbs R and Sanov A 2003 J. Phys. Chem. A 107 8215–24
[64] Amoretti M et al 2003 Phys. Plasmas 10 3056–64
[65] Anderegg F, Dubin D H E, ONeil T M and Driscoll C F 2009 Phys. Rev. Lett. 102 185001
[66] Petrich W, Anderson M H, Ensher J R and Cornell E A 1995 Phys. Rev. Lett. 74 3352
[67] Amole C et al 2012 Nature 483 439–43
[68] Mariazzi S, Bettotti P and Brusa R S 2010 Phys. Rev. Lett. 104 243401

2.5.2. Publication: Optical dipole–force cooling of anions in a Penning trap

This publication is referenced as (Fesel et al., 2017). The author of this thesis wrote the entire publication, performed the simulations and generated the graphs which present the results.

PHYSICAL REVIEW A **96**, 031401(R) (2017)

Optical dipole-force cooling of anions in a Penning trap

Julian Fesel,* Sebastian Gerber, and Michael Doser
CERN, European Laboratory for Particle Physics, 1211 Geneva, Switzerland

Daniel Comparat
Laboratoire Aimé Cotton, CNRS, Université Paris–Sud, ENS Paris Saclay, Université Paris–Saclay, Bâtiment 505, 91405 Orsay, France
(Received 21 December 2016; revised manuscript received 17 July 2017; published 13 September 2017)

We discuss the possibility of using optical dipole forces for Sisyphus cooling of ions stored in a Penning trap by addressing the specific case of the molecular cooling candidate C_2^-. Using a GPU accelerated code for Penning trap simulations, which we extended to include the molecule-light interaction, we show that this scheme can decrease the time required for cooling by an order of magnitude with respect to Doppler cooling. In our simulation we found that a reduction of the axial anion temperature from 10 K to 50 mK in around 10 s is possible. The temperature of the radial degrees of freedom was seen to thermalize to 150 mK. Based on the laser-cooled C_2^-, a study on the sympathetic cooling of anions with masses 1–50 nucleon was performed, covering relevant candidates for investigations of chemical anion reactions at ultracold temperatures as well as for antimatter studies.

DOI: 10.1103/PhysRevA.96.031401

Laser cooling of anions, which has so far never been achieved, would enable the sympathetic cooling of any other negatively charged species and open new opportunities in a variety of research areas. This includes research on the atmosphere and the interstellar medium [1], chemistry of highly correlated systems [2], and cooling of antiprotons for antimatter experiments [3]. Given the broad impact, several groups are exploring different approaches to cool anions [4–6].

Up to now, work on the cooling of anions has focused mainly on the atomic species La^- and Os^- [5–7] and the molecular species C_2^- [4]. They all have in common that the dipole transitions attractive for the cooling can have narrow natural linewidths in the range of several kilohertz. Thus, employing traditional Doppler cooling would result in cooling times on the order of 100 s to reach the 100-mK regime even when starting with particles precooled to the liquid helium temperature of 4 K. This can be a problem when the cooling is in competition with heating effects stemming from, e.g., trap misalignment or collisions with residual gases.

Addressing this problem, we discuss the possibility of using the ac Stark shift for Sisyphus cooling in ion traps [8]. Although also applicable to positive ions, we will concentrate on the specific case of C_2^- in a Penning trap, which is an interesting candidate for sympathetic cooling of antiprotons [3,4]. We will describe the cooling scheme in detail below. Using this method, depending on the laser power available, the energy removed per scattered photon can be much higher than by using the Doppler effect. This results in an accelerated cooling, while also easing the requirements on repumping, which is of special importance for the cooling of molecules.

The level structure of C_2^- is well known and depicted in Fig. 1(a) [10–13]. Given its homonuclear character, only electronic transitions are allowed, resulting in two possible systems for cooling. The first consists of the $B\,^2\Sigma(v'=0,N'=0) \leftrightarrow X\,^2\Sigma(v''=0,N''=2)$ transition at 541 nm, with a branching ratio of 72% for spontaneous decay via this channel and a natural linewidth of $\Gamma = 2\pi \times 2.1$ MHz. In order to create a closed cycle for the cooling it is then necessary to repump several lower vibrational states $X\,^2\Sigma(v''=0,\ldots,4)$, which was simulated for the case of Doppler cooling in a Paul trap in [4]. In the case of a Penning trap high magnetic fields of several tesla result in an additional strong splitting of the rotational sublevels, making the experimental realization of the repumping challenging.

We will therefore focus on the second possible system for cooling. This consists of the $A\,^2\Pi(v'=0) \leftrightarrow X\,^2\Sigma(v''=0)$ transition at 2.54 μm, with a branching ratio of 96% and a natural linewidth of $\Gamma = 2\pi \times 3.1$ kHz. Doppler cooling on this transition was estimated to take ~300 s to reach the millikelvin range when starting from 10 K [14]. Another interesting scheme was discussed in [4] for a low-density plasma, using a magnetic-field gradient in a Penning trap in order to implement a Zeeman-shift-based Sisyphus cooling cycle. Comparing this method with our proposed scheme, the magnetic version has the benefit of a higher energy being removed per photon, leading to fast cooling rates in the millisecond range and thereby a lower sensitivity to environmental heating. Despite that, the magnetic inhomogeneity can lead to particle trapping due to the magnetic mirror effect, which is more pronounced for high-density plasmas and high-magnetic-field gradients. This can lead to ions being removed from the cooling cycle and makes a careful analysis necessary in that regime [15,16]. Using a strong laser to shift the energy levels as proposed in this work has the benefit of being all optical and independent of the trapping dynamics. Besides avoiding the complexity of a magnetic mirror, it is also a solution for experimental circumstances where a magnetic-field gradient cannot be implemented.

An extensive theoretical discussion of the ac Stark shift and dipole forces can be found in [17,18]. The proposed cooling scheme is illustrated in Fig. 1(b) using the same parameters as in the actual simulation as described below.

*julian.valentin.fesel@cern.ch

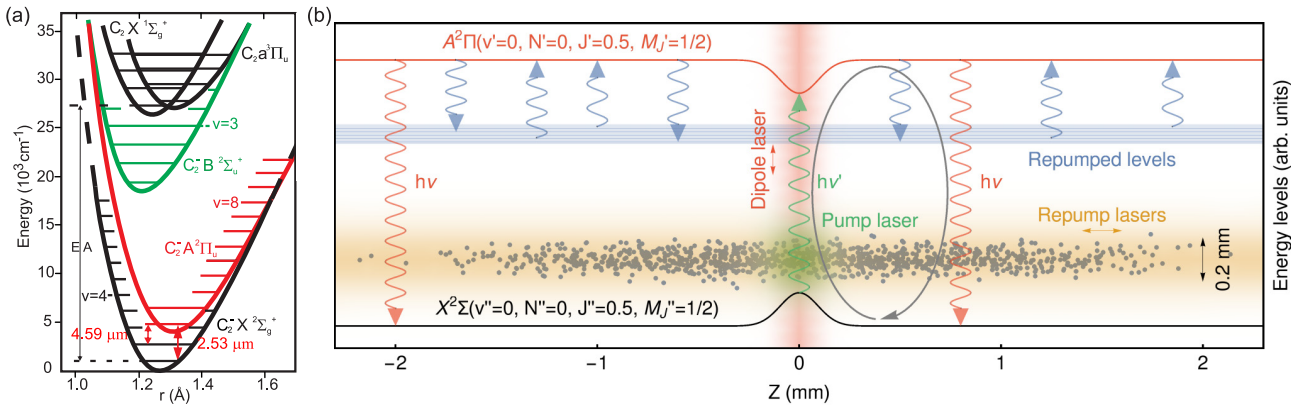

FIG. 1. (a) Overview of the electronic and vibrational states. The relevant transitions from the $A\,^2\Pi$ state for our cooling scheme are indicated. The electron affinity is equal to 3.27 eV [9]. (b) Sketch of the Sisyphus cooling cycle to scale with simulation parameters. The geometry of the ion cloud (gray) is shown together with laser beam profiles (red, green, and yellow) and an overlay of the involved electronic levels (see also Fig. 2). A 6-W laser (red), detuned from the resonance of the $A\,^2\Pi(v'=0,N'=1,J'=0.5,M'_J=1/2) \leftrightarrow X\,^2\Sigma(v''=0,N''=0,J''=0.5,M''_J=1/2)$ transition by $\delta = 1$ GHz and with a waist of $w_{\rm dip} = 185\ \mu$m, shifts the levels locally around $z = 0$, thereby creating a potential $U_{\rm dip} = 12.4$ mK. A second laser (green) on resonance with the maximally shifted levels causes transitions to the upper state in particles in the maximum of the dipole potential, by absorbing a photon with energy $h\nu'$. Due to the long lifetime of 50 μs of the $A\,^2\Pi(v=0)$ state in relation to their thermal energy, the particles are likely to leave the region of the shift and then decay to the initial state by emitting a photon with energy $h\nu = h\nu' + U_{\rm dip}$. Repump lasers (orange) on all other levels prevent losses from the cooling cycle by particles decaying to dark states. The whole cycle effectively removes the energy $\Delta E = h(\nu - \nu')$ from the particles.

Aside from repumpers, it is based on two lasers that address the $A\,^2\Pi(v'=0,N'=1,J'=0.5,M'_J=1/2) \leftrightarrow X\,^2\Sigma(v''=0,N''=0,J''=0.5,M''_J=1/2)$ transition of C_2^-. One is high powered in the range of several watts and blue detuned from resonance by 1 GHz [which we will refer to as a dipole laser (DL)], thereby shifting the energetic levels. A second laser is tuned to be resonant with the shifted levels [referred to as a pumping laser (PL)] and overlapped with the DL and the molecules. The scheme could also be realized with a single broad and strong laser, used for shifting and pumping at the same time, but in this work we use two separate lasers to permit greater flexibility. If only a single laser is used for pumping and shifting, Doppler heating by the blue-detuned DL has to be taken into account.

Focusing the lasers to a narrow region along the axis of the trap then creates an area where particles are pumped to the excited state $A\,^2\Pi(v'=0)$. If the lifetime of this state is long enough, a large fraction of particles stay in the excited state until they have left the region of the lasers and spontaneously decay to one of the lower states. In order to close the cooling cycle the lower levels, with the exception of $X\,^2\Sigma(v''=0,N''=0,J''=0.5,M''_J=1/2)$, are continuously repumped to the excited state by lasers applied in the axial direction, eventually resulting in a spontaneous decay to this ground state via the emission of a photon at frequency ν. The particles stay in this state until they reenter the shifting region. The whole cycle effectively removes the energy $\Delta E = h(\nu - \nu')$ from the particles. The energy difference stems from the axial kinetic energy of the particles and is removed when entering and leaving the shifting region due to the dipole force exerted by the laser.

Our simulation is based on the SIMBUCA code [19,20], which was specifically developed for the simulation of particles in a Penning trap. It uses a GPU to parallelize the calculation of the Coulomb interaction, allowing one to increase the total number of particles in comparison with a CPU-based simulation. The trajectories of the particles in the trap, including the cyclotron motion, are fully resolved using a fifth-order Dormand-Prince integrator. In order to include the interaction of the molecules with the light fields, we extended the code to include a simulation of the laser-induced electronic population transfers, which we based on rate equations and the Monte Carlo method. This approach is well justified in the regime of lasers with a spectral distribution much broader than the natural linewidth [21,22]. Our code treats the populations Π_i of all 16 levels (see Fig. 2, details described later in the text) separately according to the equations

$$\dot{\Pi}_i = \Sigma_j[\gamma_{ij}(\mathbf{x})(\Pi_j - \Pi_i) + \Gamma_{ji}\Pi_j - \Gamma_{ij}\Pi_i],$$
$$\gamma_{ij}(\mathbf{x}) = \frac{\Gamma_{ij}c^2}{16\pi^2 h\tau_{\rm A}\nu_{ij}^3}\rho_{ij}(\nu_{ij})I_{ij}(\mathbf{x}), \qquad (1)$$

with ρ_{ij} and I_{ij} being the spectral intensity distribution of the lasers addressing the transition, Γ_{ij} the respective Einstein coefficient, and $\tau_{\rm A}$ the lifetime of the excited state. The dipole force in the case of negligible scattering by the DL is given by

$$\mathbf{F}_i(\mathbf{x}) = -\Sigma_j\frac{\hbar\delta_{ij}}{2}\nabla\ln\left(1+\frac{\omega_{ij}^2(\mathbf{x})}{2\delta_{ij}^2}\right),$$
$$\omega_{ij}^2(\mathbf{x}) = \frac{3c^2\Gamma_{ij}}{2\pi h\nu_{ij}^3}I_{ij}(\mathbf{x}), \qquad (2)$$

with ω_{ij} being the Rabi frequency.

For the simulation an ion cloud of 1024 C_2^- molecules was initialized in thermal equilibrium at $T_{\rm init} = 10$ K, with a density of $n_{\rm init} = 2\times10^{13}$ m^{-3} and a confining magnetic field of $B = 5$ T in the Penning trap. The dimensions of the ion cloud are visualized in Fig. 3 with a mean radius of $\langle r\rangle = 50\ \mu$m and mean absolute axial extent of $\langle|z|\rangle =$

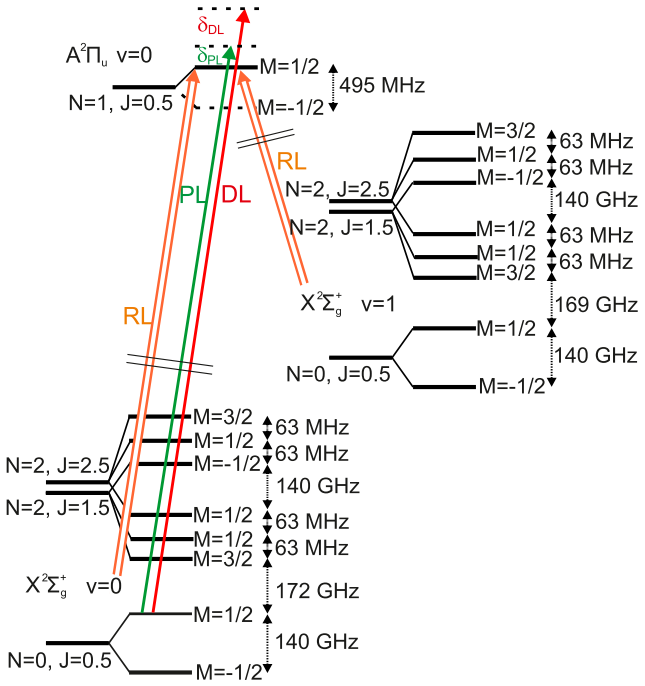

FIG. 2. Detail of the $A\,^2\Pi(v'=0) \leftrightarrow X\,^2\Sigma(v''=0)$ transition and the intermediate $X\,^2\Sigma(v=1)$ states in a 5-T magnetic field. Several arrows indicate the transitions that are addressed by the different lasers described in the text.

0.7 mm. These parameters can be experimentally achieved by supersonic expansion with subsequent dielectric barrier discharge of acetylene gas in a neon carrier [12,23,24]. We expect this to produce internally cold C_2^- with evenly distributed kinetic energies in the sub-eV range [25]. After mass selection in the 10-eV range the anions can be trapped and sympathetically cooled by electrons. Assuming a cryogenic 5-T Penning trap at 10 K, temperatures around 100 K can be achieved in a few seconds [26]. Subsequent evaporative cooling allows for a preparation of the anions at 10 K [27].

The laser parameters were chosen in order to correspond to values that could be realistically achieved with existing technology. For the DL we used a power of $P_{\mathrm{DL}} = 3$ W along the radial X axis, focused to a waist of $w_{\mathrm{dip}} = 185\ \mu$m in the center of the ion cloud. In our simulation we compared two different settings for the DL, once as a free Gaussian beam and once modulated by a cosine squared of the right periodicity, so as to correspond to, e.g., the light in an enhancement cavity. The detuning from resonance was set to $\delta_{\mathrm{DL}} = 1$ GHz. In order for Eq. (2) to be valid, scattering by the DL needs to be negligible, which implies that the spectral width of the DL must be much smaller than δ_{DL}. For the chosen parameters and molecules at 50 mK, we estimated the scattering by the DL to be less than a single photon per pass through the laser. Since the DL is blue detuned, each scattered photon results in a Doppler heating of 62 nK. Given that these scattering events still contribute to the dipole cooling cycle and a dipole force potential of $U_{\mathrm{dip}} = 6.6$ mK, we neglected this effect in the simulation.

The PL was modeled as two counterpropagating free beams along the radial Y axis with $P_{\mathrm{PL}} = 4$ mW, focused to the same size as the DL in the center of the ion cloud while neglecting the standing-wave pattern (SWP). The spectral width was set to $\Delta_{\mathrm{PL}} = 120$ MHz FWHM with a detuning that corresponds to the level shift in the focus of the DL of $\delta_{\mathrm{PL}} = 137$ MHz. On resonance, a pumping rate of $\gamma = 10$ MHz is reached in the focus of the laser. The repumping lasers along the trap axis were set to be on resonance with a power of 2 mW, the same waist as the other two lasers and a spectral width of $\Delta_{\mathrm{P}} = 50$ MHz. Depending on the transitions, the resulting pumping rate varies between $\gamma = 200$ kHz and $\gamma = 2$ MHz in the focus of the lasers. The widths of the PL and repumpers need to be large enough in order to sufficiently address the ion cloud, taking into account Doppler broadening and the spacial spectral shift in the center of the DL. Closing the cooling cycle requires repumping of 15 levels (see Fig. 2), which is implemented in the simulation with separate light fields. Three are needed to cover the unused $X\,^2\Sigma(v''=(0,1),N''=0,J''=0.5,M_J''=\pm 1/2)$ levels and the remaining ones distributed onto the $X\,^2\Sigma[v''=(0,1),N''=2,J''=(1.5,2.5),M_J''=(\pm 1/2,\pm 3/2)]$ states. In an experimental realization this could be done using three lasers. A single one is scanned over the $X\,^2\Sigma(v''=1)$ states, which is sufficient due to the low branching ratio of 4%. By imprinting sidebands at 63 MHz a second laser can repump the $X\,^2\Sigma(v''=0,N''=2)$ levels by scanning between the two branches of $X\,^2\Sigma[v''=(0,1),N''=2,J''=(1.5,2.5)]$, leaving an additional laser for the strong transition from $X\,^2\Sigma(v''=0,N''=0,J''=0.5,M_J''=-1/2)$.

The interesting cooling dynamics happen on a time scale of 14 s, which leads to impractically long simulation times. In order to circumvent this problem, we introduce an artificial augmentation factor f_{sc} to scale the size of the dipole force acting on the particles, which is initially set to 10 and consecutively reduced to unity at $[t(\mathrm{ms}), f_{\mathrm{sc}}] = [(0,10),(600,2),(925,1)]$ for the case without and at $[t(\mathrm{ms}), f_{\mathrm{sc}}] = [(0,10),(800,2),(2750,1)]$ for the case including the SWP. This effectively increases the dipole force potential, while leaving the pumping rates and the detuning the same. The reduction is necessary, since an artificially large force will start to prevent particles from reaching the intensity maximum of the DL, thereby removing them from the cooling, when its potential amplitude becomes comparable to the particle thermal energy. During our simulation the ratio of the thermal energy to the scaled dipole force potential was always larger than 10. Since the remaining small influence on the cooling speed is detrimental, the simulation still gives an upper bound on the efficiency. The actual computation simulates the trap dynamics during 8.8 s without and 5.5 s with a SWP.

Figure 3 shows the simulated temperature evolution. The time axis was scaled by the amplification factor f_{sc} to show the cooling time under realistic conditions. The resulting smooth behavior of the temperature is a powerful indication that the scaling factor is well justified and does not introduce any significant nonlinear effects. Two solid lines indicate the initial linear cooling behavior and the deviation from it as the ions get colder. For the axial degree of freedom this can be explained with the decrease in velocity in relation to the lifetime τ_{A} of the

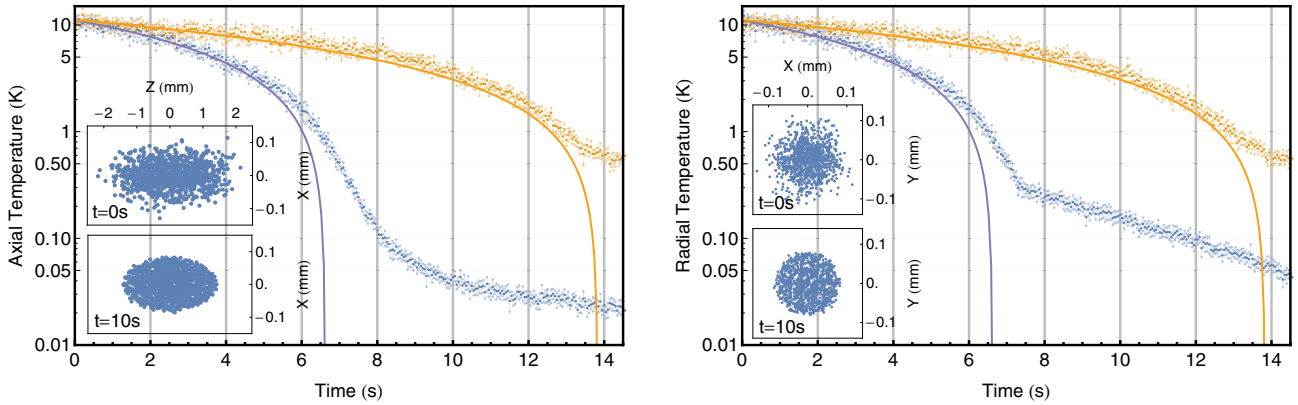

FIG. 3. Plasma temperature plot of 1024 C_2^- molecules subjected to dipole force cooling, once without (blue lower symbols) and once including a SWP (yellow upper symbols). The temperature is derived by fitting a Boltzmann distribution to the velocity histogram of the axial and radial degrees of freedom in cylindrical coordinates. The two solid lines show linear fits to the initial temperature evolution in order to illustrate the deviation from linear behavior as the molecules get colder. The insets show projected snapshots of the plasma taken from the simulation without a SWP at two points in time.

upper state. This gradually reduces the probability for a decay outside the shifted region and thereby the efficiency of the cooling. At a temperature of $T_w \simeq 60$ mK the mean traveled distance during the time τ_A becomes comparable to the waist of the DL. Together with the depth of the dipole force potential, this poses a practical limit to the cooling without readjustment of the laser parameters. The different cooling performance for the two cases with and without the SWP can be attributed to two factors. The first is a simple geometric advantage of the case without the SWP, since the overlap of the resonant region with the anion cloud is smaller. The second factor is an additional heating source that is caused by the SWP. Applying the dipole force potential in the Penning trap effectively causes a small inhomogeneity in the radially symmetric potential of the Penning trap. This causes a small expansion of the ion cloud and radial heating, which is more pronounced in the case with the SWP and stops the cooling at around 500 mK. For the case without the SWP the nonlinear effects in the radial temperature and the deviation from the evolution of the axial pendant can be attributed to a reduced thermalization between the axial and radial degrees of freedom starting in the weakly coupled regime at lower temperatures. The plasma in our simulation is initialized in the weak-coupling regime at $\Gamma_c = \frac{1}{4\pi\epsilon_0}\frac{e^2}{kT}(\frac{4\pi n}{3})^{1/3} \ll 1$ [28]. At around $T \simeq 0.5$ K it reaches the weakly coupled regime $\Gamma_c \simeq 1$ and is strongly coupled ($\Gamma_c \gg 1$) towards the end of the simulation. As discussed in [29,30], the equipartition decreases exponentially in the weakly coupled regime for a strongly magnetized plasma $\frac{\Omega_c b}{\bar{v}} \gg 1$. Apart from exhibiting interesting plasma dynamics, this shows that there is no significant direct cooling of the radial degrees of freedom.

An important concern for a cooling scheme working on a time scale of 14 s is heating by the environment. For a room temperature setup and at a pressure of around $\sim 10^{-9}$ Pa, this was experimentally investigated in [30,31], where it was concluded that the dominant contribution to heating stems from collisions of the trapped ions with residual gases. A heating rate of around ~ 0.1 K s^{-1} was measured, which would have a significant influence on the cooling speed and the final temperature of the described scheme. By going to a cryogenic Penning trap in the region of 10 K, where pressure down to $\sim 10^{-14}$ Pa [32] is achieved, the heating rate can be much lower with a reported value of 5×10^{-6} K s^{-1} [33]. In the presented simulation we assumed a cryogenic environment and neglected heating effects.

An interesting application of laser-cooled anions would be as a sympathetic coolant for other negatively charged species. Since Penning traps can be used to store species with widely differing masses together, they are well suited for this task. We investigated the efficiency of sympathetic cooling for a broad mass range with C_2^- as a coolant. For this we initialized the same ion cloud as for the previous laser cooling simulation, with 20% of the particles being replaced by anions of a different mass m' that are not directly addressed by the cooling. In order to speed up the simulation, the original full treatment of the laser cooling is approximated by an artificial drag force that resembles the actual cooling dynamics and is given by $F_z = -\mathrm{sgn}(v_z)U_0 \exp(-2z^2/w^2)$. The parameters are chosen so as to allow a simulation of particles with a mass corresponding to antiprotons. Figure 4 shows the results of the sympathetic cooling of different masses m' ranging from 1 to 50 nucleon. Even for an enhanced cooling during 100 ms, the sympathetic cooling of the axial degree of freedom is sufficiently fast. As for the previous simulation, a reduction in the equipartition of the radial degrees can be seen at lower temperatures. On the time scale of an actual implementation of the dipole cooling scheme, which is two orders of magnitude larger, the equipartition can be expected to reach lower temperatures.

In summary, we have presented an all-optical cooling scheme that is suitable for a variety of ion traps. Our simulation of the specific case of C_2^- in a Penning trap, which is a promising candidate for sympathetic cooling of other anions, shows a reduction in cooling time by an order of magnitude in comparison with Doppler cooling. On a time scale of 10 s the anions reach a temperature of 50 mK in the directly cooled axial and 150 mK in the indirectly cooled radial degrees of freedom. Similar improvements should be achievable for

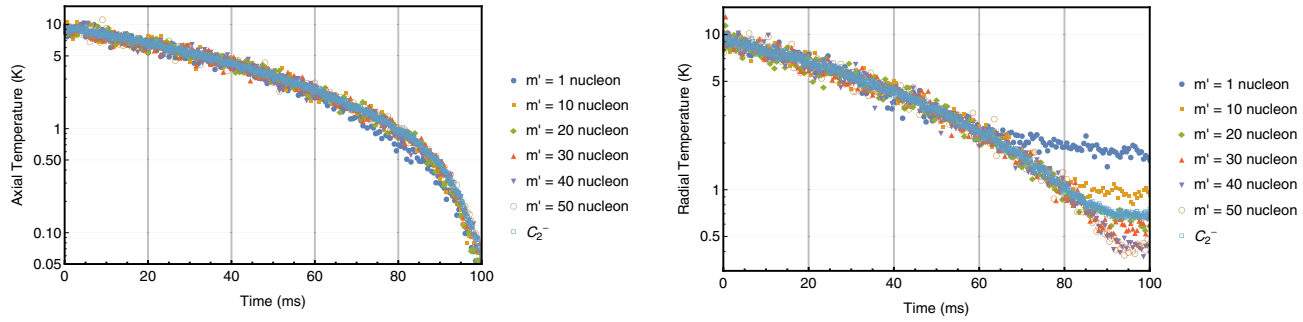

FIG. 4. Results of the sympathetic cooling of 200 negatively charged species with a mass m' immersed in an ion cloud of 824 C_2^-. For reference, the temperature of the C_2^- is given from the simulation involving the largest mass with $m' = 50$ nucleon. The cooling of the C_2^- was implemented using an artificial drag force that resembles a dipole cooling scheme.

other ions exhibiting narrow cooling transitions. Furthermore, we investigated the efficiency of sympathetic cooling by laser-cooled C_2^-. A mass range of 1–50 nucleon was covered, which includes light anions like antiprotons and heavier anions relevant in ultracold chemistry. Another promising application of the described scheme could be in the production of ultracold electrons. A transition to a cryocooled Penning trap at $T = 1$ K and with a magnetic field of $B = 0.5$ T would reduce heating by synchrotron radiation [34] below the axial cooling rate found in this work. Together with an increased equipartition rate at lower magnetic fields [30], this could potentially allow one to decrease the particle mass range where this cooling scheme is applicable down to the regime of electrons.

We want to thank our summer student Cui Hao for his help with writing the code. The research leading to these results received funding from the European Research Council under Grant Agreement No. 277762 COLDNANO.

[1] T. P. Snow and V. M. Bierbaum, Annu. Rev. Anal. Chem. **1**, 229 (2008).
[2] O. Dulieu and C. Gabbanini, Rep. Prog. Phys. **72**, 086401 (2009).
[3] A. Kellerbauer and J. Walz, New J. Phys. **8**, 45 (2006).
[4] P. Yzombard, M. Hamamda, S. Gerber, M. Doser, and D. Comparat, Phys. Rev. Lett. **114**, 213001 (2015).
[5] A. Kellerbauer, A. Fischer, and U. Warring, Phys. Rev. A **89**, 043430 (2014).
[6] E. Jordan, G. Cerchiari, S. Fritzsche, and A. Kellerbauer, Phys. Rev. Lett. **115**, 113001 (2015).
[7] L. Pan and D. R. Beck, Phys. Rev. A **82**, 014501 (2010).
[8] V. V. Ivanov and S. Gupta, Phys. Rev. A **84**, 063417 (2011).
[9] M. K. Ervin and W. C. Lineberger, J. Phys. Chem. **95**, 1167 (1991).
[10] P. Rosmus and H.-J. Werner, J. Chem. Phys. **80**, 5085 (1984).
[11] T. Sedivcová and V. Spirko, Mol. Phys. **104**, 1999 (2006).
[12] P. L. Jones, R. D. Mead, B. E. Kohler, S. D. Rosner, and W. C. Lineberger, J. Chem. Phys. **73**, 4419 (1980).
[13] Y. Shan-Shan, Chin. Phys. **12**, 745 (2003).
[14] S. Gerber, J. Fesel, M. Doser, D. Comparat (unpublished).
[15] J. Fajans, Phys. Plasmas **10**, 1209 (2003).
[16] K. Gomberoff, J. Fajans, J. Wurtele, A. Friedman, D. P. Grote, R. H. Cohen, and J. L. Vay, Phys. Plasmas **14**, 052107 (2007).
[17] J. Dalibard and C. Cohen-Tannoudji, J. Opt. Soc. Am. B **2**, 1707 (1985).
[18] R. Grimm, M. Weidemüller, and Y. Ovchinnikov, Adv. At. Mol. Opt. Phys. **42**, 95 (2000).
[19] S. Van Gorp, M. Beck, M. Breitenfeldt, V. De Leebeeck, P. Friedag, A. Herlert, T. Iitaka, J. Mader, V. Kozlov, S. Roccia, G. Soti, M. Tandecki, E. Traykov, F. Wauters, C. Weinheimer, D. Zákoucký, and N. Severijns, Nucl. Instrum. Methods Phys. Res. Sect. A **638**, 192 (2011).
[20] S. Van Gorp and P. Dupre, in *Non-Neutral Plasma Physics VIII: 10th International Workshop on Non-Neutral Plasmas*, edited by X. Sarasola, L. Schweikhard, and T. S. Pedersen, AIP Conf. Proc. No. 1521 (AIP, New York, 2013), pp. 300–308.
[21] R. Höppner, E. Roldán, and G. J. de Valcárcel, Am. J. Phys. **80**, 882 (2012).
[22] D. Comparat, Phys. Rev. A **89**, 043410 (2014).
[23] U. Even, EPJ Tech. Instrum. **2**, 17 (2015).
[24] H. Hotop, T. A. Patterson, and W. C. Lineberger, Phys. Rev. A **8**, 762 (1973).
[25] U. Even (private communication).
[26] S. L. Rolston and G. Gabrielse, Hyperfine Interact. **44**, 233 (1988).
[27] G. B. Andresen *et al.*, Phys. Rev. Lett. **105**, 013003 (2010).
[28] D. H. E. Dubin and T. M. O'Neil, Rev. Mod. Phys. **71**, 87 (1999).
[29] D. H. E. Dubin, Phys. Rev. Lett. **94**, 025002 (2005).
[30] M. J. Jensen, T. Hasegawa, J. J. Bollinger, and D. H. E. Dubin, Phys. Rev. Lett. **94**, 025001 (2005).
[31] M. J. Jensen, T. Hasegawa, and J. J. Bollinger, Phys. Rev. A **70**, 033401 (2004).
[32] A. Mooser, S. Ulmer, K. Blaum, K. Franke, H. Kracke, C. Leiteritz, W. Quint, C. C. Rodegheri, C. Smorra, and J. Walz, Nature (London) **509**, 596 (2014).
[33] G. B. Andresen *et al.*, Nat. Phys. **7**, 558 (2011).
[34] J. Bernard, J. Alonso, T. Beier, M. Block, S. Djekić, H.-J. Kluge, C. Kozhuharov, W. Quint, S. Stahl, T. Valenzuela, J. Verdú, M. Vogel, and G. Werth, Nucl. Instrum. Methods Phys. Res. Sect. A **532**, 224 (2004).

2.6. Discussion and summary of the results obtained in the simulations

Comparing the different laser cooling schemes presented in the previous sections, it is hard to single out an optimal one. Choosing a scheme for experimental realisation in a Penning trap, comprises a tradeoff between different requirements and options. Amongst other things, one has to take into account the trapping geometry and the optical access, the shape of the magnetic field allowed by the experimental setup, as well as the available budget for the laser system. The aim of this section is to summarise the results on laser cooling C_2^-, obtained in the previous section and in the literature. First, the different implementations of laser cooling so far investigated will be summarised, highlighting their merits and drawbacks, thereby enabling a comparative discussion. Consecutively, the performance of sympathetic cooling in a Penning trap, as seen in the simulations, is summarised. The section ends with a discussion of the risk of antiproton annihilations when mixed together with C_2^- in a trap for cooling.

2.6.1. Summary of the results on different laser cooling methods

Doppler selective photodetachment cooling: As described in section 2.5.1, this scheme is the least demanding one concerning experimental realisation, since it does not require repumping. A single Doppler–selective laser at 2.5 µm excites the hot fraction of anions to the $A^2\Pi$ state, from where a second, high–intensity UV laser with a wavelength in the range of $379\,\text{nm} < \lambda_{\text{UV}} < 446\,\text{nm}$ and an intensity of $3.8 \times 10^8\,\text{W}\,\text{m}^{-2}$ (compare figure 2.1) is then photodetaching the excess electron and thereby removing the anion from the trap. This effectively implements an evaporative cooling scheme and was shown in the simulation to reduce the temperature of the anion cloud by a factor of ~ 5.5, at the cost of a particle loss of $\sim 70\,\%$ within $\sim 0.35\,\text{ms}$, starting at around 10 K. In a Penning trap, a significant fraction of the photodetached, hot electrons is retrapped.

An interesting result of the simulation is, that this leads to substantial sympathetic heating of the anions at longer timescales. For this reason, this cooling scheme is probably of limited use for applications in a Penning trap. It could though be interesting for a proof of principle cooling in a Paul trap, where the electrons will be ejected.

Doppler cooling on $X^2\Sigma(v'' = 0) \leftrightarrow B^2\Sigma(v' = 0)$: The use of this transition for Doppler laser cooling was investigated in (Yzombard et al., 2015) for the case of a Paul trap. The lifetime of the $B^2\Sigma(v' = 0)$ state is 75 ns and the wavelength for the transition to $X^2\Sigma(v'' = 0)$ at 541 nm. While there are in principle 12 lower vibrational levels that need to be repumped (compare figure 2.1), only the lower ones up to $v'' = 4$ were addressed in the simulation, leading to losses to dark states. Due to the additional rotational branching, this would still require more than 10 separate lasers in an experimental realisation. For this setting, cooling from 5 K

to 60 mK was achieved within 50 ms, with a final 25 % of anions in dark states. It has to be stressed that this simulation was done for particles in a Paul trap.

Using this scheme in a Penning trap would prove to be much more challenging. The strong magnetic fields present in this case result in Zeeman splitting, which requires additional repumping lasers for this already complex task. Furthermore, the 441 nm laser can photodetach the anions by two–photon absorption, thereby releasing hot electrons in the trap, possibly leading to sympathetic heating as for photodetachment cooling described above. For these reasons the use of this scheme in a Penning trap is rather limited.

Doppler cooling on $X^2\Sigma(v''=0) \leftrightarrow A^2\Pi(v'=0)$: A detailed description of this scheme can be found in section 2.5.1. Compared to Doppler cooling on the $X^2\Sigma(v''=0) \leftrightarrow B^2\Sigma(v'=0)$ transition, the lifetime of the $A^2\Pi(v'=0)$ state with 51 µs, as well as the transition wavelength of 2.54 µm is much longer, resulting in a weaker cooling force. Assuming repumping of the $X^2\Sigma(v''=0,1)$ states, and a spectral width of 1 MHz for the cooling laser, the simulation of a small plasma in a 1 T Penning trap showed cooling from 10 K down to $\sim$ 100 mK within $\sim$ 150 s. In comparison with Doppler cooling on the $X^2\Sigma(v''=0) \leftrightarrow B^2\Sigma(v'=0)$ transition, repumping is much less demanding. The decay channel to $X^2\Sigma(v''=1)$ with a branching ratio of $\sim$ 4 % can be covered by a single broad and free–running diode laser at 4.57 µm, which is commercially available. The main effort therefore lies in repumping the decay channel to $X^2\Sigma(v''=0)$. Given the equidistant splitting of some of the rotational sublevels in this branch, the number of lasers needed can be reduced by applying sidebands. Assuming this, the best estimate for the number of separate, experimentally required lasers is five, including the cooling laser.

An important concern for such a slow cooling is heating by the environment (e.g. trap misalignment and collisions with residual gas). In the cryogenic Penning traps normally used for antimatter experiments, heating rates of $5 \times 10^{-6}\,\mathrm{K\,s^{-1}}$ have been reported (Andresen et al., 2011), which is sufficiently low for this cooling. In addition, the cooling time can be reduced if it is experimentally possible to broaden the spectral width of the cooling and repumping lasers to around 10 MHz.

Sisyphus cooling using a magnetic field gradient: This strong cooling method was discussed in (Yzombard et al., 2015). It is based on a magnetic field gradient from 2 T to 0.2 T along a $\sim$ 15 mm plasma in a Penning trap. The Zeeman–effect then causes different shifts of the rotational levels and thereby exerts a force along the magnetic field gradient. By resonantly pumping specific levels of the $X^2\Sigma(v''=0) \leftrightarrow B^2\Sigma(v'=0)$ transitions on the high and low field side, a cooling cycle can be implemented, where the particle looses energy by constantly working against the mentioned force. While having repumping requirements equal to or better than Doppler cooling on $X^2\Sigma(v''=0) \leftrightarrow B^2\Sigma(v'=0)$, the cooling time is greatly reduced. In their simulation, the authors saw a reduction of the anion temperature from 70 K to the $\sim$ 1 K regime within 80 ms.

While this would constitute a formidable cooling method and reduces the requirement on the trap heating rates, it also has certain caveats. Depending on the setup, implementing a $\sim 1.8\,\mathrm{T}$ magnetic field gradient might conflict with other requirements of the experiment. In addition, the magnetic mirror effect together with the space charge of the anions can lead to complex plasma dynamics, which can be detrimental to the cooling and the overall experimental goal (Fajans, 2003; Gomberoff et al., 2007). Especially for high density plasmas an implementation therefore requires a careful analysis. An interesting application for this method could be a proof of principle cooling in a Paul trap with additional magnetic field gradient (Walz et al., 1995).

Sisyphus cooling using an optical dipole force: The work on this cooling method was motivated by the detrimental effect of the magnetic field gradient on the plasma dynamics in the Sisyphus cooling scheme discussed above. While the main principle for the reduction of the anion energy stays the same, the force exerted by the magnetic field gradient is replaced by the dipole force of a high intensity laser. A more detailed description can be found in section 2.5.2. In addition to the repumping requirements, which are comparable to the $X^2\Sigma(v'' = 0) \leftrightarrow A^2\Pi(v' = 0)$ Doppler cooling and the previous Sisyphus method, this scheme needs the generation of a $\sim 5.6 \times 10^7\,\mathrm{W\,m^{-2}}$ light field in the centre of the plasma. It is therefore the only cooling method discussed in this thesis, that necessitates a radial optical access in the trap.

An interesting result of the simulation is that an effective radial inhomogeneity, caused by the dipole laser in the trap, can lead to expansion and heating of the plasma, resulting in a reduced cooling speed. Optimally, the dipole force is exerted by a single laser beam with a waist much bigger than the plasma radius, so that the force is in first approximation only acting axially. In the simulation the waist of the dipole beam was nearly double the radius of the plasma, which resulted in cooling from 10 K down to 100 mK within 8 s. This method could therefore serve as a compromise between the slow, all–optical Doppler cooling and the fast but magnetic field gradient based Sisyphus cooling.

2.6.2. Sympathetic cooling performance

The term sympathetic cooling denotes the thermalisation of different species in a trap, of which one is often actively or passively cooled. This technique is a standard procedure for many of the antimatter experiments at CERN, which use passively cooled electrons for sympathetic cooling of antiprotons via the Coulomb interaction in a Penning trap. Using an actively cooled heavy anion for the same task is a novel approach, and was investigated in the simulations discussed in the previous sections.

In 2.5.1 a plasma of 2048 particles, among which 200 were antiprotons, was simulated under the influence of an axial drag force cooling on the 1848 C_2^- anions. Starting from 10 K, the temperature of the axial degree of freedom was reduced below 10 mK within 20 ms. The axial temperature of the sympathetically cooled antiprotons follows this

development closely until the 10 mK mark. Given that 100 mK would be sufficient for precision measurements with antiprotons, this would be a spectacular result, if achieved experimentally. The weakness of this simulation is the small size of the plasma, which can significantly alter the dynamics with respect to centrifugal separation.

For this reason, the simulation was repeated for similar settings, but with the difference of an augmented Coulomb repulsion. This leads to an approximation of the space charge found in a larger plasma, if the density is scaled accordingly. In this setting, the simulation showed a pronounced centrifugal separation, a weaker thermalisation rate and a decoupling of the temperature evolution at $\sim 3\,\mathrm{K}$. Despite that, the antiprotons still reach sub–Kelvin temperatures within 30 ms. As discussed in 2.6.1, the active cooling schemes work on timescales of tens of seconds, around two orders of magnitude longer than the sympathetic cooling. Even though simulations on this timescale are practically not feasible, the result found on the short scale would result in sufficiently fast cooling, if extrapolated to the actual cooling time.

In addition to this simulation, the thermalisation of the axial and radial degrees of freedom in a small plasma were investigated in 2.5.2, for the case of a cooling that only addresses the axial degree directly. This simulation was repeated with different masses, covering the range of 1 u to 50 u for the sympathetically cooled species. The simulated plasma consisted of 824 directly cooled C_2^- and 200 thermalising particles. The sympathetic cooling of the axial degree of freedom on a timescale of 100 ms shows a similar behaviour as in 2.5.1, with no significant temperature difference between the two species, and is found to be mass–independent.

Cooling of the radial degree of freedom shows a different behaviour. The equipartition between the radial and axial degrees of freedom diminishes strongly at lower temperatures. This effect is found to be more pronounced for lower masses. Despite that, the equipartition is shown to be still strong enough to reach radial temperatures below 100 mK within 9 s.

2.6.3. Risk of annihilations for antiproton sympathetic cooling with matter anions

Loading baryonic matter and antimatter into the same Penning trap raises the question of annihilations between the species. In contrast to nuclear fusion, where large energies are needed to overcome the Coulomb repulsion between the positively charged cores, the cores of matter and antimatter atoms have opposite charges and attract each other. This section presents an argument on the basis of the energetic orders of magnitude involved, that for the application of sympathetic antiproton cooling, annihilations are of no concern.

If C_2^- and antiprotons are loaded in the same trap, the only barrier between the cores is the shielding of the positive C_2^- core by the electron cloud and the repulsion of the negatively charged antiproton by the excess electron. To overcome this barrier, the antiprotons would either need to approach the molecules to a distance of $\sim 1\,\mathrm{\AA}$, in order to reach into the electron cloud, or would need an energy larger than the electron affinity $\mathrm{EA} = 3.27\,\mathrm{eV}$, in order to be able to neutralise the anion by collision. Even

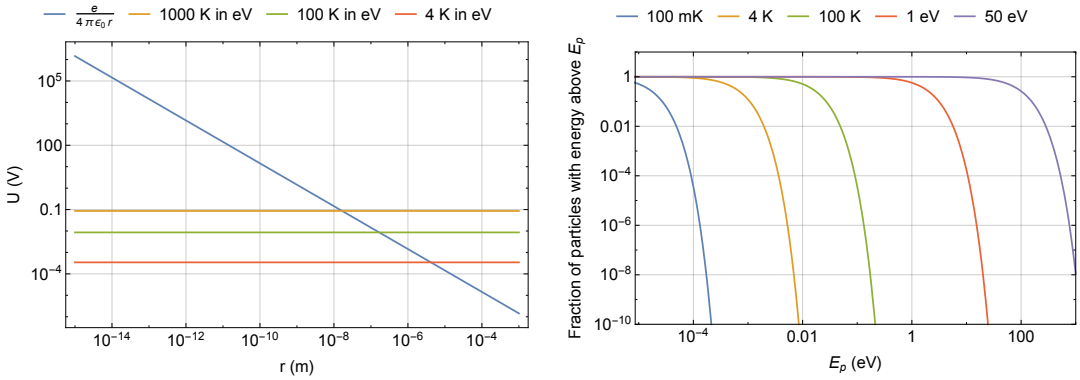

Figure 2.5.: *Left:* Potential energy of a single charge. *Right:* Plot of the fraction of particles of a Boltzmann distribution, reaching an energy above E_p.

though the neutralisation does not necessarily pose the risk of annihilation, since the neutral molecule can escape the trap, both possibilities are discussed.

The Brillouin limit (2.59) of an antiproton plasma in a 5 T Penning trap is around $\sim 7 \times 10^{10}\,\mathrm{cm}^{-3}$. This corresponds to a Wigner-Seitz radius of $a_\mathrm{WS} \sim 1.5\,\mu\mathrm{m}$. The left hand side of figure 2.5 shows the electric potential of a single charge. As can be seen, starting from a_WS, the antiprotons would have to overcome a potential energy of tens of eV in order to approach the core to ~ 1 Å. Given that this is already larger than the electron affinity of $C_2{}^-$, this argument can be used to derive an upper bound on the annihilation rate. Assuming a Boltzmann distribution of antiproton kinetic energies, the risk of annihilation can be estimated by calculating the fraction of particles with an energy above EA for different plasma temperatures.

The result of this calculation is shown on the right hand side of figure 2.5. As can be seen, the fraction of antiprotons with a kinetic energy above the threshold are negligibly small for the cryogenic plasmas usually used in the antiproton experiments at CERN. In addition, the plasma temperatures that would be needed would not only pose the risk of substantial annihilation, but would also be impossible as a starting temperature for most of the cooling schemes discussed in this thesis.

3. Experimental setup for a pulsed C_2^- source

As was seen in the previous chapter, the slow laser cooling schemes necessitate to initialise trapped C_2^- at around 10 K. Starting from hot anions with kinetic energies in the $\sim$ eV range, the 100 K regime can be reached within 100 s, using electron cooling in a 5 T cryogenic Penning trap, at liquid He temperature (Rolston and Gabrielse, 1989). From there, 10 K are reachable by evaporative cooling (Andresen et al., 2010). Apart from this, the anion has to be produced in large enough quantities. The AE$\bar{g}$IS experiment at CERN traps around $\sim 2 \times 10^5$ antiprotons within two AD cycles of $\sim$ 200 s each (Aghion et al., 2018; Brusa et al., 2017). In order to be in agreement with the antiproton to coolant ratios in section 2.5, the anions therefore have to be produced at a rate of $\sim 1 \times 10^4\,\mathrm{s}^{-1}$, assuming that they can be accumulated without loss.

An additional requirement that was implicitly assumed so far is, that the anions can be initialised in their internal ground state, that is the $X^2\Sigma(v'' = 0)$ manifold. This is important, since in the homonuclear case of C_2^-, where ro–vib transitions are forbidden, any higher excitations cannot spontaneously decay to the ground state, and are therefore lost from the cooling cycle. Internally hot C_2^- has been produced using graphite filaments, heated to 2600 K by an ac current (Honig, 1954), hot cathode dc discharges in an equal gas mixture of carbon monoxide (CO) and acetylene (C_2H_2) (Jones et al., 1980; Lineberger and Patterson, 1972; Mead et al., 1985) and ac discharges in water cooled gas cells, using a mixture of helium and acetylene (K. M. Ervin et al., 1989; M. K. Ervin and Lineberger, 1991; Rehfuss et al., 1988; Royen and Zackrisson, 1992; Shan-Shan et al., 2003; Wang et al., 1999). Using these methods would therefore require additional optical pumping, or cold neutral buffer gas cooling for ground state preparation. Given the complexity of pumping schemes in molecular species, neutral buffer gas cooling is favourable.

Anion production including buffer gas cooling is effectively implemented in a so–called supersonic expansion valve (SSEV). Here, the anions are produced from a specific trace gas, mixed in an usually noble carrier gas. Pulses of the gas are then expanded from several atmospheres to vacuum, while being subjected to an ionisation mechanism. Since the gas cools rapidly during the expansion, the collisions of the produced anions with the neutral carrier leave them internally cold. For the ionisation, high energy electron beams (Johnson et al., 1984), electric discharges (Osborn et al., 1996) and dielectric barrier discharges (Luria et al., 2009) have been used. On the basis of this the successful production of C_2^- has been reported. In (Beer et al., 1995) a mixture of 5 % C_2H_2 and 3 % CO_2 in helium was expanded through a pulsed electric discharge. The internal rotational temperature was determined to be $\approx$ 80 K and no signs of vibrational excitation

were found. Similarly, in (Bragg et al., 2003) a mixture of 2 % C_2H_2 and 2 % CO_2 in neon was used, while the electric discharge was stabilised by an 1 kV electron gun. The expected rotational temperature was quoted in the range of 50 K to 100 K. In (Lu et al., 2015), C_2^- production was reported from sputtering of the stainless steel electrode of an entrainment source.

Motivated by these results, this chapter describes a pulsed source for ground state C_2^-, using a commercial SSEV with an integrated dielectric barrier discharge (DBD) for ionisation (Even, 2015). Since the ionisation produces unwanted byproducts, the setup includes acceleration and mass filtration of the anion pulses, in order to prevent impurities in the final trapped anion clouds. The section starts with an overview of the apparatus and then proceeds with a detailed discussion of the different components. This includes the anion production, acceleration and steering of the pulses, mass filtration, anion detection and the timing and electronic control of the setup. In addition, the development of an enhancement cavity and the necessary optics for photodetachment spectroscopy is described. The section ends with a presentation and discussion of the experimental results.

3.1. Overview of the setup

An overview of the setup is depicted in figure 3.1. Starting from the upper left, a gas mixture of acetylene as a trace gas in a helium or neon carrier at around $\sim$ 8 bar is supplied to the SSEV, which together with the built–in DBD stage, gives out ionised pulses into the vacuum (see figure 3.2 c)). The DBD needs to be stabilised by supplying electrons, which is implemented using a biased halogen lamp from which the glass cover was removed (see figure 3.2 e)). Under pressure, the valve constantly leaks a small amount of the supplied gas in the vacuum. Even when employing strong pumping, the production region therefore has to be separated from the rest of the setup, which is done using a so–called skimmer. This is a conical and sharp aperture with a 3 mm diameter, designed to minimise the influence on the produced anion beam (see figure 3.2 a)). In the next chamber the anions are accelerated to 1.8 keV using a pulsed tube, which at the same time separates them from the positive and neutral species in the bunch. The high acceleration voltage is necessary to reduce the detrimental effects from the space charge potential of the resulting anion bunch and to make the beam more resilient to electromagnetic stray fields. Two segmented einzel lenses allow to collimate and steer the beam by applying different dc voltages to the electrodes (see figure 3.2 b)). A translatable Faraday cup (FC) serves as a first diagnostic tool for the anion beam (see figure 3.2 f)). At this point the accelerated beam still consists of different anionic species. It is therefore sent through a commercial Wien filter system, to spatially separate the C_2^- from the rest of the anions. After the Wien filter, a third segmented einzel lens allows for corrections to the beam, and a beam bender enables rerouteing the beam to a Paul trap. The latter is not discussed in this thesis. Finally, the anions are detected by either a FC and a current amplifier, or a multi channel plate (MCP) using a phosphor screen as anode and a fast, triggered camera system for imaging. The

electronic control of the experiment is done using LabView to centrally monitor and set the involved devices. A field–programmable gate array (FPGA) then executes the fast timing sequence and performs timed analogue to digital conversion.

3.1.1. Pulsed creation of C_2^-

The specific type of SSEV used in the experiment is a commercially available *Even–Lavie pulsed valve EL–5–3–2011* for room–temperature use, and includes a DBD module of the type *Even–Lavie DBD 12*. It is operated by a dedicated controller unit, which activates the SSEV and DBD in a timed sequence after receiving a TTL pulse. A detailed description of the working principle of the SSEV can be found in (Even, 2015) and a picture is shown in figure 3.2 c). Upon reception of the TTL signal, a magnetic coil in the SSEV is pulsed and pulls back a magnetic plunger, that separates the high pressure from the vacuum side. This releases a $\sim 20\,\mu s$ burst of gas into the vacuum, which expands and is formed into a beam by a conical nozzle. Around $\sim 100\,\mu s$ after the SSEV the DBD is activated. The latter is implemented by a ring–shaped electrode around the nozzle, which is isolated from the gas by a dielectric. A rapid succession of up to 30 high–voltage pulses at 750 kHz and up to 1500 V then accelerates electrons in the nozzle region, which are confined by the field of an additional ring–shaped permanent magnet. The current in the thereby created discharge is limited by the dielectric to short nanosecond spikes, which prevents the formation of an arc, heating of the gas jet and contamination by sputtering from the electrode. A detailed review of DBDs can be found in (Kogelschatz, 2003). The discharge needs to be stabilised by an electron supply. For this, a simple hot cathode in the vicinity of the nozzle is sufficient. In the setup, the latter is realised using a halogen light bulb *Osram Halogen Starlight, 90 W , 12 V*, from which the glass was broken off. During operation it is biased to $-200\,V$ and heated by a current of 3.5 A, which is done by floating a *TTI PL303QMD-P* power supply. The floating voltages are supplied by a *CAEN SY1527* system, using a *CAEN A1821N* board for the negative, and a *CAEN A1832P* for positive voltages. Different gas mixtures were tried out in the setup, which were based on different ratios of acetylene and carbon dioxide in either a helium or neon carrier. They are similar to previously used gas mixtures (see beginning of chapter 3). Given the safety concerns associated with acetylene (Schendler and Schulze, 1990), the gas mixtures were readily bought from *Carbagas* at 40 to 100 bar, depending on the mixture. A pressure regulator *Tescom series 44–1100* is used to adjust the supply to the valve from 0 bar to 100 bar with a precision of 0.5 bar.

The sealing of the magnetic plunger allows for a constant small leak of the gas into the vacuum, and therefore requires strong pumping in the production chamber. For this a $400\,L\,s^{-1}$ turbo pump is employed (*Oerlikon Leybold Turbovac TMP 361*), which is able to sustain 6×10^{-6} mbar at a supply pressure of 10 bar at the SSEV. While this is sufficient for the operation of the SSEV and DBD, the rest of the setup, and especially any employed particle traps, need a much better vacuum. For this reason, the production chamber is connected to the rest of the setup only by a small opening, and a second $240\,L\,s^{-1}$ turbo pump (*Edwards nEXT240D*) used in the next chamber. The

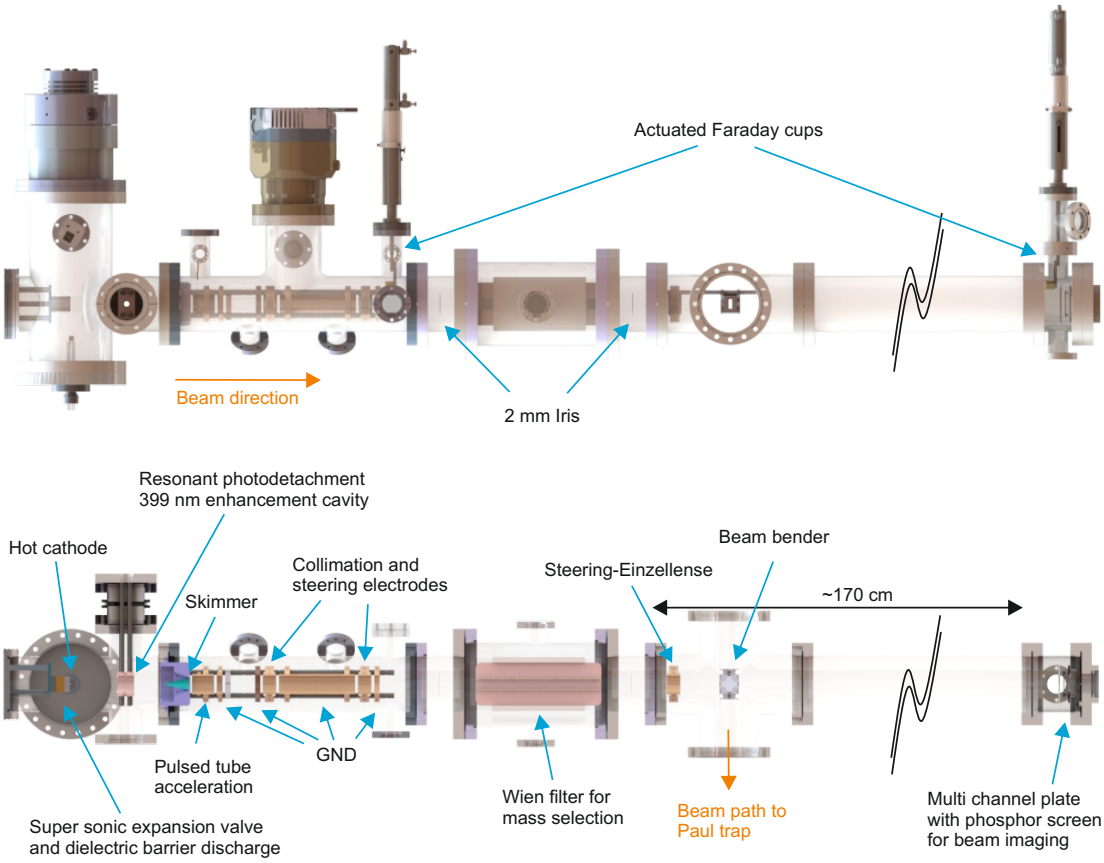

Figure 3.1.: *Top:* 3D CAD drawing of the setup described in this thesis. Only the main components are included and the FC is shown duplicated to indicate the possible mounting positions. The flight direction of the anions is from left to right. *Bottom:* Horizontal cut through the 3D drawing viewed from above, with descriptions of the important parts.

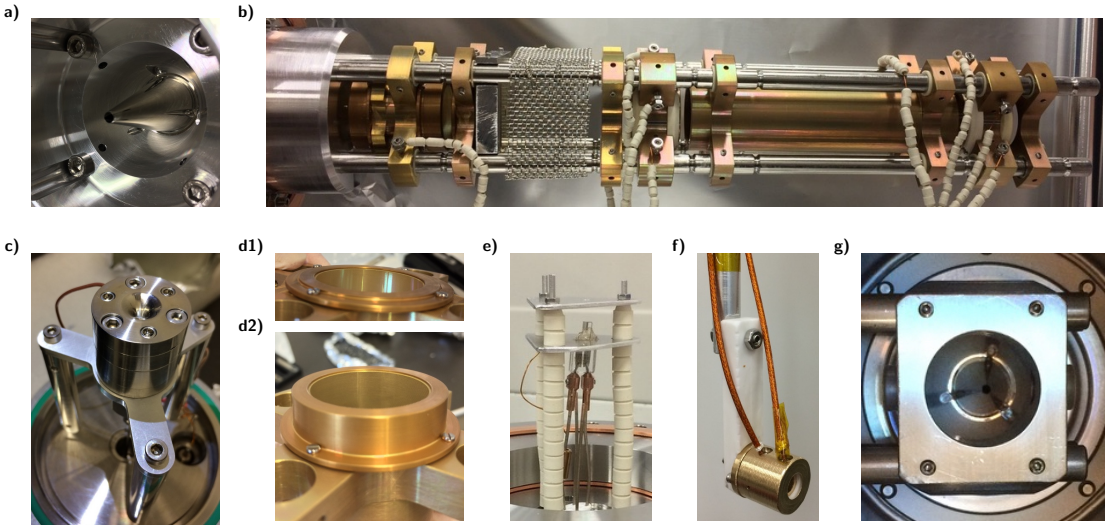

Figure 3.2.: **a)** 3 mm opening diameter skimmer. **b)** Electrode stack for acceleration, collimation and steering of the anion pulse. **c)** Even–Lavie type supersonic expansion valve with dielectric barrier discharge stage. **d1)** and **d2)** Gold mesh used for the endcaps of the pulsed tube and ground electrode. **e)** Self–built hot cathode using a broken halogen light bulb. **f)** Self–built shielded Faraday cup. **g)** Optical resonator mounted in front of the skimmer.

large on–axis particle densities produced by the SSEV can lead to significant interference at the entrance of a small aperture, up to an essential clogging. To prevent this (see (Even, 2015; Luria et al., 2011) for details) a skimmer with a 3 mm orifice is used (*Beam dynamics Inc., model 50.8 Ni*), that is mounted at a distance of 17.5 cm downstream from the SSEV.

3.1.2. Acceleration and collimation of the anion pulse

The cold gas jet leaving the SSEV has a velocity of $\sim 825\,\mathrm{m\,s^{-1}}$ (see section 3.2.1) in the case of neon and an axial velocity spread corresponding to a temperature of $\sim 200\,\mathrm{mK}$, according to the manufacturer. For several reasons it is preferable to accelerate the particles to higher energies at this stage. First, the experimental environment at the AD involves large magnetic stray fields, and makes it therefore difficult to work with low energy particles. Secondly, the acceleration allows to separate the negative from the likewise produced positive charges, and is necessary to reduce the effect of space charge expansion in the pure anion beam. Lastly, the larger energy increases the detection efficiency when using an MCP for monitoring the beam.

The acceleration is implemented using a so–called pulsed tube. This is an electrically conducting tube, with an inner diameter of 3 cm and a length of 4 cm, that is covered by a fine mesh at the entrance and exit (see figure 3.2 d)). The latter is a *Precision eforming, MG17* gold mesh, with an opening fraction of 90 %, a wire line width of 19 µm and an opening width of 344 µm. This tube is placed on axis directly after the skimmer. It is initially grounded, but upon entrance of the particle jet, ramped to $U_{\mathrm{acc}} = -1.8\,\mathrm{kV}$ using a fast push–pull switch (*Behlke HTS 31-03-GSM*). Due to the mesh on either side, the potential inside the tube is homogeneous and the particles experience no force until they reach the other end of the tube. Upon leaving, they are accelerated by a potential gradient towards a third mesh (see figure 3.2 d1)) which is grounded. For accelerations in the kV regime, the kinetic energy of the particles can therefore in good approximation be assumed to be U_{acc}. A 6 mm diameter, removable iris is placed behind the last mesh in order to define the size of the beam. In addition to clipping unwanted parts of the beam, which would be distorted by the einzel lens system, the imposed constraint helps in the analysis of the beam dynamics.

Figure 3.3 d) shows a simulation of the acceleration potential. After acceleration, two einzel lenses at positive voltages allow to change the focus of the beam. The voltage needed for collimation is on the order of half the acceleration voltage with opposite sign, as will be seen in section 3.2. In addition, the electrode stack allows steering of the beam. For this, the einzel lenses are segmented in four isolated parts. To set the voltages on each electrode, the following formula is used:

$$U_j = U_{\mathrm{el}} + U_{\mathrm{st}} \sin\left(\phi + \frac{\pi j}{4}\right). \tag{3.1}$$

Here, U_{el} is the offset for beam collimation, U_{st} the voltage determining the magnitude of the steering, ϕ the angle defining the direction of the steering and j the index defining the electrode, ranging from one to four. A simulation of the resulting potentials for three

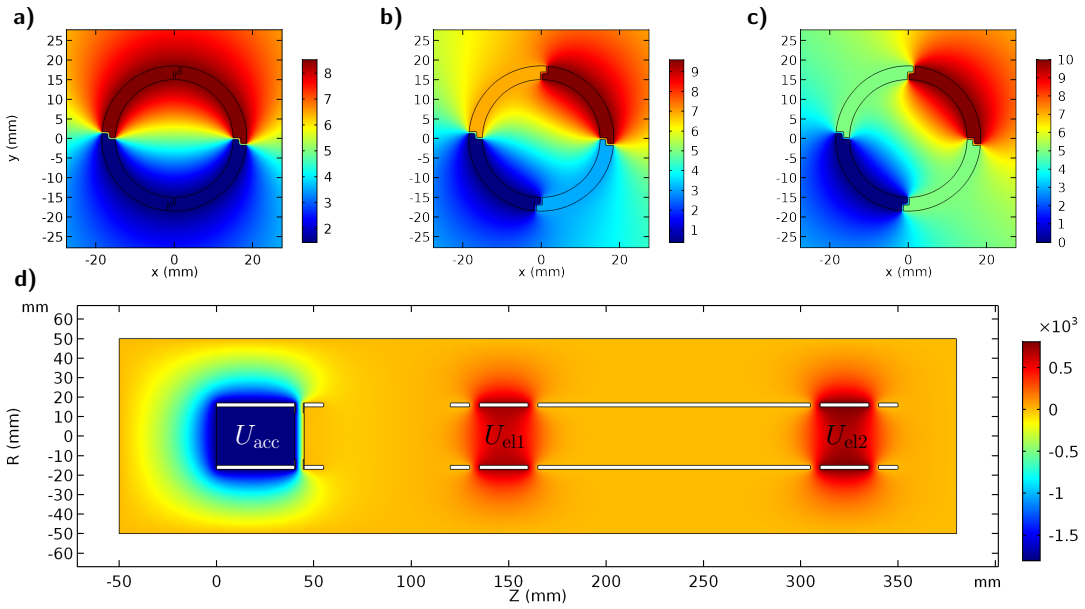

Figure 3.3.: **a) - c)** Plot of the electrode potentials (unit is volt) used for beam steering. The potentials are shown for $U_{st} = 10V$ and for steering at angles $\phi = \{0, 1/8, 1/4\}\pi$. **d)** Plot of the acceleration and collimation potential (unit is volt) for the settings: $U_{acc} = -1800\,\mathrm{V}$, $U_{el1} = 820\,\mathrm{V}$ and $U_{el2} = 710\,\mathrm{V}$.

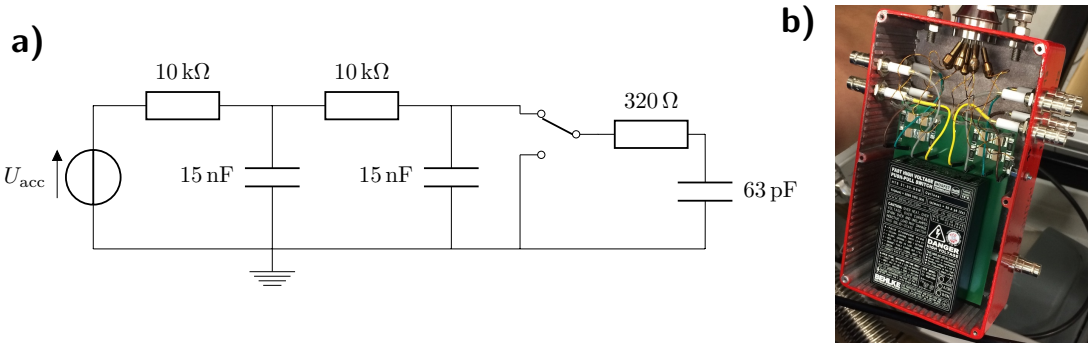

Figure 3.4.: **a)** Circuit providing the high peak currents for ramping of the pulsed tube. **b)** Image of the high–voltage switch and the PCB used to supply the voltages for the pulsed tube and einzel lenses. The electronics are mounted in a box next to the vacuum feedthrough to keep the cables short.

different steering directions and $U_{el} = 0$ is shown in figure 3.3 a–c). As can be seen, these potential settings lead to a radial electric field component, that is fairly homogeneous for coaxial beams. The steering is mainly used for smaller corrections to the particle trajectory, and U_{st} usually around two orders of magnitude smaller than U_{acc}. An effect of the steering on the collimation, due to the asymmetry in the potential, can therefore normally be neglected.

The voltages for the electrodes are supplied by CAEN modules, using a *CAEN A1821N* board for the negative, and a *CAEN A1832P* for positive voltages. These can provide up to ±6 kV, but are limited to a current of 200 µA. The pulsed tube has a capacity of ≈ 60 pF. Since the ramping of the acceleration voltage has to happen within a microsecond, instantaneous currents of several amperes are required, which cannot be provided by the power supplies. The circuit used to circumvent this problem is shown in figure 3.4 a). A passive, second–order low–pass filter ($R = 10\,\text{k}\Omega$, $C = 15\,\text{nF}$) is used between the supply and the electrodes. Apart from reducing electronic noise coming from the high–voltage supplies, the filter capacity next to the high–voltage switch acts as a charge buffer, and provides the large currents needed to ramp the pulsed tube. To prevent damage to the switch, the current is limited by a shunt resistor $R = 320\,\Omega$ to around 5.6 A. All circuit elements needed to supply the pulsed tube and einzel lenses are assembled on a single printed circuit board (PCB) (see figure 3.4 b)).

3.1.3. Mass filtration

The accelerated anion beam still includes different negatively charged particles, generated by the SSEV and the DBD. Since Penning traps are not mass selective, these species would be equally trapped together with the C_2^-. While trace impurities of atomic and molecular anions do not significantly interfere with the sympathetic cooling, larger amounts can lead to altered plasma dynamics in the trap by centrifugal separation

and steal cooling power from the actual goal of cooling the antiprotons. To single out the C_2^-, a Wien filter (also called velocity filter) is used.

This filter uses a crossed magnetic and electric field to deflect species, depending on their velocity and charge. For the case of an electric field in $\hat{\mathbf{x}}$, a magnetic field in $\hat{\mathbf{y}}$ and a beam in $\hat{\mathbf{z}}$ direction, the force acting on a particle with charge q is:

$$\mathbf{F}_\mathrm{L} = q\left(E\hat{\mathbf{x}} + vB\hat{\mathbf{z}} \times \hat{\mathbf{y}}\right) = q\left(E - vB\right)\hat{\mathbf{x}}. \tag{3.2}$$

By tuning E and B, the force can therefore be made to vanish for specific values of v, meaning that particles at this velocity are not deflected and can be separated from the rest. The acceleration scheme used in the setup defines the kinetic energy of the beam to $E_\mathrm{kin} = |qU_\mathrm{acc}|$, making the particle velocity a function of the respective mass $v = \sqrt{\frac{2|qU_\mathrm{acc}|}{m}}$. In this setting, the Wien filter therefore effectively acts as a mass filter for the incoming particle beam.

The used device is a *Beam Imaging Solutions Inc., model 600–H* velocity filter, with a nominal resolution of $m/\Delta m \sim 400$. It features electromagnetic coils, which, under rated conditions, allow to produce nominal magnetic fields up to 100 mT. In pulsed operation, which limits heating of the coils, it was found experimentally that the device can be used for mass filtration with magnetic fields up to 175 mT. The nominal voltage that can be applied to the electrodes is 300 V. The electric field is produced by two main horizontal deflection plates, with a length of ≈ 15 cm, which are placed at a distance of ≈ 18 mm from each other. In addition, 12 shims allow fine tuning of the resulting electric field. A passive controller on the basis of a network of voltage dividers is supplied, and allows to tune the electrode voltages via potentiometers. Due to this configuration, a single voltage supply is sufficient to operate the mass filter. In addition to the horizontal deflection, two separate electrodes, with their own voltage supply, allow vertical deflection of the beam at the entrance of the device. For the measurements in this thesis, the horizontal electrodes were operated with the factory potentiometer settings.

An important figure is the mass resolution, required to separate C_2^- from the bulk of the beam. To this end, it is interesting to look at the masses of all species possibly produced. Ignoring the complex formation dynamics, table 3.1 shows a list of all anions that can be formed from an initial gas mixture of acetylene, carbon dioxide, neon and helium, by naive permutation of the constituents. Anions with negative EA can be neglected, since they are unstable and would either decay before entering the Penning trap or could be easily removed via photodetachment in flight. Likewise doubly charged anions were ignored as unstable (Boldyrev and Simons, 1993). The masses of the remaining species are shown in figure 3.5, together with the relative abundance of their naturally occurring isotopes. As can be seen, $^{12}C_2^-$ at 24 u is separated from other species by 1 u with the exception of a low abundance isotope of NeH^-. A resolution of 1 u at 24 u, to separate $^{12}C_2H^-$ and $^{12}C_2^-$, is therefore sufficient, and can be achieved with the device in use.

3.1.4. Detection of the anions

The produced anions are analysed using two different detectors, a FC for charge detection and a MCP for monitoring the shape of the beam. For the former, a shielded design for

Species	EA (eV)	Reference
CO_2^-	-0.6	(Knapp et al., 1986)
O_2^-	0.45	(K. M. Ervin et al., 2003)
CO^-	1.26	(Refaey and Franklin, 1976)
$C_2H_2^-$	unstable	(Dressler and Allan, 1987)
H_2CC^-	0.484	(DeVine et al., 2018; Gerardi et al., 2010)
C_2H^-	2.97	(Zhou et al., 2007)
C_2^-	3.27	(M. K. Ervin and Lineberger, 1991)
NeH^-	0.73	(Harris et al., 2014)
Ne^-	-1.2	(Bratsch and Lagowski, 1986)
F^-	3.40	(Blondel et al., 2001)
H_2O^-	$< 10^{-4}$	(Chipman, 1978)
HO^-	1.83	(Smith et al., 1997)
O^-	1.46	(Blondel et al., 2005)
CH_4^-	?	probably unstable
CH_3^-	0.08	(Ellison et al., 1978)
CH_2^-	0.65	(Leopold et al., 1985)
CH^-	1.24	(Kasdan et al., 1975)
C^-	1.26	(Bresteau et al., 2016)
He^-	-0.5	(Bratsch and Lagowski, 1986)
H_2^-	unstable	(Heber et al., 2006)
H^-	0.75	(Lykke et al., 1991)

Table 3.1.: List of possibly produced anions based on naive combination of the gas mixture constituents. Stable anions have a positive electron affinity (Bartmess, 2018, retrieved 23.04.2018). An extensive review can also be found in (Rienstra-Kiracofe et al., 2002). F^- is included for reasons discussed in section 3.3.

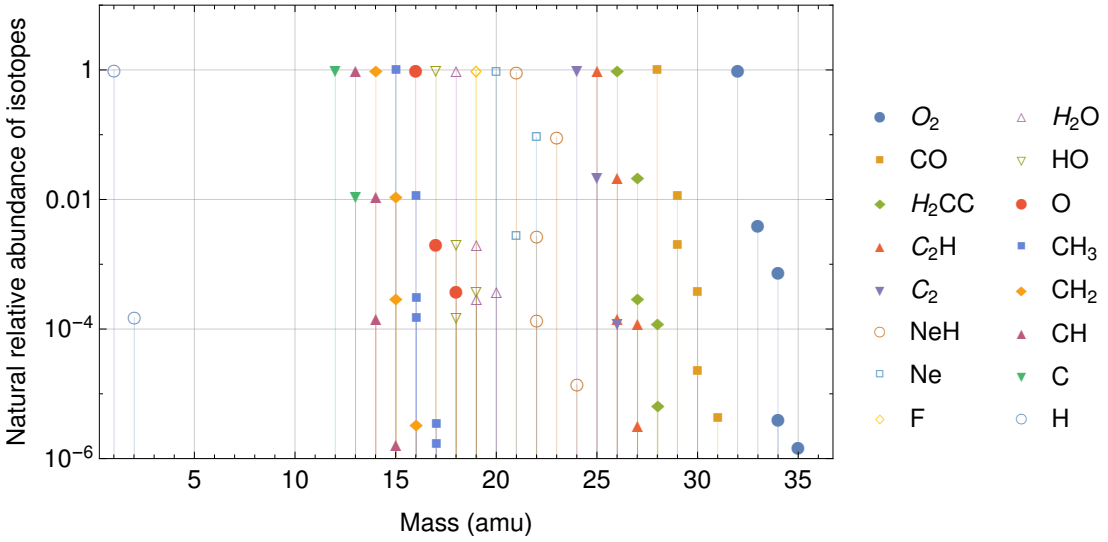

Figure 3.5.: Plot of the natural relative isotope abundance and masses of the stable anions from table 3.1. The plot was created on the basis of the natural isotope abundances of the atomic constituents of each species. Isotopes with an abundance $< 1 \times 10^{-6}$ are not shown. The isotope data was retrieved from (Wolfram Alpha LLC, 2017).

the FC was used (see figure 3.2 f)). Here, the electrode is surrounded by a grounded shield, with a single 5 mm entrance on one side. In addition, the entrance is surrounded by a suppression plate. This is a ring–shaped electrode, isolated from the shield and FC, which can be biased to several hundred volts. This way it can either be used to repel unwanted charges, or suppress reflection of secondary electrons during the impact of the beam. The conducting parts are machined from brass, while the isolators are made from ceramic. A shielded vacuum cable then connects the cup to a *Femto, DLPCA-200* variable gain current amplifier. The amplified signal is recorded by an analogue–to–digital converter (ADC), which is controlled by the FPGA.

The MCP is a commercial system (*Hamamatsu F2223–21P379*), with a diameter of 24 mm, using a phosphor screen as a readout device. The phosphor screen is imaged by a triggered camera (*Allied Vision Mako G–234B PoE*), whose exposure time can be set with a precision of ±9.6 µs. The optical imaging system is self–built, using two lenses with a diameter of 5 cm on a breadboard. The voltages in the kV range that are needed for amplification are supplied by the *CAEN A1832P*.

3.1.5. Enhancement cavity for photodetachment laser spectroscopy

While these measurements are not part of this thesis, the setup includes the possibility for flyby photodetachment spectroscopy, as a tool for the characterisation of the initial electronic population of the molecules. As is described in section 2.3, the $A^2\Pi \leftrightarrow X^2\Sigma$

transition is an interesting candidate for photodetachment spectroscopy, requiring a laser at 2.54 µm for resonant excitation and a laser with a wavelength below 446 nm for the detachment from the $A^2\Pi$ state. To increase the interaction time with the laser, the spectroscopy module is positioned in front of the skimmer, before the particles are accelerated (see figure 3.1). Since the detachment has to happen in the short time–window, during which the molecules are in the excited state $A^2\Pi$ and are transversing the laser, the detachment laser needs to have a high intensity. For budget reasons, in this setup this is achieved by enhancing a low–power laser in a high–finesse optical resonator (also called an enhancement cavity)

An extensive discussion of optical resonators can be found in (Hodgson and Weber, 2005), from which the most important relations are summarised here. A simple example of an optical resonator consists of two mirrors with polished backs facing each other. If a laser beam enters this arrangement via one of the mirrors, it is subsequently reflected back and forth by the mirrors, and therefore interferes with itself. In order for the beam to stay confined in the resonator, the curvature r of the mirrors needs to fulfill the relation:

$$0 < g_1 g_2 < 1 \qquad\qquad g_i = 1 - \frac{L}{r_i}, \tag{3.3}$$

where L is the distance between the two mirrors. Under realistic conditions, the reflectivity of the mirrors is finite, and only a fraction R_M of the light is reflected by the mirrors. Taking this into account, expressions for the light reflected by and transmitted through the resonator can be calculated:

$$R_\mathrm{C} = \frac{4R_\mathrm{M}\sin^2(kL)}{(1-R_\mathrm{M})^2 + 4R_\mathrm{M}\sin^2(kL)} \qquad\qquad T_\mathrm{C} = \frac{(1-R_\mathrm{M})^2}{(1-R_\mathrm{M})^2 + 4R_\mathrm{M}\sin^2(kL)}, \tag{3.4}$$

where k is the wavenumber of the laser. From this it can be seen that for light with frequencies:

$$\nu = n\Delta\nu = n\frac{c}{2L} \qquad n \in \mathbb{N}^+ \tag{3.5}$$

the resonance condition of the cavity is reached. $\Delta\nu$ is also called the free spectral range (FSR) of the resonator. At these frequencies the phase shift of a round trip between the two mirrors is 2π, which intuitively explains the constructive interference and resonance. The spatially allowed modes inside the cavity are the Hermite–Gaussian modes. For the fundamental mode, the waist w_0 in the case of a symmetric resonator is given by:

$$w_0 = k^{-1/2}\left(L\left(2r - L\right)\right)^{1/4}. \tag{3.6}$$

The enhanced energy density at resonance inside the cavity is then given by:

$$\rho_\mathrm{max} = \frac{2P}{c\pi w_0^2}\frac{1+R_\mathrm{M}}{1-R_\mathrm{M}}, \tag{3.7}$$

where P is the power of the beam entering the cavity. Equation (3.4) also allows to determine the spectral FWHM of the resonator:

$$\delta\nu = \left|\ln(R_\mathrm{M})\right|\frac{c}{2\pi L} \simeq \frac{c\left(1-R_\mathrm{M}\right)}{2\pi L}, \tag{3.8}$$

which is connected to the storage time of the light in the resonator. In the last step, $|\ln(R_{\mathrm{M}})|$ was approximated as the first term of its Taylor series around one, which is a reasonable approximation in the case of high quality mirrors. If the laser is turned off abruptly, the light in the resonator leaks out in transmission. The time it takes the energy density to drop by a fraction of $1/e$ is connected to the spectral FWHM according to:

$$\tau = \frac{L}{c\,|\ln(R_{\mathrm{M}})|} = \frac{1}{2\pi\delta\nu} \simeq \frac{L}{c\,(1-R_{\mathrm{M}})}. \tag{3.9}$$

In the literature, optical resonators are often characterised by the so–called *finesse* $\mathcal{F}$:

$$\mathcal{F} = \frac{\Delta\nu}{\delta\nu} = \frac{\pi}{|\ln(R_{\mathrm{M}})|} \simeq \frac{\pi}{1-R_{\mathrm{M}}}. \tag{3.10}$$

High values of $\mathcal{F}$ are therefore an indicator for good–quality mirrors, and high light amplification inside the resonator. The resonator described in this thesis uses custom–made, concave mirrors from *Layertec*, with a quoted reflectivity R_{M} above 0.9997 at 399 nm, a curvature of 400 mm and a diameter of 12.7 mm. A picture of the resonator at its mounting position in front of the skimmer can be seen in figure 3.2 g). The mirrors are mounted on a specially designed holder, which was machined from low thermal expansion *Invar* steel, at a distance of 38.6 mm from each other. For vibration isolation, the holder is mounted on a separate vacuum flange via four steel rods. The flange is firmly attached to the optical table, on which the rest of the laser setup is placed. A bellow then isolates the flange from the vacuum setup.

High–performance resonators with a finesse of 10 000 or more and lengths in the cm range, have spectral widths of 500 kHz or smaller. Given a similar small spectral width of the laser, fluctuations in the environmental conditions (e.g. thermal drifts or vibrations) can change the parameters of the resonator inside the laser or the enhancement resonator, causing them to drift out of resonance. It is therefore necessary to stabilise them with regard to each other. Two different approaches are usually employed for this. The first is to mount one of the resonator mirrors on a piezo actuator, which allows to change the distance between the mirrors and thereby adjust the resonance frequency. The second is to use a laser which can be frequency modulated. In both cases it is necessary to have a reference signal, which allows to determine how far off resonance the laser and the resonator are with respect to each other.

A straightforward approach would be to monitor the transmitted or reflected laser intensity of the enhancement resonator (see eq. (3.4)). By operating on the flank of the resonance signal, a drift of either the resonator or the laser leads to a proportional change in the intensity. This approach has two disadvantages. Firstly, it cannot distinguish between frequency drifts and drifts in the laser intensity itself. Secondly, it cannot be used to stabilise on the maximum of the resonance, since the reference signal is symmetric around it, and hence it cannot be determined in which direction the correction has to be. These problems are overcome by the Pound–Drever–Hall (PDH) laser frequency stabilisation scheme. The reader is referred to (Black, 2001) for a detailed introduction to this technique. It is based on a constant, small and high frequency modulation of the laser. The latter can be seen in the reflected intensity of the resonator. The crucial

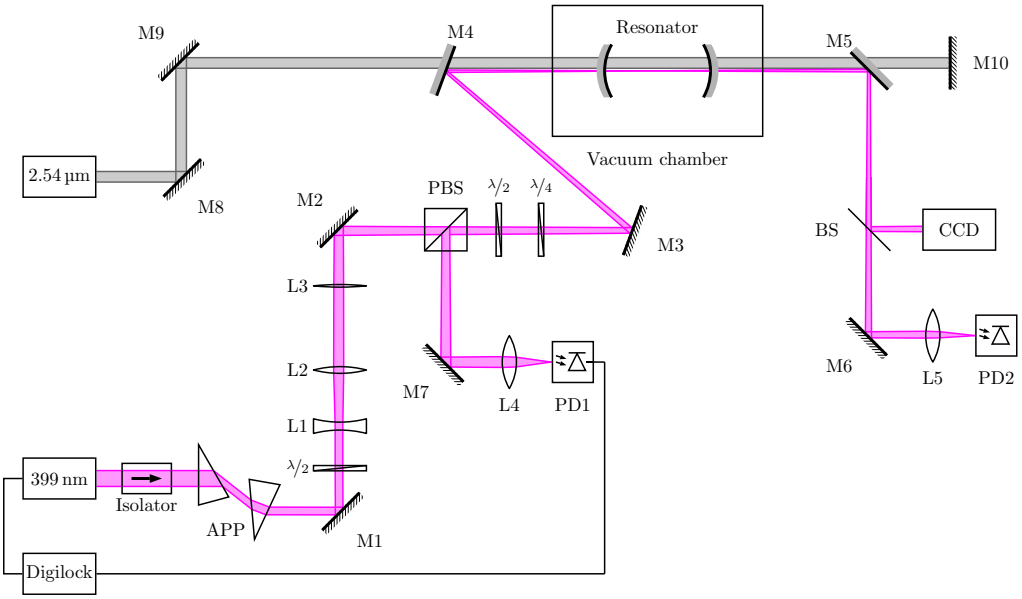

Figure 3.6.: Schematic of the optical setup for the photodetachment spectroscopy. The focus is on the enhancement resonator and the optics for its interaction with the 399 nm laser. The preparatory and stabilising optics of the 2.54 µm laser are omitted. The graphic was made using the `pst − optexp` package for LaTeX (Bersch, 2014).

effect is then, that the reflected signal experiences a phase change around the resonance with respect to the applied modulation. By monitoring the reflected intensity of the resonator and comparing it to the applied modulation, an asymmetric reference signal (also called error signal) can therefore be deduced.

A schematic overview of the optical setup, that was built for enhancing a low power laser at 399 nm in a resonator, is shown in figure 3.6. The used laser is a *Toptica DL Pro HP System*, with a line width < 150 kHz. The laser is grating–stabilised and has two possibilities for modulation. The first is fast, at up to 25 MHz, and achieved by modulating the current of the laser diode. The second is slow ~ 5 kHz, but allows modulations in a larger frequency range up to ~ 20 GHz, by applying a voltage to a piezo which changes the position of the stabilising grating. The laser has an internal optical isolator, but it was found that an additional external 30 dB isolator is necessary to eliminate destabilising back reflections from the resonator. An anamorphic prism pair (APP) is used to correct the initial spacial ellipticity of the laser beam. A system of three lenses is then used to match the spacial mode of the laser to the resonator. To monitor the reflected light from the resonator, a polarising beam splitter (PBS), combined with a $\lambda/4$ plate is used. The light initially transmitted by the PBS, which is reflected by the resonator, passes the $\lambda/4$ plate twice and therefore experiences a 90° rotation of its polarisation. As a result, it is reflected by the PBS. A second $\lambda/2$ plate allows to correct additional polarisation changes, caused by the optical elements in the path. The

reflected light is then monitored by a fast photodiode (PD) (*Thorlabs PDA10A-EC*) with a bandwidth of 150 MHz. The PBS also gives control over the laser power sent to the resonator, by adjusting the polarisation using the $\lambda/2$ plate after mirror M1. As an additional diagnostic tool and to ease the alignment procedures, the light transmitted through the resonator is also monitored. After a 50/50 beam splitter (BS), one arm is sent to a fast photodiode identical to the one in reflection. The other arm is monitored by the bare CCD of a *Playstation eye* USB camera, and allows to determine the spacial mode in the resonator. The resonator mirrors, vacuum windows, as well as mirrors M4 and M5 feature a calcium fluorite substrate, which is transmissive at 399 nm and 2.54 µm. This allows to superimpose the 2.54 µm laser via mirrors M9 and M10, by using a reflective laser line coating for 399 nm on mirrors M4 and M5. The optical components necessary to control and stabilise the 2.54 µm laser are not covered in this thesis and omitted in figure 3.6.

Stabilising the 399 nm laser to the resonator requires a feedback circuit on the basis of the voltage signal from PD1. This is implemented using a *Toptica Digilock* system. The latter uses fast ADCs, DACs and an FPGA for signal processing, and is designed specifically for the purpose of laser stabilisation. To this end, it allows to generate the PDH signal for the modulation of the laser and to demodulate the reflection signal from PD1. On the basis of the error signal from the demodulation, two proportional–integral–derivative (PID) controllers can be implemented on the Digilock, covering different kinds of drifts. The first controls the feedback to the piezo moving the laser grating and allows to compensate slow drifts (e.g. thermal changes of the resonator substrate). The second controls the feedback on the laser diode current and is used to correct fast frequency changes (e.g. electronic noise on the laser controls). The parameters are controlled via a computer interface.

3.2. Experimental results: acceleration and beam steering

3.2.1. Ion production and stability of the DBD

Three different gas mixtures were investigated in the measurements: 5 % C_2H_2, 3 % CO_2 in helium, 2 % C_2H_2, 2 % CO_2 in neon and 5 % C_2H_2 in neon. Using the hot cathode for stabilisation, it was possible to reliably operate the DBD with all three mixtures, with a supply pressure of 8 bar at the SSEV. In single shot operation, a pressure of 6×10^{-6} mbar can be maintained in the valve chamber. The stability of the discharge can be monitored using the FC, which is placed 578 mm downstream of the SSEV nozzle. Figure 3.7 shows the current signal, as recorded by the FC, when the suppression plate is biased to −30 V and all other electrodes are grounded. This way, only positive charges can reach the electrode. The valve is triggered at $t = 0$, followed by the DBD at $t = 80$ µs which results in a pick–up that can be seen in the FC time trace. The particles then drift through the vacuum until they reach the FC. From the arrival time, the velocity of the gas bunch can therefore be estimated to be $\sim 1500\,\mathrm{m\,s^{-1}}$ for the case of helium, and $\sim 825\,\mathrm{m\,s^{-1}}$ if neon is used as carrier gas. In the case of $H^{\pm}$, the velocities correspond to energies in the $E_{\mathrm{kin}} \sim 100$ meV and $E_{\mathrm{kin}} \sim 30$ meV range. The different velocities are

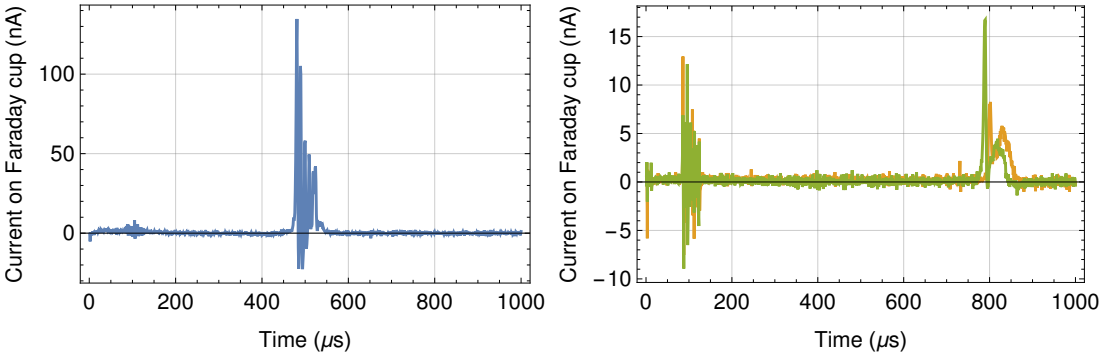

Figure 3.7.: Current signal from the FC, placed directly behind the acceleration and steering stack at a distance of 578 mm from the SSEV nozzle. The suppression plate of the FC was biased to −30 V, allowing only positive charges to reach the electrode. *Left:* using the gas mixture 5 % C_2H_2, 3 % CO_2 in helium. *Right:* using 2 % C_2H_2, 2 % CO_2 in neon and 5 % C_2H_2 in neon.

a result of lower molecular velocities and higher viscosities of heavier carrier gases, and are in reasonable agreement with the literature (Even, 2015).

The stability of the DBD can be quantified by integrating the FC signal for consecutive shots, as shown in figure 3.7. Figure 3.8 shows a histogram of the integrated FC signal for 500 shots, using 5 % C_2H_2, 3 % CO_2 in helium. To visualise the fluctuations, the axis is normalised to the mean value of the distribution, by applying the transformation $x \to x/\bar{x} - 1$. The standard deviation of the scaled distribution is $\sigma \approx 0.12$. The total number of produced charges therefore fluctuates by around 10 %. A similar behaviour was observed for the other two gas mixtures.

3.2.2. Acceleration of the particles

The time traces of the FC are also a good means to monitor the acceleration of the particles. Using identical parameters as in figure 3.7, figure 3.9 shows FC time traces, only this time using the pulsed tube for acceleration of the particles. The suppression plate was biased to −500 V in order to suppress the emission of secondary electrons from the FC. The pulsed tube is ramped to −1.8 kV at $t = 270\,\mu s$, $t = 400\,\mu s$ and $t = 390\,\mu s$ respectively, and maintains the voltage for 500 µs. The fast ramping again results in a pick up, and can therefore be seen in the signal. It is cut for higher signal amplitudes due to the small dynamic range of the ADC. Comparing the traces to the unaccelerated case, the effect of the pulsing can be clearly seen. In addition, the times of the ramp agree with the estimated particle velocities prior to the acceleration and the distance of 265 mm between the SSEV nozzle and the end of the pulsed tube.

The order of magnitude of negative charges recorded per shot by the FC, as in the data shown in figure 3.9, is $\sim 1 \times 10^7$. This number however, should be seen as a lower bound, since the FC is too small to record the whole beam and too near to the einzel lens system to allow for a small enough focus. It must also be pointed out, that at this point

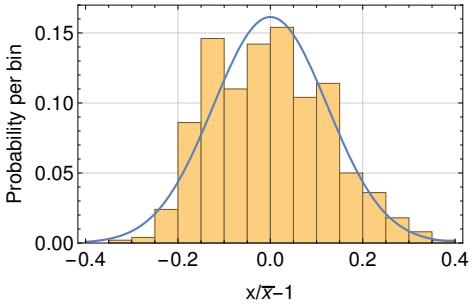

Figure 3.8.: Histogram of the integrated, unaccelerated FC signal as shown in figure 3.7, on the basis of 500 shots from the SSEV. The gas mixture 5 % C_2H_2, 3 % CO_2 in helium was used. In order to visualise the fluctuation, the axis was scaled to the mean of the distribution, resulting in a standard deviation of $\sigma \approx 0.12$. The blue line shows a normal distribution with the same mean and standard deviation.

in the setup, the bunch still consists of all different kinds of anions that are produced by the DBD. Furthermore it is noteworthy, that 3.7 shows the detection of positive charges, while only anions are accelerated and detected in 3.9. This was done intentionally, to show and underline that both ions and anions are produced from the used gas mixture in the DBD. The particles then travel as a quasineutral bunch, and can be separated later by using the appropriate voltages.

3.2.3. Collimation and steering

While care was taken in the design and construction of the pulsed tube, to limit deterioration of the beam quality, some effects cannot be prevented. For an initial characterisation of the beam, the MCP was mounted between the first FC mounting position and the mass filter (see figure 3.1). The measurement showed that the beam leaving the einzel lens system is large enough to clip at the endelectrode. Since the beam is constrained to a 6 mm diameter by the iris after the last acceleration mesh, this implies a significant divergence. Due to a lack of diagnostic tools at the relevant positions, only speculations can be made about its origin. It is conceivable that warping of the meshes, space charge effects arising from the charge separation of the neutral particle bunch, fringe field effects from the mesh or a combination of them are responsible.

The effect of the einzel lens system on the beam at the near position, without using steering, is illustrated in figure 3.10. The used gas mixture was 5 % C_2H_2 in neon and the MCP settings were identical for all three images. The applied einzel lens voltages are given in the figure. While a focusing effect can be clearly observed, it is also evident that the beam has a tilt or offset with respect to the axis of the experimental setup. This leads to aberrations by the einzel lenses which can be seen in the images, together with clipping of the beam by the electrodes.

The functionality of the steering, using the segments of the einzel lenses, is shown in

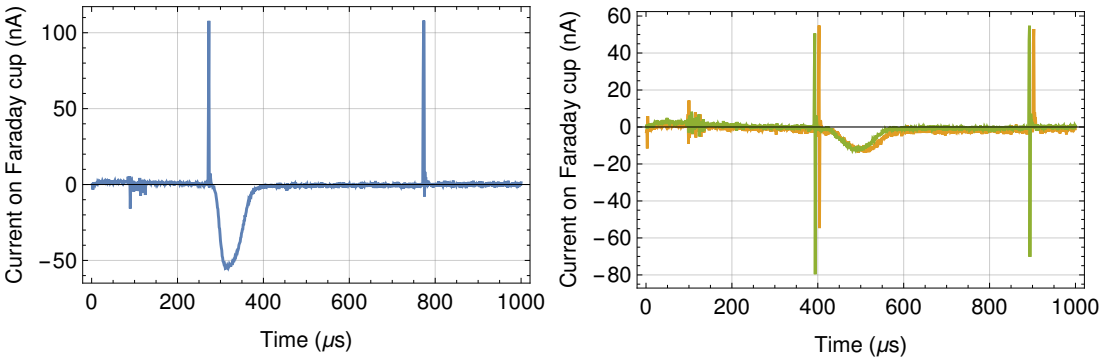

Figure 3.9.: Current signal on the FC, using the pulsed tube for acceleration of the particle bunch and the einzel lenses to focus the beam. The suppression plate of the FC is biased to −500 V. The spikes are pick up signals due to the ramping of the pulsed tube. *Left:* using the gas mixture 5 % C_2H_2, 3 % CO_2 in helium. *Right:* using 2 % C_2H_2, 2 % CO_2 in neon and 5 % C_2H_2 in neon.

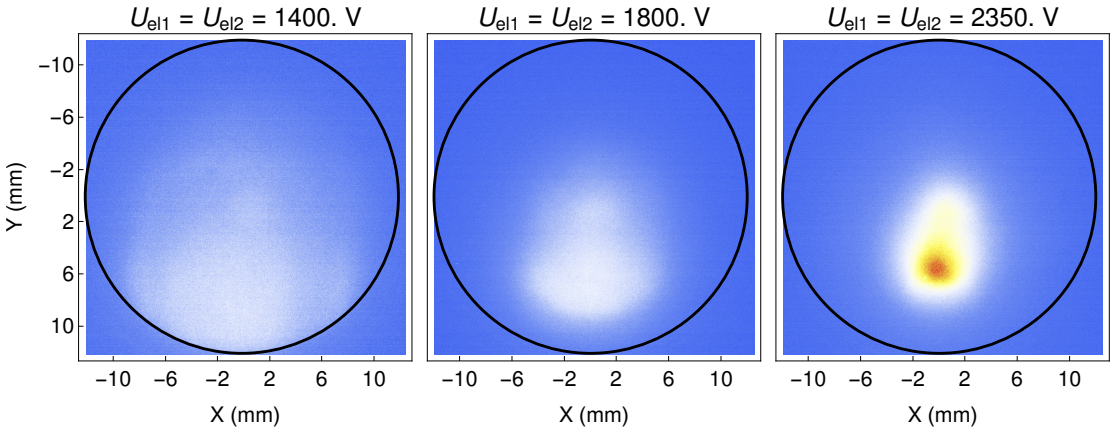

Figure 3.10.: MCP images of the 1.8 keV accelerated anion pulse after being focused by the einzel lenses. Both lenses were set to equal positive voltages and no steering voltages were applied to the segments. The used gas mixture was 5 % C_2H_2 in neon. All three images were taken with identical MCP and camera settings. For comparability, the images use the same colour scale. A black circle shows the outlines of the phosphor screen.

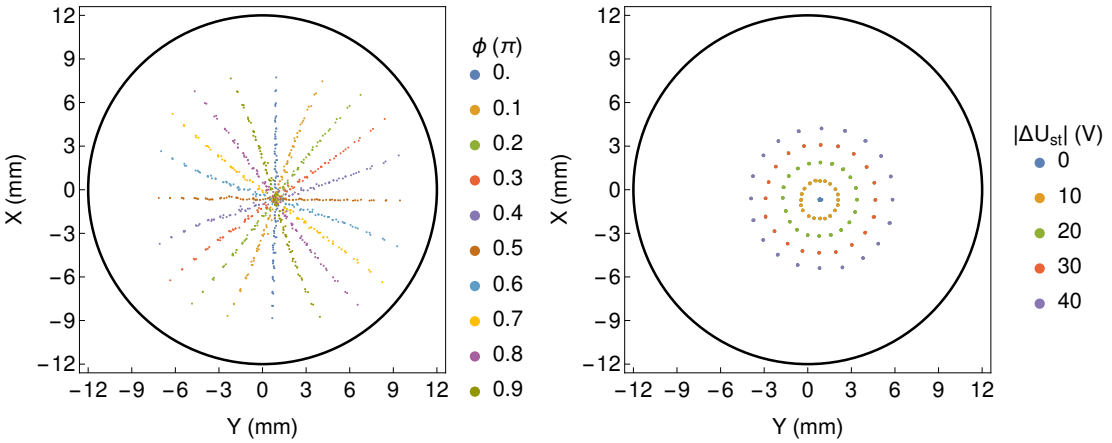

Figure 3.11.: Illustration of the functionality of the steering. The markers show the centre position of the beam for different steering parameters. A black line shows the outline of the phosphor screen (see text for details). *Left:* the steering amplitude of both einzel lenses was scanned independently from $-40\,\mathrm{V}$ to $40\,\mathrm{V}$ in steps of $10\,\mathrm{V}$ for different steering angles. The colour coding shows the different angles. *Right:* part of the data shown on the left, with $U_{\mathrm{st}} = 0\,\mathrm{V}$ for the second einzel lens. Colour coded for the amplitude.

figure 3.11. For this measurement, the 1.8 keV anion beam was focused onto the MCP, while scanning through different steering angles and amplitudes and recording an image of the beam for each setting. The images were then processed and the centre $\vec{c}$ of the beam was located. For this, the pixels corresponding to the active area of the phosphor screen were selected and the minimum and maximum intensity value determined. On this basis, the top 50 % of the intensity values were selected and used to calculate a weighted mean of the corresponding pixels:

$$\vec{c} = \left(\sum_i \chi_i\right)^{-1} \sum_i \vec{x}_i \chi_i, \tag{3.11}$$

where the sum is over the selected top 50 % pixels, $\vec{x}$ denotes the position and χ the intensity of the pixel. The plot on the left shows the calculated beam centre for a large parameter scan. For different steering angles ϕ (colour coding of the plot), the amplitude U_{st} of both einzel lenses was scanned independently from $-40\,\mathrm{V}$ to $40\,\mathrm{V}$, in steps of $10\,\mathrm{V}$ (see eq. (3.1)). As can be seen, there is good agreement between the set parameters and the effect on the beam. The plot on the right highlights the effect of the steering amplitude. It shows a part of the data plotted on the left, where only the first einzel lens was used for steering, this time colour coded for the amplitude U_{st} of the second einzel lens. Again there is good agreement between the parameters and the influence on the beam.

According to the manufacturer of the mass filter, the device requires a collimated beam with a diameter less than 10 mm in order to be able to resolve masses 24 u and 25 u. Using the einzel lens system, it was tried to achieve these parameters by making a two–point measurement. For this, the MCP was placed once at the first FC mounting position, where figures 3.10 and 3.11 were recorded, and then moved to the far position as shown in figure 3.1. At each position, a large scan over the steering and einzel lens parameters was performed. By comparing the beam sizes at the two positions for identical settings, it was possible to determine an optimal set of parameters. It was found, that the size of the beam cannot be reduced below 15 mm while forming a collimated beam. The working hypothesis at the time of the measurement was, that this is due to the unexpectedly strong divergence of the beam after the acceleration and the distance between the last mesh and the first einzel lens. This could be improved by changing the geometry of the einzel lens system. However, due to a constraint on time it was decided to proceed with the measurements with the mass filter and ensure collimation of the beam using irises in addition to the einzel lens system.

3.3. Experimental results: mass spectrometry

The irises are placed directly in front of and after the Wien filter, each with a diameter of 2 mm (see figure 3.1 for an illustration). Even though the mass filter was readily bought mounted in a DN200 vacuum chamber, a closer inspection showed that it has a minor tilt with respect to the chamber. While this can be compensated by using bellows for the connection to the setup and a separate translatable mount for the mass filter chamber, this option had to be discarded due to time and budget reasons. Instead, the irises were aligned on axis with the tilt, and the steering capabilities of the einzel lenses and the deflection electrodes of the filter used to guide the beam through the assembly. This was done by optimising the focusing and steering parameters until the signal on the MCP downstream was maximised. The found settings were in agreement with the parameters of the collimated beam, found in the two–point measurement which was discussed in the previous section.

Using this setup, mass spectra were recorded for the three gas mixtures mentioned in the previous sections. For this, the horizontal deflection was set to a constant 350 V and the supply current of the magnet coil scanned over a range corresponding to 0 u to 30 u. The resulting signal on the MCP was then recorded. For each current setting, a specific mass can pass the filter undeflected and reaches the MCP. The resolution of the spectrum then depends on the strength of the deflection of unwanted masses, the drift length to the MCP, the size of the beam at the detector and the size of the integrated window. The window size can be controlled by selecting only part of the phosphor screen during the evaluation.

The resulting spectra are shown in figure 3.12. Here, the x–axis is already transformed from current to atomic masses, using the relationship:

$$m = 2eU_{\mathrm{acc}} \left(\frac{d_{\mathrm{el}} B\left(I_{\mathrm{coil}}\right)}{U_{\mathrm{el}}} \right)^2 , \tag{3.12}$$

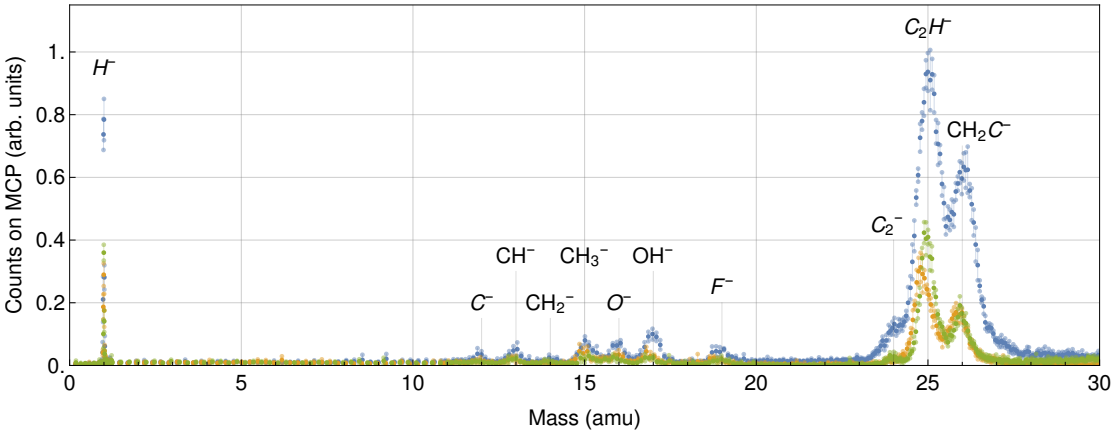

Figure 3.12.: Mass spectra recorded by integrating the particle signal behind the mass filter with the MCP for different coil currents. The spectra were measured for three different gas mixtures: 5 % C_2H_2, 3 % CO_2 in helium, 2 % C_2H_2, 2 % CO_2 in neon and 5 % C_2H_2 in neon. Annotations show the most likely anionic candidate for each signal. See text for details.

where U_{acc} is the acceleration voltage, d_{el} the distance between the horizontal deflection electrodes, U_{el} the voltage applied to the deflection electrodes and $B\left(I_{\mathrm{coil}}\right)$ the linear relationship between coil current I_{coil} and the resulting magnetic field B. An empirical function for $B\left(I_{\mathrm{coil}}\right)$ is provided by the supplier. Expression (3.12) results from equation (3.2) for the case that the forces cancel (the undeflected beam), the relationship between velocity and acceleration voltage $v = \sqrt{\frac{2|qU_{\mathrm{acc}}|}{m}}$ and by approximating the electric field of the deflection plates as $E = {}^{U_{\mathrm{el}}}/_{d_{\mathrm{el}}}$. Due to several imperfections in the experimental setup, the $I \rightarrow m$ transformation of the x–axis results in obviously unphysical signals at fractions of an atomic mass unit. By looking at equation (3.12), it is easy to see that the limited accuracy of the high–voltage power supplies will lead to errors in U_{acc} and U_{el}. Likewise, hysteresis in the yoke of the mass filter magnet can do the same for the $B\left(I_{\mathrm{coil}}\right)$ term. In addition, the approximation $E = {}^{U_{\mathrm{el}}}/_{d_{\mathrm{el}}}$ is only valid for on–axis beams in the mass filter. Since the irises and the steering of the beam have to account for the tilt of the mass filter, mechanical imperfections of the mounts can lead to additional shifts due to fringe field effects.

While it could be tried to characterise and account for these imperfections, a more practical approach is to calibrate the mass spectrum. To this end, it was tried to ignite a gas mixture of 5 % O_2 in helium with the DBD. It was planned to use an expected O^- signal for the calibration. Even though a large parameter range was tried out, it was not possible to create a detectable amount of anions. For this reason, the mass spectrum shown in 3.12 was calibrated using the expected H^-, C^- and CH^- signals. The details of this procedure would distract from the topic of this section and were therefore moved to the appendix A.3. Even though this approach is less certain, the resulting integer

mass signals agree with the used assumption and the knowledge about the content of the gas mixtures.

The y–axis is proportional to the summed pixel intensities of a 2.5 mm, vertical window in the centre of the MCP. For the measurement, five consecutive shots were integrated on the camera in a time window of 1 s. This is a compromise between stray–light, which is increasing the noise on the camera due to the prolonged exposure and a limit on the frequency of the shots due to the pressure building up in the valve chamber. For each datapoint, five of these integrated burst were recorded and averaged. The error bars show the standard deviation of the respective ensemble. To facilitate comparisons of the peak sizes, the y–axis was scaled to unity by the maximally occurring value.

The labels in 3.12 show the most likely anionic candidates for the signals. Since the settings were identical for all three gas mixtures, a rough comparison can be made regarding the quantities of the produced anions. The main uncertainty concerning the comparability is the detection efficiency of the MCP for different anion species. Apart from performing a detailed calibration measurement, which is out of the scope of this thesis, the only data available on the detection efficiency of the device is shown in A.4. Even though there is the potential for variations on the order of 10 %, given the data in A.4, it seems reasonable to assume that amplitudes in a window of ±2 u around a specific mass are comparable. The fact that the measured distribution of the anions agrees with the gas content is further evidence, that the variance of the detection efficiency allows for at least a qualitative comparison. It is also interesting to see that there are significant differences regarding the overall production efficiency.

The signal at 19 u is the only one which cannot be explained by the constituents of the gas, but might be a result of the production method. The SSEV uses ceramics for the nozzle and for isolation of the DBD electrode. It was observed that prolonged use etches the ceramic parts and could therefore release F^-, given the right ceramic.

While being dwarfed by the larger acetylene products C_2H^- and H_2CC^-, there is a clear signal at 24 u, where $C_2{}^-$ is expected. Even though the final verification has to be done by laser spectroscopy, the three–peak structure is a strong indication that it is indeed the anion that is sought after. Using the FC at the far position in front of the MCP, an effort was made to determine the number of anions at the position of 24 u. However, in the current configuration the signal is too weak to be detected by the FC, even when using a high–performance amplifier. A rough estimate based on the recorded MCP images gives a lower limit of several dozens of anions per valve shot.

While the resolution is sufficient for the distinction of the main constituents of the anion beam, it is too low for a complete spatial separation and significantly below the rated resolution of the device. Three effects are mainly suspected to be responsible for this. The first is the velocity spread of the beam. Since the mass selection happens indirectly through velocity selection (see section 3.1.3), a spread of the velocity distribution increases the uncertainty in the mass spectrum. Even though fine gold meshes are used for a precise definition of the potential inside the pulsed tube, expansion due to space charge can still be a cause of such a spread. The second effect has its origin in the unsatisfactory solution for the tilt of the mass filter. Due to unavoidable alignment errors of the irises with respect to the tilt, it is likely that the beam still shows a residual

misalignment, which can cause aberrations if there is a velocity component in the horizontal direction. The third effect stems from the reduced flux due to the use of the irises. This makes it difficult to detect aberrations in the beam, which is necessary to fine–tune the electric field inside the mass filter by means of the shims. It is therefore likely that the device performs below its potential, since there are residual inhomogeneities present in the electric field.

3.4. Experimental results: enhancement cavity

This section presents the results obtained with the 399 nm enhancement cavity, described in section 3.1.5. For the operation of the photodetachment spectroscopy which it is built for, two properties are of special importance. Firstly, the light amplification needs to be achieved and verified to work at the needed level. This is discussed in 3.4.1. Secondly, the stable operation of the frequency lock of the laser to the resonator must be shown in the experimental environment. This particularly includes its robustness to the operation of the SSEV and the DBD, and is discussed in section 3.4.2.

3.4.1. Finesse and optical power in the cavity

The FSR of the cavity is a property which can simply be calculated from the distance between the mirrors (see eq. (3.5)). This distance is defined by the cavity holder as $L = (38.8 \pm 0.3)\,\mathrm{mm}$, which gives $\Delta\nu = (3.88 \pm 0.03)\,\mathrm{GHz}$ for the FSR. The error in L is the machining precision with which the holder was produced. Since determining the performance of the cavity is equal to determining its finesse, looking at (3.10), it can be seen that this requires either measuring the spectral FWHM $\delta\nu$ of the resonance, or the decay time τ (see eqs. (3.8) and (3.9)). If the line width of the used laser is much narrower than the cavity resonance, $\delta\nu$ can be determined by scanning the laser while measuring the reflection signal from the resonator. Since it is unlikely that this assumption is valid for the used setup, τ is measured instead.

Ideally, this is done by moving the laser into resonance with the cavity and then turning it off abruptly. Monitoring the exponential decay of the transmission signal then allows to determine τ. The nominal reflectivity for the used mirrors is $> 99.97\,\%$, making the decay rate an expected $\tau > 0.42\,\mu\mathrm{s}$ and resulting in a spectral width of $\delta\nu < 371\,\mathrm{kHz}$. The shutdown needs to happen on a timescale similar to this, which therefore requires a fast shutter like an acousto–optic modulator (AOM). Since such a device was not available, a slightly different approach was used.

By scanning the laser frequency fast enough, an effective turn off can be realised when the laser moves out of resonance. While this requires no additional hardware to the one needed for the lock, it has the disadvantage of allowing for interference effects between the laser and the cavity. In the setup, the measurement was realised using the piezo for the frequency scan and PD2 to monitor the signal (see figure 3.6). Figure 3.13 on the left shows the transmission signal of a single scan over the TEM00 mode of the cavity. As can be seen, there is a discrepancy between the exponential decay that is to be expected and the signal that is observed. After an initial pumping phase, where the

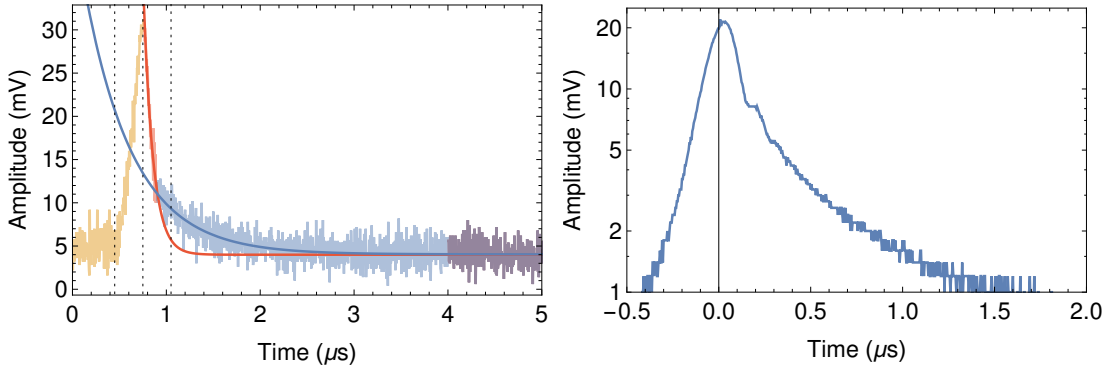

Figure 3.13.: Measurement of the cavity finesse. Both plots show the transmission signal while scanning the laser frequency over the resonance. Details can be found in the text. *Left:* plot of a single scan with two lines showing fits to the decay curve. The blue marked data and fit were used to determine the finesse. *Right:* average of 128 scans on a logarithmic scale. Interference between the detuned laser and the cavity can be seen.

laser moves into resonance and builds up energy in the resonator, a sharp drop can be seen, followed by a much slower decay of the transmission signal. This deviation from the expected exponential decay is most likely an interference effect, as was mentioned earlier. As described in detail in (An et al., 1995), the laser interacts with the cavity while moving out of resonance, which can lead to a significant interference.

Three vertical dotted lines are shown in the figure. From left to right they illustrate the onset of the resonance, the maximum and the onset mirrored around the maximum. As can be seen, the sharp drop stops shortly before the laser is expected to move out of resonance, which agrees with the interpretation of the interference. A beating can also be seen on the right in figure 3.13. Here the laser was scanned over the resonance, while averaging 128 traces of the transmission signal with an oscilloscope. A *Tektronix TDS 2024C* oscilloscope was used for the measurement and triggered on the rising side of the signal. The effect of the detuned laser is clearly visible on a logarithmic scale.

To determine the finesse, the trace on the left in figure 3.13 is fitted with an exponential function:

$$f(t) = a + b \exp\left(-\frac{(t - t_0)}{\tau}\right), \tag{3.13}$$

where a, b, t_0 and τ are parameters of the fit. This is done twice with different regions of the data. Once for the region marked red, which corresponds to the sharp drop and part of the background region, and once for the region marked blue, which is the expected cavity ringdown and the background. The correspondingly coloured lines show the acquired fits. As can clearly be seen, the two regions cannot be described by the same exponential decay. For the reasons discussed, only the second fit is used, which then yields:

$$\tau = (0.52 \pm 0.03)\,\mu\text{s} \qquad R_\text{M} = (99.975 \pm 00.002)\,\% \qquad \mathcal{F} = (12800 \pm 700)\,. \tag{3.14}$$

The error of τ is the standard error, which is returned by the fitting software (*Mathematica*, `NonlinearModelFit`). For R_M and $\mathcal{F}$ they are derived by Gaussian error propagation. The result is in good agreement with the specified reflectivity of the mirrors.

Under optimal conditions, it was possible to couple around 20 % of an estimated 43 mW beam (taking into account the vacuum window) into the cavity. Using equation (3.7), this results in a maximum energy density of $\rho = 13.4\,\mathrm{J\,m^{-3}}$ (corresponding to an intensity of $0.4\,\mathrm{MW\,cm^{-2}}$) for the fundamental mode with a waist of $w_0 = 104\,\mu\mathrm{m}$.

3.4.2. Stability of the frequency stabilisation during valve shots

An important requirement for the frequency stabilisation is a good–quality reflection signal from the resonator. This is shown in figure 3.14 on the left side. The blue line shows the signal from the cavity, as measured with PD1. A yellow line shows the PDH error signal used for the stabilisation loop, which is calculated internally by the Digilock from the reflection signal and the applied modulation. Based on this, the parameters of the PID controllers can be optimised in order to lock the laser. From the signal in figure 3.14 it is clear that it is far from optimal. This is due to a malfunctioning DAC in the Digilock at the time of the measurement, which introduced artificial noise into the locking circuit. Since this had to be replaced by the manufacturer, which would have taken too much time, the measurements had to be performed in this suboptimal setting. Nevertheless, for the photodetachment spectroscopy it is important that the stabilisation is robust against the operation of the experiment in the time window of the pulses. If this is achieved, fluctuations on a longer timescale can be removed by performing a postselection. Even with the hardware problems of the Digilock, the results below show the functionality of the resonator to this degree.

To verify the stability, the setup was operated under the usual conditions for C_2^- production. The cavity was locked and the SSEV and DBD pulsed, while monitoring the cavity transmission signal and collecting the anion current on the FC. The results of this are shown on the right side of figure 3.14. The red trace in the upper plot shows the transmission signal of the locked cavity. As a reference, the blue trace shows the same with the laser turned off and the green trace a scan over the cavity resonance. The lower plot shows the current signal on the FC, to verify the normal operation of the SSEV and that particles were traversing the resonator. The suppression plate of the FC was biased to 30 V in order to measure only the negative charges. The used gas mixture was 5 % C_2H_2 in neon. As can be seen, there is no influence on the stability of the lock. The long–term stability of the lock was tested as well, but could not be achieved reliably due to the malfunctioning DAC in the Digilock. However, this problem can be easily overcome by a repair of the device and is merely a question of time.

3.5. Experimental results: discussion and summary

The experimental results demonstrated in this chapter show the main functionality of the C_2^- source. Using a hot cathode for stabilisation, the SSEV in combination with the DBD reliably ionises three different gas mixtures containing acetylene. The produced

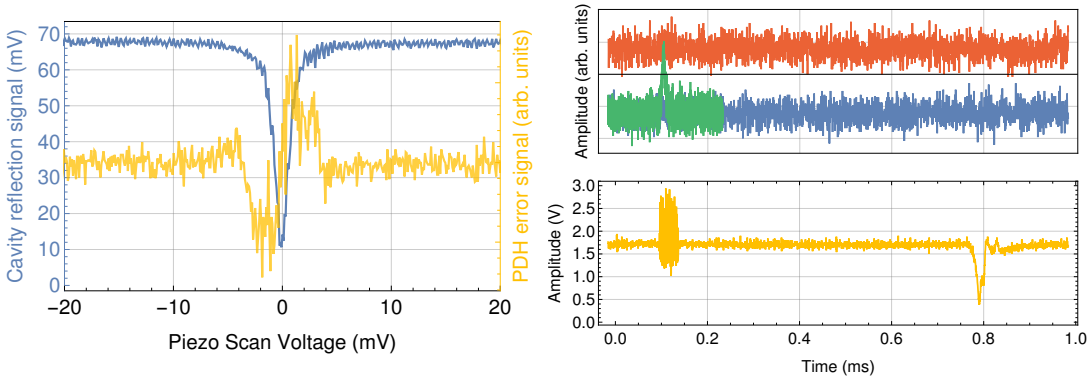

Figure 3.14.: Experimental data showing the frequency stabilisation of the laser to the enhancement cavity. *Left:* plot of a scan over the TEM00 resonance of the cavity, while using the PDH modulation. The blue line shows the reflection signal recorded with PD1 and the yellow line the error signal which is calculated from it. *Right:* stability of the lock during the operation of the SSEV and the DBD. The red trace in the upper plot shows the transmission signal of the locked resonator. The blue trace shows the same with the laser turned off and the green trace a scan over the resonance as reference. The lower plot shows the current on the FC. The latter was recorded simultaneously with the red trace.

particles can be accelerated using a pulsed tube, and the energetic beam steered and manipulated by an einzel lens system. Two functioning and tested detectors are available for diagnostic purposes: a FC for charge measurements and a MCP for beam shape measurements and detection of single particles. A Wien filter allows to record mass spectra of the produced species, by spatially separating particles with different charge–to–mass ratios. It therefore also allows to clean the beam for a specific species. In addition, an enhancement cavity for 399 nm laser light was built. This includes setting up the required optics, diagnostic tools and control electronics for its operation. The cavity was commissioned by showing its stable functionality while the C_2^- source was in use. The enhancement cavity can be used as a basis for photodetachment spectroscopy of the produced anions.

While the main functionality is demonstrated in this thesis, there is still room for improvement of different components. This applies especially to the flux of C_2^- that is currently produced. While it is enough for detection on the MCP, it is too low for a charge measurement with the FC. Even though the maximum repetition rate of the SSEV is quoted with 600 Hz, in the setup it was found to be limited to 20 Hz. This is due to a pressure build up in the first chamber, and the fact that the DBD cannot be operated above 1×10^{-4} mbar. Together with the rough estimate on the number of C_2^- per shot, given in section 3.3, this results in a flux on the order of $\sim 1 \times 10^3\,\mathrm{s}^{-1}$. This would fall short of the $\sim 1 \times 10^4\,\mathrm{s}^{-1}$ which is required to load the Penning trap for

sympathetic cooling of antiprotons in AE$\bar{g}$IS (see introduction to chapter 3).

There are two straightforward improvements that could be implemented to improve the flux. Firstly, the pumping capacity in the valve chamber could be increased. This could be done by enlarging the chamber diameter and installing additional turbo molecular pumps. Doing so would allow to run the SSEV at a higher repetition rate and, given the maximum rating of 600 Hz, possibly increase the flux by an order of magnitude by itself. Secondly, the geometry of the einzel lens system could be optimised. At the moment there is a gap between the last acceleration electrode and the first einzel lens, which allows the beam to expand and makes it harder to collimate. By minimising this gap the collimation could be enhanced, possibly to the extent of making the irises superfluous. This effect was already seen in a temporary test during the commissioning of the source. Given that the irises are currently clipping more than 90 % of the beam, this could again increase the flux by an order of magnitude.

Another straightforward improvement would benefit the resolution of the mass filter. While the masses 24 u and 25 u can be distinguished, there is still a significant overlap between them. This would lead to impurities in the trap during the sympathetic cooling, which would decrease its efficiency. There are again two measures which could be taken to increase the resolution. The first depends on the degree to which the collimation and flux of the beam can be improved by the measures discussed before. But given a stronger C_2^- signal, this would facilitate the optimisation of the electric field inside the filter by tuning the voltages on the shims. The second possible improvement of the resolution would be a variable mount of the Wien filter. As was discussed in 3.3, the filter has a tilt with respect to the vacuum chamber, which requires the use of the einzel lenses and its vertical deflection to compensate for this defect. In combination with the irises, imperfections in the mounting are likely to lead to aberrations if a tilt remains. Mounting the filter on a variable stage and using bellows for the connection to the other chambers, would allow to mechanically counteract the tilt. Given a quoted resolution of $M/\Delta M = 400$ for the device, there is clearly room for improvement.

This page is actually not completely blank.

4. Conclusion and outlook

The topics of this thesis describe the effort that was made towards laser cooling of anions, with the goal to use them as a sympathetic coolant for antiprotons. It covers a theoretical analysis of the requirements and the expected performance of different cooling schemes, as well as a report on the efforts made towards an experimental realisation. While both parts were summarised and discussed in their own respective sections (see. 2.6 and 3.5), a conclusion with a focus on the practical implications is drawn here and an outlook on the next steps is presented.

From the analysis of the cooling schemes in chapter 2 it becomes clear that their experimental realisation is a challenging task with stringent requirements. It is therefore practical to proceed in smaller steps and master the different ingredients for the final goal one by one. As an intermediate goal, it was therefore decided to work towards laser cooled C_2^- in a Paul trap. While this excludes the possibility of sympathetic antiproton cooling, due to the mass selectivity of the trap, it eases the requirements on the realisation. As discussed in sections 2.3 and 2.6, the absence of a magnetic field significantly eases the repumping needed for laser cooling. It also enables the use of the photodetachment cooling method, since the hot electrons naturally leave the trap. Concerning the experimental realisation, it has the added advantage that the radial optical access is easier to implement. As can be seen in figure 3.1, the use of a Paul trap is already foreseen in the setup. To this end, the third segmented einzel lens and the beam bender allow to deflect the mass–filtered beam towards the trap. The commissioning of the 399 nm laser enhancement cavity, which was discussed in 3.1.5 and 3.4, was done with the parallel intent of using it in the Paul trap.

These topics are also the subjects of the next steps of the anion cooling project. As discussed in 3.5, there are several improvements to the C_2^- source that present themselves for implementation. In parallel, the commissioning of the Paul trap is the next major goal. Another important task will then be the characterisation of the initial electronic population of the produced C_2^-. This can either be done by flyby spectroscopy in the valve chamber, using the enhancement cavity described in this thesis, or by spectroscopy on confined C_2^- in the Paul trap. The commissioning of the 2.54 µm laser system needed for this is currently in its final stages.

The medium–term goal is then laser cooling of C_2^- in the Paul trap. Among the methods discussed in 2.6, photodetachment cooling appears most suitable for this task. While Doppler cooling on the $X^2\Sigma(v'' = 0) \leftrightarrow A^2\Pi(v' = 0)$ transition and Sisyphus cooling on the basis of the optical dipole force could also be applied, the heating rates in a room temperature trap are likely to make this challenging. Even though showing strong cooling in the simulation, the Sisyphus method on the basis of a magnetic field gradient would have different requirements in a Paul trap than in a Penning trap. It

is therefore less appealing, given the long–term goal of implementing the cooling in a Penning trap.

The final step, sympathetic antiproton cooling in the Penning trap of the AE$\bar{g}$IS experiment, will then require attaching the source to the apparatus at the AD. Depending on the cooling scheme that is chosen, the electrode geometry of the Penning trap might have to be altered, to allow for e.g. radial access for the optical dipole force cooling. In addition, the laser system will have to be extended, to cope with the level splitting in the magnetic field. To conclude, it can be said that the chosen goal still requires several steps for successful implementation. So far however, there are no principle roadblocks which cannot be overcome by taking the appropriate technical measures.

A. Appendix

A.1. Conventional notation used for molecular spectroscopy

Quantum numbers to denote specific molecular energy levels usually follow a certain convention in the literature. This is summarised here (Lefebvre-Brion and Field, 2004).

- Total nuclear spin ..... $\mathbf{I} = \mathbf{I}_\mathrm{A} + \mathbf{I}_\mathrm{B}$
- Total electron spin ..... $\mathbf{S} = \sum_i \mathbf{s}_i$
- Total electronic orbital angular momentum ..... $\mathbf{L} = \sum_i \mathbf{l}_i$
- Projection of $\mathbf{L}$ on the molecular axis of diatomic molecules ..... Λ
- Rotational angular momentum ..... $\mathbf{R}$
- Total angular momentum ..... $\mathbf{F} = \mathbf{L} + \mathbf{R} + \mathbf{S} + \mathbf{I}$
- Total angular momentum excluding nuclear spin ..... $\mathbf{J} = \mathbf{L} + \mathbf{R} + \mathbf{S}$
- Total angular momentum excluding nuclear and electron spin ..... $\mathbf{N} = \mathbf{L} + \mathbf{R}$

A.2. Hamiltonian of a single particle in a Penning trap in a rotating frame of reference

The Lagrangian of a single particle with charge q in electric and magnetic fields is given by:

$$\mathcal{L} = \frac{m}{2}\dot{\mathbf{r}}^2 - q\Phi(\mathbf{r}, t) + q\dot{\mathbf{r}} \cdot \mathbf{A}(\mathbf{r}, t). \tag{A.1}$$

The transition to a rotating frame defined by $\mathbf{\Omega}$ can be done by applying the transformation (Landau and Lifshitz, 1976, §39; Thyagaraja and McClements, 2009)

$$\mathbf{r} \to \mathbf{R} \qquad \dot{\mathbf{r}} \to \dot{\mathbf{R}} - \mathbf{\Omega} \times \mathbf{R}, \tag{A.2}$$

where $\mathbf{\Omega}$ defines the axis and frequency of rotation. The particle coordinates and velocity in the laboratory are denoted by $\mathbf{r}$, $\dot{\mathbf{r}}$ and in the rotating frame by $\mathbf{R}$, $\dot{\mathbf{R}}$. Φ and $\mathbf{A}$ are the electric and magnetic potential in the laboratory frame. Applying these transformations leads to the new Lagrangian:

$$\mathcal{L}_\mathrm{Rot} = \frac{m}{2}\left(\dot{\mathbf{R}} - \mathbf{\Omega} \times \mathbf{R}\right)^2 - q\Phi(\mathbf{R}, t) + q\left(\dot{\mathbf{R}} - \mathbf{\Omega} \times \mathbf{R}\right) \cdot \mathbf{A}(\mathbf{R}, t). \tag{A.3}$$

The geometry of Penning traps is ideally represented in a cylindrical coordinate system:

$$X = R\cos(\Theta) \qquad Y = R\sin(\Theta) \qquad Z = Z, \tag{A.4}$$

in which the vector potential of the axial magnetic field in the Penning trap takes the form:

$$\mathbf{A} = \frac{BR}{2}\begin{pmatrix} -\sin(\Theta) \\ \cos(\Theta) \\ 0 \end{pmatrix} = \frac{BR}{2}\hat{e}_\Theta. \tag{A.5}$$

The rotating frame of interest is then defined by $\mathbf{\Omega} = \omega\hat{e}_z$. Substituting all this in (A.3), after some straightforward algebra, gives:

$$\mathcal{L}_{\mathrm{Rot}} = \frac{m}{2}\left(\dot{R}^2 + R^2\dot{\Theta}^2 + \dot{Z}^2\right) - q\Phi(R,Z,t) + \frac{mR^2}{2}\left(\dot{\Theta}\left(\Omega_c - 2\omega\right) - \omega\left(\Omega_c - \omega\right)\right), \tag{A.6}$$

where the definition of the *cyclotron frequency* $\Omega_c = \frac{qB}{m}$ was used. The Lagrangian leads to the generalised momenta $p_i = \frac{\partial\mathcal{L}}{\partial\dot{q}_i}$ with $\dot{q}_i = \{\dot{R}, \dot{\Theta}, \dot{Z}\}$:

$$p_R = m\dot{R} \qquad p_\Theta = mR^2\left(\frac{\Omega_c}{2} - \omega + \dot{\Theta}\right) \qquad p_Z = m\dot{Z}, \tag{A.7}$$

which in turn can be used to calculate the Hamiltonian $H = \sum_i p_i\dot{q}_i - \mathcal{L}$:

$$H_{\mathrm{Rot}} = \frac{p_R^2}{2m} + \frac{1}{2mR^2}\left(p_\Theta - \frac{BqR^2}{2}\right)^2 + \frac{p_Z^2}{2m} + q\Phi(R,Z,t) + \omega p_\Theta. \tag{A.8}$$

Expressed in the velocity variables $\dot{q}_i$ this becomes:

$$H_{\mathrm{Rot}} = \frac{m}{2}\left(\dot{R}^2 + R^2\dot{\Theta}^2 + \dot{Z}^2\right) + q\Phi(R,Z,t) + \frac{m}{2}\omega R^2\left(\Omega_c - \omega\right). \tag{A.9}$$

A.3. Calibration of the mass spectrum

This section discusses the procedure that was used to calibrate the mass spectrum, using the result of the 5 % C_2H_2, 3 % CO_2 in helium gas mixture as an example. Figure A.1 shows the implicit mass spectrum, as recorded by ramping the current of the mass filter magnet. The density of measurements was varied to account for the quadratic relationship between current and mass and to achieve a finer resolution of the interesting regions. As discussed in section 3.3, a straight forward transformation using equation (3.12) leads to a spectrum showing unphysical mass signals. This is shown by the red markers in figure A.2 for the interesting regions of the spectrum. The approach for calibration is to use the knowledge about the gas content to determine two signals, which are then used as a reference.

Assuming a modest shift of the spectrum, it is suggestive to interpret the first two signals as H^- and C^-, which are the lightest anions that can be produced from the source

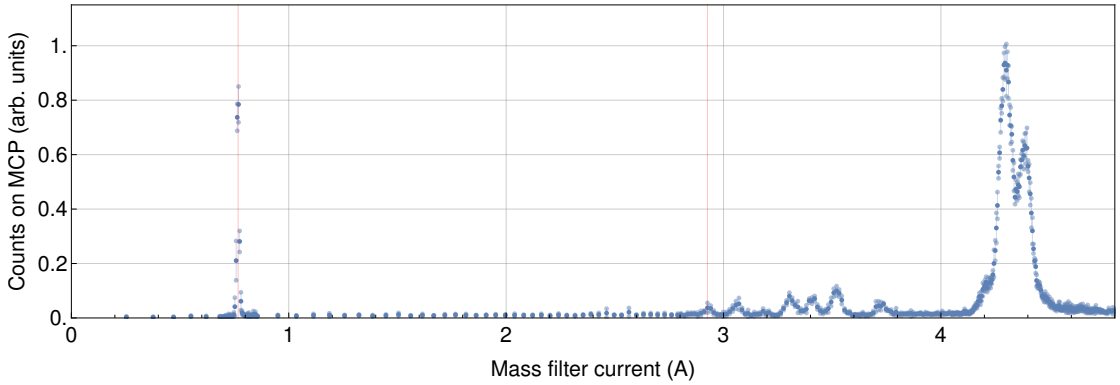

Figure A.1.: Implicit mass spectrum for the 5 % C_2H_2, 3 % CO_2 in helium gas mixture, as recorded by ramping the current of the mass filter magnet. Two vertical red lines mark the signals, which were used for the calibration of the spectrum.

gas. To correct for the shift, it is assumed that its dominant origin can be accounted for by two additional terms α, β in the transformation:

$$m = 2eU_{\mathrm{acc}} \left(\frac{d_{\mathrm{el}} B \left(I_{\mathrm{coil}} + \alpha \right)}{U_{\mathrm{el}} + \beta} \right)^2 . \tag{A.10}$$

Comparing with the original transformation (3.12) shows this to be the same as using a new effective mass filter magnet current $I_{\mathrm{eff}} = I_{\mathrm{coil}} + \alpha$ and deflection voltage $U_{\mathrm{eff}} = U_{\mathrm{el}} + \beta$. The parameters α and β are then determined by fitting (A.10) to the value pairs $(I_{\mathrm{H}^-}, 1\,\mathrm{u})$ and $(I_{\mathrm{C}^-}, 12\,\mathrm{u})$, which define the centre and FWHM currents of the signals. This was done using a nonlinear model fit in *Mathematica*.

The resulting values of α and β for the different gas mixtures are on the order of $\sim 100\,\mathrm{mA}$ and $\sim -20\,\mathrm{V}$ for the different gas mixtures. While the procedure for the calibration was the same for all three gases, due to the weak signal strength, the 1 u and 13 u peaks were used for the other two mixtures. As a crosscheck, the calibration was performed under varying assumptions, with the second signal at 11 u and 13 u. Both cases lead to inconsistent spectra, with signals appearing at fractions of an atomic mass, which is further support for the validity of the calibration.

A.4. Detection efficiency of the MCP

Figure A.3 shows a table of the MCP detection efficiencies for varies radiation types. The table is reproduced from the technical information sheet as received from the customer support. The document can also be found via the link given in the reference (HAMAMATSU PHOTONICS K.K., 2018).

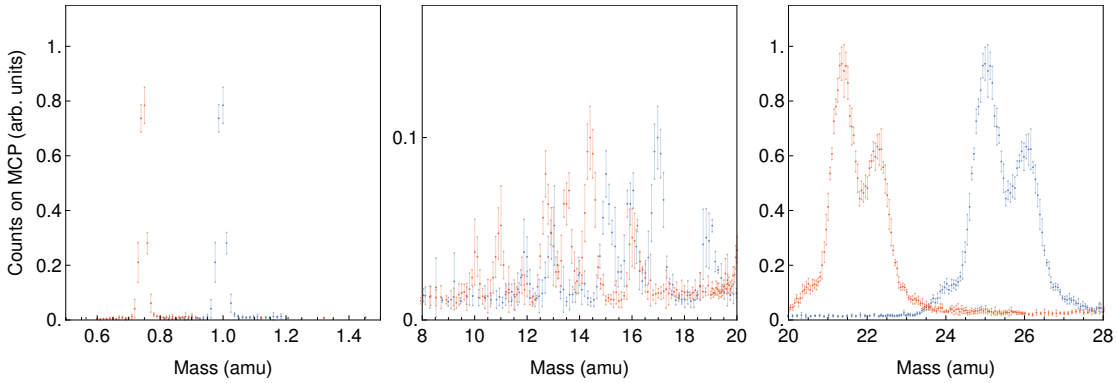

Figure A.2.: Plots of the interesting regions of the mass spectrum after transformation of the x–axis. The red markers show the spectrum without calibration using the relationship from equation (3.12). The blue markers show the spectrum after the calibration is applied.

Types of Radiation	Energy or Wavelength	Detection Efficiency (%)
Electron	0.2 keV to 2 keV	50 to 85
	2 keV to 50 keV	10 to 60
Ion (H^+, He^+, Ar^+)	0.5 keV to 2 keV	5 to 58
	2 keV to 50 keV	60 to 85
	50 keV to 200 keV	4 to 60
UV	300 Å to 1100 Å	5 to 15
	1100 Å to 1500 Å	1 to 5
Soft X-ray	2 Å to 50 Å	5 to 15
Hard X-ray	0.12 Å to 0.2 Å	to 1
High energy particle (ρ, π)	1 GeV to 10 GeV	to 95
Neutron	2.5 MeV to 14 MeV	0.14 to 0.64

Figure A.3.: Detection efficiency of the MCP. Taken from (HAMAMATSU PHOTONICS K.K., 2018).

A.5. Zusammenfassung (Abstract in German)

Das Thema dieser Dissertation ist die Laserkühlung von molekularen Anionen mit dem Ziel, diese für die sympathetische Kühlung von Antiprotonen in einer Penning–Falle einzusetzen. Sie beinhaltet sowohl eine theoretische Analyse der Eignung von verschiedenen Kühlmethoden als auch einen Bericht über die Fortschritte, welche in Richtung einer experimentellen Realisierung gemacht wurden. Der Fokus liegt auf der molekularen Spezies C_2^-, welche in einer kürzlich durchgeführten Studie als Vorteilhafteste einer Reihe von Kandidaten ausgemacht wurde. Das Thema der Laserkühlung von anionischen Molekülen gewinnt auch dadurch an Brisanz, dass das Kühlen von atomaren Anionen bisher nicht erfolgreich war, obwohl es Bestrebungen in diese Richtung gibt (Yzombard et al., 2015).

Nach einer generellen Einleitung des Themas werden die grundlegenden Eigenschaften von anionischen Molekülen besprochen, was insbesondere ihre elektronische Struktur betrifft. Diesem folgt eine Behandlung der Interaktion von Licht mit den Übergängen zwischen den elektronischen Zuständen, insoweit diese für die späteren Kapitel von Bedeutung ist. Ein besonderes Augenmerk liegt schließlich auf der elektronischen Struktur von C_2^- und den Übergängen, die für die Laserkühlung von Interesse sind. Dem folgt eine ausführliche, theoretische Untersuchung von verschiedenen Implementierungen der Laserkühlung. Diese Analyse wurde mithilfe von Computersimulationen gemacht, die mit einem GPU–beschleunigten C++ Programm durchgeführt wurden (Van Gorp et al., 2011; Van Gorp and Dupre, 2013). Letzteres wurde speziell für die Simulation von Ladungen in einer Penning–Falle geschrieben und im Rahmen dieser Arbeit um die Interaktion zwischen Teilchen und Laserlicht erweitert. Die Simulationen resultierten in zwei Publikationen (Fesel et al., 2017; Gerber et al., 2018), welche in den Unterkapiteln 2.5.1 und 2.5.2 zu finden sind. Eine Zusammenfassung sowie ein Vergleich der untersuchten Kühlmethoden, findet sich schließlich in Unterkapitel 2.6. Letzteres zielt darauf ab, dem Leser einen Überblick darüber zu verschaffen, welche Herausforderungen bei der experimentellen Realisierung der Laserkühlung von C_2^- zu erwarten sind.

In Kapitel 3 wird schließlich der experimentelle Aufbau für die Bereitstellung von C_2^- beschrieben. Dieser basiert auf einem sogenannten „Supersonic Expansion Valve“, welches in Kombination mit einem „Dielectric Barrier Discharge“ ein Gasgemisch aus Acetylen in einem noblen Trägergas ionisiert. Die produzierten Anionen werden anschließend beschleunigt und mittels eines Wien–Filters die gewünschte Masse ausgewählt. Der verwendete experimentelle Aufbau wird im Detail beschrieben (siehe Abbildung 3.1 für einen Überblick) und die gewonnenen Resultate präsentiert. Letztere inkludieren ein Massenspektrum, welches die erfolgreiche Produktion von Anionen mit einer Masse von 24 u zeigt, welche C_2^- entspricht.

Im experimentellen Aufbau wurde ebenfalls eine Möglichkeit zur Spektroskopie der produzierten Anionen vorgesehen, welche auf die Photoneutralisation von angeregten Anionen ausgelegt ist. Zu diesem Zweck wurde ein optischer Resonator für die Überhöhung der Energiedichte eines 399 nm Lasers gebaut, welcher gleichzeitig durchlässig für Licht mit einer Wellenlänge von 2.54 µm ist, um die resonante Anregung der Anionen zu ermöglichen. Der optische Aufbau zur Stabilisierung des 399 nm Lasers auf den

Resonator wird beschrieben (siehe Abbildung 3.6 für einen Überblick), gefolgt von einer Diskussion der experimentellen Resultate. Letztere inkludieren eine Bestimmung des Gütefaktors des Resonators auf $\mathcal{F} = (12800 \pm 700)$ und eine Überprüfung der Robustheit der Stabilisierung während des Betriebs der C_2^- Quelle. Zu guter Letzt findet in Kapitel 4 eine übergreifende Diskussion der besprochenen Inhalte statt und es wird ein Ausblick auf die zukünftig notwendige Arbeit gegeben.

A.6. Curriculum vitae

Julian Valentin Fesel

MSc

Personal information

Date of birth 10.06.1989
Nationality Austria

Education

11/2014 – today **Doctoral studies of Physics**, *CERN in affiliation with the University of Vienna*, Geneva/Vienna.
Thesis in applied physics on the development of an anionic cooling bath for antiprotons. Affiliation with the AEgIS experiment at CERN.
Supervisors: Dr. Michael Doser (CERN) and Univ.-Prof. Dr. Markus Aspelmeyer (University of Vienna).
Expected to finish: Spring 2019

10/2012 – 11/2014 **Master's studies of Physics**, *University of Vienna, Faculty of Physics*, Vienna.
Thesis title: Master's thesis on optical levitation of nano spheres.
Supervisor: Univ.-Prof. Dr. Markus Aspelmeyer.
Graduation with distinction.

10/2009 – 10/2012 **Bachelor's studies of Physics**, *University of Vienna, Faculty of Physics*, Vienna.
Bachelor's thesis: "The EPR–Paradox and the Bell–Inequality"
Graduation with distinction.

09/2001 – 07/2008 **Secondary School**, *Akademisches Gymnasium and Bundesgymnasium Seekirchen*, Salzburg.
Graduation with distinction.

Work experience

2014 (6 months) **Research assistant in the group of Prof. Aspelmeyer**, *University of Vienna.*

2014 (4 months) **Tutor for "Theoretical Quantum Mechanics 1"**, *University of Vienna.*

12/2008-07/2009 (9 months) **Emergency medical technician**, *Red Cross*, Salzburg.
Civilian service as an EMT for the rescue service in Salzburg.

Publications

2018 S. Gerber, J. Fesel, M. Doser and D. Comparat, *Photodetachment and Doppler laser cooling of anionic molecules,* New J. Phys., 20, 23024 (2018), `http://stacks.iop.org/1367-2630/20/i=2/a=023024`

2017 J. Fesel, S. Gerber, M. Doser and D. Comparat, *Optical dipole-force cooling of anions in a Penning trap,* Phys. Rev. A, 96, 31401 (2017), `https://link.aps.org/doi/10.1103/PhysRevA.96.031401`

2016 D. Grass, J. Fesel, S. G. Hofer, N. Kiesel and M. Aspelmeyer, *Optical trapping and control of nanoparticles inside evacuated hollow core photonic crystal fibers,* Appl. Phys. Lett., 108, 221103 (2016), `http://dx.doi.org/10.1063/1.4953025`

Conference presentations

03/2018 **Low energy antiproton physics (LEAP)**, *Paris*, Title: Laser cooled anions as a sympathetic coolant for antiprotons.

08/2017 **Joint Annual Meeting of SPS and ÖPG**, *Geneva*, Title: Laser cooled anions as a sympathetic coolant.

06/2017 **APS, Division of Atomic, Molecular, and Optical Physics (DAMOP)**, *Sacramento*, Title: Laser cooled anions as a sympathetic coolant.

09/2016 **Annual Meeting of the ÖPG**, *Vienna*, Title: Laser cooled anions as a sympathetic coolant.

Grants and distinctions

2018 Dissertation Completion Fellowship, *University of Vienna*

2014 Stipend of the Austrian doctoral student program at CERN, *Geneva*

2013 Gifted student award, *University of Vienna*

2010 Gifted student award, *University of Vienna*

Glossary

AD antiproton decelerator 9, 10, 56, 80

ADC analogue–to–digital converter 59, 65, 66

AEgIS antihydrogen experiment: gravity, interferometry, spectroscopy 9, 10, 11, 51, 76, 80

ALPHA antihydrogen laser physics apparatus 9

AOM acousto–optic modulator 73

APP anamorphic prism pair 64

ASACUSA atomic spectroscopy and collisions using slow antiprotons 9

BASE baryon antibaryon symmetry experiment 9

BS beam splitter 64

CCD charge–coupled device 64

CERN conseil européen pour la recherche nucléaire 9, 48, 50, 51

CP charge–parity 9

CPT charge–parity–time 9

DAC digital–to–analogue converter 65, 75

DBD dielectric barrier discharge 3, 7, 52, 53, 58, 65, 66, 71, 72, 73, 75, 76

EA electron affinity 21, 49, 50, 59

ELENA extra low energy antiproton (ring) 9

FC Faraday cup 52, 53, 59, 65, 66, 67, 66, 69, 72, 75, 76

FPGA field–programmable gate array 52, 59, 65

FSR free spectral range 62, 73

FWHM full width half maximum 20, 62, 73, 82

GBAR gravitational behaviour of antihydrogen at rest 9, 10

GPU graphics processing unit 3, 85

LHC Large Hadron Collider 9

MCP multi channel plate 52, 56, 59, 61, 67, 69, 70, 72, 75, 76, 83

P parity 9

PBS polarising beam splitter 64

PCB printed circuit board 58

PD photodiode 64, 65, 73, 75

PDH Pound–Drever–Hall 63, 65, 75

PID proportional–integral–derivative 65, 75

RCE resonant charge exchange 10

SSEV supersonic expansion valve 3, 51, 52, 53, 56, 58, 65, 66, 72, 73, 75, 76, 77

TBR three–body recombination 10

TTL transistor–transistor logic 53

USB universal serial bus 64

WEP weak equivalence principle 9

Bibliography

Aghion, S., C. Amsler, G. Bonomi, R. S. Brusa, M. Caccia, R. Caravita, F. Castelli, G. Cerchiari, D. Comparat, G. Consolati, A. Demetrio, L. Di Noto, M. Doser, C. Evans, M. Fanì, R. Ferragut, J. Fesel, A. Fontana, S. Gerber, M. Giammarchi, A. Gligorova, F. Guatieri, S. Haider, A. Hinterberger, H. Holmestad, A. Kellerbauer, O. Khalidova, D. Krasnický, V. Lagomarsino, P. Lansonneur, P. Lebrun, C. Malbrunot, S. Mariazzi, J. Marton, V. Matveev, Z. Mazzotta, S. R. Müller, G. Nebbia, P. Nedelec, M. Oberthaler, N. Pacifico, D. Pagano, L. Penasa, V. Petracek, F. Prelz, M. Prevedelli, B. Rienäcker, J. Robert, O. M. Røhne, A. Rotondi, H. Sandaker, R. Santoro, L. Smestad, F. Sorrentino, G. Testera, I. C. Tietje, E. Widmann, P. Yzombard, C. Zimmer, J. Zmeskal, N. Zurlo, and M. Antonello (2018). "Compression of a mixed antiproton and electron non–neutral plasma to high densities". In: *The European Physical Journal D* 72, p. 76. DOI: 10.1140/epjd/e2018-80617-x.

Ahmadi, M., B. X. R. Alves, C. J. Baker, W. Bertsche, A. Capra, C. Carruth, C. L. Cesar, M. Charlton, S. Cohen, R. Collister, S. Eriksson, A. Evans, N. Evetts, J. Fajans, T. Friesen, M. C. Fujiwara, D. R. Gill, J. S. Hangst, W. N. Hardy, M. E. Hayden, E. D. Hunter, C. A. Isaac, M. A. Johnson, J. M. Jones, S. A. Jones, S. Jonsell, A. Khramov, P. Knapp, L. Kurchaninov, N. Madsen, D. Maxwell, J. T. K. McKenna, S. Menary, J. M. Michan, T. Momose, J. J. Munich, K. Olchanski, A. Olin, P. Pusa, C. Ø. Rasmussen, F. Robicheaux, R. L. Sacramento, M. Sameed, E. Sarid, D. M. Silveira, D. M. Starko, G. Stutter, C. So, T. D. Tharp, R. I. Thompson, D. P. van der Werf, and J. S. Wurtele (2018a). "Observation of the 1S–2P Lyman–α transition in antihydrogen". In: *Nature* 561, pp. 211–215. DOI: 10.1038/s41586-018-0435-1.

Ahmadi, M., B. X. R. Alves, C. J. Baker, W. Bertsche, A. Capra, C. Carruth, C. L. Cesar, M. Charlton, S. Cohen, R. Collister, S. Eriksson, A. Evans, N. Evetts, J. Fajans, T. Friesen, M. C. Fujiwara, D. R. Gill, J. S. Hangst, W. N. Hardy, M. E. Hayden, C. A. Isaac, M. A. Johnson, J. M. Jones, S. A. Jones, S. Jonsell, A. Khramov, P. Knapp, L. Kurchaninov, N. Madsen, D. Maxwell, J. T. K. McKenna, S. Menary, T. Momose, J. J. Munich, K. Olchanski, A. Olin, P. Pusa, C. Ø. Rasmussen, F. Robicheaux, R. L. Sacramento, M. Sameed, E. Sarid, D. M. Silveira, G. Stutter, C. So, T. D. Tharp, R. I. Thompson, D. P. van der Werf, and J. S. Wurtele (2018b). "Characterization of the 1S–2S transition in antihydrogen". In: *Nature* 557, pp. 71–75. DOI: 10.1038/s41586-018-0017-2.

Amoretti, M., C. Amsler, G. Bonomi, A. Bouchta, P. Bowe, C. Carraro, C. L. Cesar, M. Charlton, M. J. T. Collier, M. Doser, V. Filippini, K. S. Fine, A. Fontana, M. C. Fujiwara, R. Funakoshi, P. Genova, J. S. Hangst, R. S. Hayano, M. H. Holzscheiter, L. V. Jørgensen, V. Lagomarsino, R. Landua, D. Lindelöf, E. L. Rizzini, M. Macrì, N. Madsen, G. Manuzio, M. Marchesotti, P. Montagna, H. Pruys, C. Regenfus, P.

Riedler, J. Rochet, A. Rotondi, G. Rouleau, G. Testera, A. Variola, T. L. Watson, and D. P. van der Werf (2002). "Production and detection of cold antihydrogen atoms". In: *Nature* 419, pp. 456–459. DOI: 10.1038/nature01096.

An, K., C. Yang, R. R. Dasari, and M. S. Feld (1995). "Cavity ring–down technique and its application to the measurement of ultraslow velocities". In: *Optics Letters* 20.9, pp. 1068–1070. DOI: 10.1364/OL.20.001068.

Andreev, S. V., V. I. Balykin, V. S. Letekhov, and V. G. Minogin (1981). "Radiative slowing and reduction of the energy spread of sodium atoms to 1.5 K in an oppositely directed laser beam". In: *Journal of Experimental and Theoretical Physics Letters* 34.8, pp. 442–445. URL: http://www.jetpletters.ac.ru/ps/1520/article_23237.shtml.

Andresen, G. B., M. D. Ashkezari, M. Baquero-Ruiz, W. Bertsche, P. D. Bowe, E. Butler, C. L. Cesar, S. Chapman, M. Charlton, J. Fajans, T. Friesen, M. C. Fujiwara, D. R. Gill, J. S. Hangst, W. N. Hardy, R. S. Hayano, M. E. Hayden, A. Humphries, R. Hydomako, S. Jonsell, L. Kurchaninov, R. Lambo, N. Madsen, S. Menary, P. Nolan, K. Olchanski, A. Olin, A. Povilus, P. Pusa, F. Robicheaux, E. Sarid, D. M. Silveira, C. So, J. W. Storey, R. I. Thompson, D. P. Van Der Werf, D. Wilding, J. S. Wurtele, and Y. Yamazaki (2010). "Evaporative Cooling of Antiprotons to Cryogenic Temperatures". In: *Physical Review Letters* 105.1, p. 013003. DOI: 10.1103/PhysRevLett.105.013003.

Andresen, G. B., M. D. Ashkezari, M. Baquero-Ruiz, W. Bertsche, P. D. Bowe, E. Butler, C. L. Cesar, M. Charlton, A. Deller, S. Eriksson, J. Fajans, T. Friesen, M. C. Fujiwara, D. R. Gill, A. Gutierrez, J. S. Hangst, W. N. Hardy, R. S. Hayano, M. E. Hayden, a. J. Humphries, R. Hydomako, S. Jonsell, S. L. Kemp, L. Kurchaninov, N. Madsen, S. Menary, P. Nolan, K. Olchanski, A. Olin, P. Pusa, C. Ø. Rasmussen, F. Robicheaux, E. Sarid, D. M. Silveira, C. So, J. W. Storey, R. I. Thompson, D. P. van der Werf, J. S. Wurtele, and Y. Yamazaki (2011). "Confinement of antihydrogen for 1,000 seconds". In: *Nature Physics* 7, pp. 558–564. DOI: 10.1038/nphys2025.

Bartmann, W., P. Belochitskii, H. Breuker, F. Butin, C. Carli, T. Eriksson, W. Oelert, R. Ostojic, S. Pasinelli, and G. Tranquille (2018). "The ELENA facility". In: *Philosophical Transactions of the Royal Society A* 376, p. 20170266. DOI: 10.1098/rsta.2017.0266.

Bartmess, J. (2018). *NIST Chemistry WebBook, NIST Standard Reference Database Number 69*. Ed. by P. Linstrom and W. Mallard. Gaithersburg MD, 20899: National Institute of Standards and Technology. DOI: 10.18434/T4D303.

Beer, E. de, Y. Zhao, I. Yourshaw, and D. M. Neumark (1995). "Stimulated Raman pumping of C_2^- probed via resonant two–photon detachment". In: *Chemical Physics Letters* 244.5, pp. 400–406. DOI: 10.1016/0009-2614(95)00967-9.

Bersch, C. (2014). *pst-optexp package for LaTeX*. URL: https://www.ctan.org/tex-archive/graphics/pstricks/contrib/pst-optexp (visited on 12/02/2018).

Bertsche, W. A. (2018). "Prospects for comparison of matter and antimatter gravitation with ALPHA–g". In: *Philosophical Transactions of the Royal Society A* 376, p. 20170265. DOI: 10.1098/rsta.2017.0265.

Bertsche, W. A., E. Butler, M. Charlton, and N. Madsen (2014). "Physics with antihydrogen". In: *Journal of Physics B: Atomic, Molecular and Optical Physics* 48.23, p. 232001. DOI: 10.1088/0953-4075/48/23/232001.

Bilodeau, R. C. and H. K. Haugen (2000). "Experimental Studies of Os^-: Observation of a Bound–Bound Electric Dipole Transition in an Atomic Negative Ion". In: *Physical Review Letters* 85.3, pp. 534–537. DOI: 10.1103/PhysRevLett.85.534.

Black, E. D. (2001). "An introduction to Pound–Drever–Hall laser frequency stabilization". In: *American Journal of Physics* 69.1, p. 79. DOI: 10.1119/1.1286663.

Blondel, C., W. Chaibi, C. Delsart, C. Drag, F. Goldfarb, and S. Kröger (2005). "The electron affinities of O, Si, and S revisited with the photodetachment microscope". In: *The European Physical Journal D* 33.3, pp. 335–342. DOI: 10.1140/epjd/e2005-00069-9.

Blondel, C., C. Delsart, and F. Goldfarb (2001). "Electron spectrometry at the μeV level and the electron affinities of Si and F". In: *Journal of Physics B: Atomic, Molecular and Optical Physics* 34.9, pp. L281–L288. DOI: 10.1088/0953-4075/34/9/101.

Boldyrev, A. I. and J. Simons (1993). "Theoretical search for small linear doubly charged anions". In: *The Journal of Chemical Physics* 98.6, pp. 4745–4752. DOI: 10.1063/1.464978.

Bragg, A. E., R. Wester, A. V. Davis, A. Kammrath, and D. M. Neumark (2003). "Excited–state detachment dynamics and rotational coherences of C_2^- via time–resolved photoelectron imaging". In: *Chemical Physics Letters* 376.5, pp. 767–775. DOI: 10.1016/S0009-2614(03)01060-1.

Bratsch, S. G. and J. J. Lagowski (1986). "Predicted stabilities of monatomic anions in water and liquid ammonia at 298.15 K". In: *Polyhedron* 5.11, pp. 1763–1770. DOI: 10.1016/S0277-5387(00)84854-8.

Bresteau, D., C. Drag, and C. Blondel (2016). "Isotope shift of the electron affinity of carbon measured by photodetachment microscopy". In: *Physical Review A* 93.1, p. 13414. DOI: 10.1103/PhysRevA.93.013414.

Bruna, P. J. and F. Grein (2000). "Ab initio study of the electron–spin magnetic moments (g–factors) of C_2^-, CSi^-, Si_2^-, LiC_2, NaC_2, and $LiSi_2$". In: *The Journal of Chemical Physics* 112.24, pp. 10796–10805. DOI: 10.1063/1.481723.

Brusa, R. S., C. Amsler, T. Ariga, G. Bonomi, P. Bräunig, L. Cabaret, M. Caccia, R. Caravita, F. Castelli, G. Cerchiari, D. Comparat, G. Consolati, A. Demetrio, L. D. Noto, M. Doser, A. Ereditato, C. Evans, R. Ferragut, J. Fesel, A. Fontana, S. Gerber, M. Giammarchi, A. Gligorova, F. Guatieri, S. Haider, H. Holmestad, T. Huse, A. Kellerbauer, D. Krasnický, V. Lagomarsino, P. Lansonneur, P. Lebrun, C. Malbrunot, S. Mariazzi, V. Matveev, Z. Mazzotta, G. Nebbia, P. Nedelec, M. Oberthaler, N. Pacifico, D. Pagano, L. Penasa, V. Petracek, C. Pistillo, F. Prelz, M. Prevedelli, L. Ravelli, B. Rienäcker, O. M. Røhne, A. Rotondi, M. Sacerdoti, H. Sandaker, R. Santoro, P. Scampoli, L. Smestad, F. Sorrentino, I. M. Strojek, G. Testera, I. C. Tietje, S. Vamosi, E. Widmann, P. Yzombard, J. Zmeskal, and N. Zurlo (2017). "The AEgIS experiment at CERN: measuring antihydrogen free–fall in earth's gravitational field to test WEP with antimatter". In: *Journal of Physics: Conference Series* 791.1, p. 012014. DOI: 10.1088/1742-6596/791/1/012014.

Canetti, L., M. Drewes, and M. Shaposhnikov (2012). "Matter and antimatter in the universe". In: *New Journal of Physics* 14, p. 95012. DOI: 10.1088/1367-2630/14/9/095012.

Cerchiari, G. (2018). "Laser spectroscopy of La^- and anion trapping with a view to laser cooling". PhD thesis. Ruprecht–Karls–Universität, Heidelberg. URL: http://hdl.handle.net/21.11116/0000-0002-A01A-C.

Cerchiari, G., A. Kellerbauer, M. S. Safronova, U. I. Safronova, and P. Yzombard (2018). "Ultracold Anions for High–Precision Antihydrogen Experiments". In: *Physical Review Letters* 120.13, p. 133205. DOI: 10.1103/PhysRevLett.120.133205.

Chen, F. (1984). *Introduction to plasma physics and controlled fusion*. New York: Plenum Press.

Chipman, D. M. (1978). "Effect of Molecular Geometry on the Electron Affinity of Water". In: *The Journal of Physical Chemistry* 82.9, pp. 1080–1083. DOI: 10.1021/j100498a023.

Dalibard, J. and C. Cohen–Tannoudji (1985). "Dressed–Atom approach to atomic motion in laser light: the dipole force revisited". In: *Journal of the Optical Society of America B* 2.11, pp. 1707–1720. DOI: 10.1364/JOSAB.2.001707.

Davidson, R. C. (2001). *Physics of nonneutral plasmas*. 2nd ed. Imperial College Press.

Debu, P. (2012). "GBAR". In: *Hyperfine Interactions* 212.1-3, pp. 51–59. DOI: 10.1007/s10751-011-0379-4.

Demtröder, W. (2016). *Experimentalphysik 3: Atome, Moleküle und Festkörper*. 5th ed. Springer Spektrum. DOI: 10.1007/978-3-662-49094-5.

DeVine, J. A., M. L. Weichman, C. Xie, M. C. Babin, M. A. Johnson, J. Ma, H. Guo, and D. M. Neumark (2018). "Autodetachment from Vibrationally Excited Vinylidene Anions". In: *The Journal of Physical Chemistry Letters* 9, pp. 1058–1063. DOI: 10.1021/acs.jpclett.8b00144.

Doser, M., S. Aghion, C. Amsler, G. Bonomi, R. S. Brusa, M. Caccia, R. Caravita, F. Castelli, G. Cerchiari, D. Comparat, G. Consolati, A. Demetrio, L. Di Noto, C. Evans, M. Fanì, R. Ferragut, J. Fesel, A. Fontana, S. Gerber, M. Giammarchi, A. Gligorova, F. Guatieri, S. Haider, A. Hinterberger, H. Holmestad, A. Kellerbauer, O. Khalidova, D. Krasnický, V. Lagomarsino, P. Lansonneur, P. Lebrun, C. Malbrunot, S. Mariazzi, J. Marton, V. Matveev, Z. Mazzotta, S. R. Müller, G. Nebbia, P. Nedelec, M. Oberthaler, N. Pacifico, D. Pagano, L. Penasa, V. Petracek, F. Prelz, M. Prevedelli, B. Rienäcker, J. Robert, O. M. Røhne, A. Rotondi, H. Sandaker, R. Santoro, L. Smestad, F. Sorrentino, G. Testera, I. C. Tietje, E. Widmann, P. Yzombard, C. Zimmer, J. Zmeskal, and N. Zurlo (2018). "AEgIS at ELENA: outlook for physics with a pulsed cold antihydrogen beam". In: *Philosophical Transactions of the Royal Society A* 376, p. 20170274. DOI: 10.1098/rsta.2017.0274.

Doser, M., C. Amsler, A. Belov, G. Bonomi, P. Bräunig, J. Bremer, R. Brusa, G. Burkhart, L. Cabaret, C. Canali, F. Castelli, K. Chlouba, S. Cialdi, D. Comparat, G. Consolati, L. D. Noto, A. Donzella, A. Dudarev, T. Eisel, R. Ferragut, G. Ferrari, A. Fontana, P. Genova, M. Giammarchi, A. Gligorova, S. Gninenko, S. Haider, J. P. Hansen, S. Hogan, L. Jorgensen, T. Kaltenbacher, A. Kellerbauer, D. Krasnicky, V. Lagomarsino, S. Mariazzi, V. Matveev, F. Merkt, F. Moia, G. Nebbia, P. Nedelec, M.

Oberthaler, D. Perini, V. Petracek, F. Prelz, M. Prevedelli, C. Regenfus, C. Riccardi, O. Rohne, A. Rotondi, M. Sacerdoti, H. Sandaker, M. Spacek, J. Storey, G. Testera, A. Tokareva, D. Trezzi, R. Vaccarone, F. Villa, Z. Zavatarelli, A. Zenoni, and A. Collaboration (2012). "Exploring the WEP with a pulsed cold beam of antihydrogen". In: *Classical and Quantum Gravity* 29.18, p. 184009. DOI: 10.1088/0264-9381/29/18/184009.

Dressler, R. and M. Allan (1987). "A dissociative electron attachment, electron transmission, and electron energy–loss study of the temporary negative ion of acetylene". In: *The Journal of Chemical Physics* 87.8, pp. 4510–4518. DOI: 10.1063/1.452864.

Dubin, D. H. E. and T. M. O'Neil (1999). "Trapped nonneutral plasmas, liquids, and crystals (the thermal equilibrium states)". In: *Reviews of Modern Physics* 71.1, pp. 87–172. DOI: 10.1103/RevModPhys.71.87.

Ellison, G. B., P. C. Engelking, and W. C. Lineberger (1978). "An experimental Determination of the Geometry and Electron Affinity of CH_3". In: *Journal of the American Chemical Society* 100.8, pp. 2556–2558. DOI: 10.1021/ja00476a054.

Ertmer, W., R. Blatt, J. L. Hall, and M. Zhu (1985). "Laser Manipulation of Atomic Beam Velocities: Demonstration of Stopped Atoms and Velocity Reversal". In: *Physical Review Letters* 54.10, pp. 996–999. DOI: 10.1103/PhysRevLett.54.996.

Ervin, K. M., I. Anusiewicz, P. Skurski, J. Simons, and W. C. Lineberger (2003). "The Only Stable State of O_2^- Is the $X\,^2\Pi_g$ Ground State and It (Still!) Has an Adiabatic Electron Detachment Energy of 0.45 eV". In: *The Journal of Physical Chemistry A* 107.41, pp. 8521–8529. DOI: 10.1021/jp0357323.

Ervin, K. M., J. Ho, and W. C. Lineberger (1989). "A study of the singlet and triplet states of vinylidene by photoelectron spectroscopy of $H_2C{=}C^-$, $D_2C{=}C^-$, and $HDC{=}C^-$. Vinylidene–acetylene isomerization". In: *The Journal of Chemical Physics* 91.10, pp. 5974–5992. DOI: 10.1063/1.457415.

Ervin, M. K. and W. C. Lineberger (1991). "Photoelectron spectra of C_2^- and C_2H^-". In: *The Journal of Physical Chemistry* 95.3, pp. 1167–1177. DOI: 10.1021/j100156a026.

Even, U. (2015). "The Even–Lavie valve as a source for high intensity supersonic beam". In: *EPJ Techniques and Instrumentation* 2, p. 17. DOI: 10.1140/epjti/s40485-015-0027-5.

Fajans, J. (2003). "Non–neutral plasma equilibria, trapping, separatrices, and separatrix crossing in magnetic mirrors". In: *Physics of Plasmas* 10.5, pp. 1209–1214. DOI: 10.1063/1.1564820.

Fesel, J., S. Gerber, M. Doser, and D. Comparat (2017). "Optical dipole–force cooling of anions in a Penning trap". In: *Physical Review A* 96.3, p. 31401. DOI: 10.1103/PhysRevA.96.031401.

Foot, C. J. (2005). *Atomic Physics*. 1st ed. New York: Oxford University Press. URL: https://global.oup.com/academic/product/atomic-physics-9780198506959?cc=at&lang=en&#.

Gabrielse, G., N. S. Bowden, P. Oxley, A. Speck, C. H. Storry, J. N. Tan, M. Wessels, D. Grzonka, W. Oelert, G. Schepers, T. Sefzick, J. Walz, H. Pittner, T. W. Hänsch, and E. A. Hessels (2002). "Background–Free Observation of Cold Antihydrogen with

Field–Ionization Analysis of Its States". In: *Physical Review Letters* 89.21, p. 213401. DOI: 10.1103/PhysRevLett.89.213401.

Gerardi, H. K., K. J. Breen, T. L. Guasco, G. H. Weddle, G. H. Gardenier, J. E. Laaser, and M. A. Johnson (2010). "Survey of Ar–Tagged Predissociation and Vibrationally Mediated Photodetachment Spectroscopies of the Vinylidene Anion, $C_2H_2^-$". In: *The Journal of Physical Chemistry A* 114.3, pp. 1592–1601. DOI: 10.1021/jp9095419.

Gerber, S., J. Fesel, M. Doser, and D. Comparat (2018). "Photodetachment and Doppler laser cooling of anionic molecules". In: *New Journal of Physics* 20, p. 023024. DOI: 10.1088/1367-2630/aaa951.

Gomberoff, K., J. Fajans, J. Wurtele, A. Friedman, D. P. Grote, R. H. Cohen, and J.-L. Vay (2007). "Simulation studies of non–neutral plasma equilibria in an electrostatic trap with a magnetic mirror". In: *Physics of Plasmas* 14.5, p. 052107. DOI: 10.1063/1.2727470.

Griffiths, D. (2008). *Introduction to Elementary Particles*. 2nd ed. WILEY–VCH Verlag GmbH & Co. KGaA. DOI: 10.1002/9783527618460.

Grimm, R., M. Weidemüller, and Y. B. Ovchinnikov (2000). "Optical Dipole Traps for Neutral Atoms". In: *Advances in Atomic, Molecular, and Optical Physics* 42, pp. 95–170. DOI: 10.1016/S1049-250X(08)60186-X.

Haken, H. and H. C. Wolf (2006). *Molekülphysik und Quantenchemie*. Springer, Berlin, Heidelberg, pp. 1–535. DOI: 10.1007/3-540-30315-4.

HAMAMATSU PHOTONICS K.K. (2018). *MCP Assembly — Technical Information*. URL: https://www.triumf.ca/sites/default/files/Hamamatsu%20MCP%20guide.pdf (visited on 12/30/2018).

Harris, J. P., D. R. Manship, W. H. Breckenridge, and T. G. Wright (2014). "Comparison of the interactions in the rare gas hydride and Group 2 metal hydride anions". In: *The Journal of Chemical Physics* 140.8, p. 84304. DOI: 10.1063/1.4865749.

Heber, O., R. Golser, H. Gnaser, D. Berkovits, Y. Toker, M. Eritt, M. L. Rappaport, and D. Zajfman (2006). "Lifetimes of the negative molecular hydrogen ions: H_2^-, D_2^-, and HD^-". In: *Physical Review A* 73.6, p. 60501. DOI: 10.1103/PhysRevA.73.060501.

Hodgson, N. and H. Weber (2005). *Laser resonators and beam propagation : fundamentals, advanced concepts and applications*. 2nd ed. New York: Springer-Verlag Berlin Heidelberg, p. 796. DOI: 10.1007/b106789.

Honig, R. E. (1954). "Mass Spectrometric Study of the Molecular Sublimation of Graphite". In: *The Journal of Chemical Physics* 22.1, pp. 126–131. DOI: 10.1063/1.1739819.

Höppner, R., E. Roldán, and G. J. de Valcárcel (2012). "A semiclassical optics derivation of Einstein's rate equations". In: *American Journal of Physics* 80.10, p. 882. DOI: 10.1119/1.4740247.

Hori, M., H. Aghai-Khozani, A. Sótér, D. Barna, A. Dax, R. Hayano, T. Kobayashi, Y. Murakami, K. Todoroki, H. Yamada, D. Horváth, and L. Venturelli (2016). "Buffer–gas cooling of antiprotonic helium to 1.5 to 1.7 K, and antiproton–to–electron mass ratio". In: *Science* 354.6312, pp. 610–614. DOI: 10.1126/science.aaf6702.

Hori, M. and J. Walz (2013). "Physics at CERN's Antiproton Decelerator". In: *Progress in Particle and Nuclear Physics* 72, pp. 206–253. DOI: 10.1016/j.ppnp.2013.02.004.

Hummon, M. T., M. Yeo, B. K. Stuhl, A. L. Collopy, Y. Xia, and J. Ye (2013). "2D Magneto–Optical Trapping of Diatomic Molecules". In: *Physical Review Letters* 110.14, p. 143001. DOI: 10.1103/PhysRevLett.110.143001.

Jenč, F. (1996). "The reduced potential curve (RPC) method and its applications". In: *International Reviews in Physical Chemistry* 15.2, pp. 467–523. DOI: 10.1080/01442359609353191.

Johnson, M. A., M. L. Alexander, and W. C. Lineberger (1984). "Photodestruction cross sections for mass-selected ion clusters: $(CO_2)_n^+$". In: *Chemical Physics Letters* 112.4, pp. 285–290. DOI: 10.1016/0009-2614(84)85742-5.

Jones, P. L., R. D. Mead, B. E. Kohler, S. D. Rosner, and W. C. Lineberger (1980). "Photodetachment spectroscopy of C_2^- autodetaching resonances". In: *Journal of Chemical Physics* 73.9, pp. 4419–4432. DOI: 10.1063/1.440678.

Jordan, E., G. Cerchiari, S. Fritzsche, and A. Kellerbauer (2015). "High–Resolution Spectroscopy on the Laser–Cooling Candidate La^-". In: *Physical Review Letters* 115.11, p. 113001. DOI: 10.1103/PhysRevLett.115.113001.

Jordan, J. E. (2015). "High–resolution Doppler laser spectroscopy of the laser cooling candidate La^-". PhD thesis. Ruprecht–Karls–Universität, Heidelberg. URL: http://hdl.handle.net/11858/00-001M-0000-0029-4D2F-B.

Kasdan, A., E. Herbst, and W. C. Lineberger (1975). "Laser photoelectron spectrometry of CH^-". In: *Chemical Physics Letters* 31.1, pp. 78–82. DOI: 10.1016/0009-2614(75)80062-5.

Kellerbauer, A., S. Aghion, C. Amsler, A. Ariga, T. Ariga, G. Bonomi, P. Bräunig, J. Bremer, R. S. Brusa, L. Cabaret, M. Caccia, R. Caravita, F. Castelli, G. Cerchiari, K. Chlouba, S. Cialdi, D. Comparat, G. Consolati, A. Demetrio, L. Di Noto, M. Doser, A. Dudarev, A. Ereditato, C. Evans, R. Ferragut, J. Fesel, A. Fontana, S. Gerber, M. Giammarchi, A. Gligorova, F. Guatieri, S. Haider, H. Holmestad, T. Huse, E. Jordan, M. Kimura, T. Koettig, D. Krasnický, V. Lagomarsino, P. Lansonneur, P. Lebrun, S. Lehner, J. Liberadzka, C. Malbrunot, S. Mariazzi, V. Matveev, Z. Mazzotta, G. Nebbia, P. Nédélec, M. Oberthaler, N. Pacifico, D. Pagano, L. Penasa, V. Petrácek, C. Pistillo, F. Prelz, M. Prevedelli, L. Ravelli, B. Rienäcker, O. Røhne, A. Rotondi, M. Sacerdoti, H. Sandaker, R. Santoro, P. Scampoli, L. Smestad, F. Sorrentino, M. Spacek, J. Storey, I. Strojek, G. Testera, I. Tietje, E. Widmann, P. Yzombard, S. Zavatarelli, J. Zmeskal, N. Zurlo, and AEGIS Collaboration (2016). "Probing antimatter gravity — The AEGIS experiment at CERN". In: *EPJ Web of Conferences* 126, p. 02016. DOI: 10.1051/epjconf/201612602016.

Kellerbauer, A., M. Amoretti, A. Belov, G. Bonomi, I. Boscolo, R. Brusa, M. Büchner, V. Byakov, L. Cabaret, C. Canali, C. Carraro, F. Castelli, S. Cialdi, M. de Combarieu, D. Comparat, G. Consolati, N. Djourelov, M. Doser, G. Drobychev, A. Dupasquier, G. Ferrari, P. Forget, L. Formaro, A. Gervasini, M. Giammarchi, S. Gninenko, G. Gribakin, S. Hogan, M. Jacquey, V. Lagomarsino, G. Manuzio, S. Mariazzi, V. Matveev, J. Meier, F. Merkt, P. Nedelec, M. Oberthaler, P. Pari, M. Prevedelli, F. Quasso, A. Rotondi, D. Sillou, S. Stepanov, H. Stroke, G. Testera, G. Tino, G. Trénec, A. Vairo, J. Vigué, H. Walters, U. Warring, S. Zavatarelli, and D. Zvezhinskij (2008). "Proposed antimatter gravity measurement with an antihydrogen beam". In: *Nuclear*

Instruments and Methods in Physics Research, Section B 266.3, pp. 351–356. DOI: 10.1016/j.nimb.2007.12.010.

Kellerbauer, A. and J. Walz (2006). "A novel cooling scheme for antiprotons". In: *New Journal of Physics* 8.45, pp. 1–9. DOI: 10.1088/1367-2630/8/3/045.

Knapp, M., O. Echt, D. Kreisle, T. D. Märk, and E. Recknagel (1986). "Formation of long–lived CO_2^-, N_2O^-, and their dimer anions, by electron attachment to van der waals clusters". In: *Chemical Physics Letters* 126.3,4, pp. 225–231. DOI: 10.1016/S0009-2614(86)80074-4.

Knoop, M., N. Madsen, and R. C. Thompson (2014). *Physics with trapped charged particles*. London: Imperial College Press.

Kogelschatz, U. (2003). "Dielectric–barrier Discharges: Their History, Discharge Physics, and Industrial Applications". In: *Plasma Chemistry and Plasma Processing* 23.1, pp. 1–46. DOI: 10.1023/A:1022470901385.

Landau, L. D. and E. M. Lifshitz (1976). *Mechanics*. Oxford New York: Pergamon Press.

Lefebvre-Brion, H. and R. W. Field (2004). *The Spectra and Dynamics of Diatomic Molecules*. Elsevier Academic Press. DOI: 10.1016/B978-0-12-441455-6.X5000-8.

Leopold, D. G., K. K. Murray, A. E. S. Miller, and W. C. Lineberger (1985). "Methylene: A study of the $\tilde{X}\,^3B_1$ and $\tilde{a}\,^1A_1$ states by photoelectron spectroscopy of CH_2^- and CD_2^-". In: *The Journal of Chemical Physics* 83.10, pp. 4849–4865. DOI: 10.1063/1.449746.

Lineberger, W. C. and T. A. Patterson (1972). "Two photon photodetachment spectroscopy: The C_2^- $^2\Sigma$ states". In: *Chemical Physics Letters* 13.1, pp. 40–44. DOI: 10.1016/0009-2614(72)80037-X.

Loudon, R. (2000). *The Quantum Theory of Light*. 3rd ed. Oxford University Press, p. 450.

Lu, Y.-J., J. H. Lehman, and W. C. Lineberger (2015). "A versatile, pulsed anion source utilizing plasma–entrainment: Characterization and applications". In: *The Journal of Chemical Physics* 142.4, p. 44201. DOI: 10.1063/1.4906300.

Luria, K., W. Christen, and U. Even (2011). "Generation and Propagation of Intense Supersonic Beams". In: *Journal of Physical Chemistry A* 115, pp. 7362–7367. DOI: 10.1021/jp201342u.

Luria, K., N. Lavie, and U. Even (2009). "Dielectric barrier discharge source for supersonic beams". In: *Review of Scientific Instruments* 80.10, p. 104102. DOI: 10.1063/1.3244085.

Lykke, K. R., K. K. Murray, and W. C. Lineberger (1991). "Threshold photodetachment of H^-". In: *Physical Review A* 43.11, pp. 6104–6107. DOI: 10.1103/PhysRevA.43.6104.

Madsen, N. (2018). "Antiproton physics in the ELENA era". In: *Philosophical Transactions of the Royal Society A* 376, p. 20170278. DOI: 10.1098/rsta.2017.0278.

Major, F. G., V. N. Gheorghe, and G. Werth (2005). *Charged particle traps : physics and techniques of charged particle field confinement*. Berlin New York: Springer-Verlag Berlin Heidelberg, p. 356. DOI: 10.1007/b137836.

Mead, R. D., U. Hefter, P. A. Schulz, and W. C. Lineberger (1985). "Ultrahigh resolution spectroscopy of C_2^-: The $A\,^2\Pi_u$ state characterized by deperturbation methods". In: *The Journal of Chemical Physics* 82.4, pp. 1723–1731. DOI: 10.1063/1.448960.

Neuhauser, W., M. Hohenstatt, P. Toschek, and H. Dehmelt (1978). "Optical–Sideband Cooling of Visible Atom Cloud Confined in Parabolic Well". In: *Physical Review Letters* 41.4, pp. 233–236. DOI: 10.1103/PhysRevLett.41.233.

O'Malley, S. M. and D. R. Beck (2010). "Lifetimes and branching ratios of excited states in La^-, Os^-, Lu^-, Lr^-, and Pr^-". In: *Physical Review A* 81.3, p. 032503. DOI: 10.1103/PhysRevA.81.032503.

Osborn, D. L., D. J. Leahy, D. R. Cyr, and D. M. Neumark (1996). "Photodissociation spectroscopy and dynamics of the $N_2O_2^-$ anion". In: *The Journal of Chemical Physics* 104.13, pp. 5026–5039. DOI: 10.1063/1.471132.

Pegg, D. J. (2004). "Structure and dynamics of negative ions". In: *Reports on Progress in Physics* 67.6, pp. 857–905. DOI: 10.1088/0034-4885/67/6/R02.

Perez, P. and Y. Sacquin (2012). "The GBAR experiment: gravitational behaviour of antihydrogen at rest". In: *Classical and Quantum Gravity* 29.18, p. 184008. DOI: 10.1088/0264-9381/29/18/184008.

Phillips, W. D. (1998). "Laser cooling and trapping of neutral atoms". In: *Reviews of Modern Physics* 70.3, pp. 721–741. DOI: 10.1103/RevModPhys.70.721.

Refaey, K. M. A. and J. L. Franklin (1976). "Endoergic ion–molecule–collision processes of negative ions. III. Collisions of I^- on O_2, CO, and CO_2". In: *International Journal of Mass Spectrometry and Ion Physics* 20, pp. 19–32. DOI: 10.1016/0020-7381(76)80029-0.

Rehfuss, B. D., D.-J. Liu, B. M. Dinelli, M.-F. Jagod, W. C. Ho, M. W. Crofton, and T. Oka (1988). "Infrared spectroscopy of carbo–ions. IV. The $A\,^2\Pi_u - X\,^2\Sigma_g^+$ electronic transition of C_2^-". In: *The Journal of Chemical Physics* 89.1, pp. 129–137. DOI: 10.1063/1.455731.

Rienstra-Kiracofe, J. C., G. S. Tschumper, H. F. F Schaefer, S. Nandi, and G. B. Ellison (2002). "Atomic and Molecular Electron Affinities: Photoelectron Experiments and Theoretical Computations". In: *Chemical reviews* 102, pp. 231–282. DOI: 10.1021/cr990044u.

Rolston, S. L. and G. Gabrielse (1989). "Cooling antiprotons in an ion trap". In: *Hyperfine Interactions* 44, pp. 233–246. DOI: 10.1007/BF02398673.

Rosmus, P. and H.-J. Werner (1984). "Multireference–CI calculations of radiative transition probabilities in C_2^-". In: *The Journal of Chemical Physics* 80.10, p. 5085. DOI: 10.1063/1.446579.

Royen, P. and M. Zackrisson (1992). "Spin–Splitting Analysis of the $B\,^2\Sigma_u^+(v=0)$ State of C_2^-, Using Velocity Modulation Laser Spectroscopy". In: *Journal of Molecular Spectroscopy* 155.2, pp. 427–429. DOI: 10.1016/0022-2852(92)90534-U.

Schendler, T. and H.-P. Schulze (1990). "Stabilitätsgrenzdrücke von Acetylen/Gas–Gemischen". In: *Chemie Ingenieur Technik* 62.1, pp. 41–43. DOI: 10.1002/cite.330620111.

Šedivcová, T. and V. Špirko (2006). "Potential energy and transition dipole moment functions of C_2^-". In: *Molecular Physics* 104.13-14, pp. 1999–2005. DOI: 10.1080/00268970600662689.

Sellner, S., M. Besirli, M. Bohman, M. J. Borchert, J. Harrington, T. Higuchi, A. Mooser, H. Nagahama, G. Schneider, C. Smorra, T. Tanaka, K. Blaum, Y. Matsuda, C. Os-

pelkaus, W. Quint, J. Walz, Y. Yamazaki, and S. Ulmer (2017). "Improved limit on the directly measured antiproton lifetime". In: *New Journal of Physics* 19.8, p. 083023. DOI: 10.1088/1367-2630/aa7e73.

Shan-Shan, Y., Y. Xiao-Hua, L. Ben-Xia, K. Kakule, W. Sheng-Hai, G. Ying-Chun, L. Yu-Yan, and C. Yang-Quin (2003). "Study of hot bands in the $B\,^2\Sigma_u^+ - X\,^2\Sigma_g^+$ system of C_2^- anion". In: *Chinese Physics* 12.7, pp. 745–749. DOI: 10.1088/1009-1963/12/7/308.

Shuman, E. S., J. F. Barry, and D. DeMille (2010). "Laser cooling of a diatomic molecule". In: *Nature* 467, pp. 820–823. DOI: 10.1038/nature09443.

Smith, J. R., J. B. Kim, and W. C. Lineberger (1997). "High–resolution threshold photodetachment spectroscopy of OH^-". In: *Physical Review A* 55.3, pp. 2036–2043. DOI: 10.1103/PhysRevA.55.2036.

Smorra, C., S. Sellner, M. J. Borchert, J. A. Harrington, T. Higuchi, H. Nagahama, T. Tanaka, A. Mooser, G. Schneider, M. Bohman, K. Blaum, Y. Matsuda, C. Ospelkaus, W. Quint, J. Walz, Y. Yamazaki, and S. Ulmer (2017). "A parts–per–billion measurement of the antiproton magnetic moment". In: *Nature* 550, p. 371. DOI: 10.1038/nature24048.

Steele, D., E. R. Lippincott, and J. T. Vanderslice (1962). "Comparative Study of Empirical Internuclear Potential Functions". In: *Reviews of Modern Physics* 34.2, pp. 239–251. DOI: 10.1103/RevModPhys.34.239.

Storry, C. H., A. Speck, D. L. Sage, N. Guise, G. Gabrielse, D. Grzonka, W. Oelert, G. Schepers, T. Sefzick, H. Pittner, M. Herrmann, J. Walz, T. W. Hänsch, D. Comeau, and E. A. Hessels (2004). "First Laser–Controlled Antihydrogen Production". In: *Physical Review Letters* 93.26, p. 263401. DOI: 10.1103/PhysRevLett.93.263401.

Thyagaraja, A. and K. G. McClements (2009). "Plasma physics in noninertial frames". In: *Physics of Plasmas* 16, p. 92506. DOI: 10.1063/1.3238485.

Ulmer, S., C. Smorra, A. Mooser, K. Franke, H. Nagahama, G. Schneider, T. Higuchi, S. Van Gorp, K. Blaum, Y. Matsuda, W. Quint, J. Walz, and Y. Yamazaki (2015). "High–precision comparison of the antiproton–to–proton charge–to–mass ratio". In: *Nature* 524, pp. 196–199. DOI: 10.1038/nature14861.

Van Gorp, S., M. Beck, M. Breitenfeldt, V. De Leebeeck, P. Friedag, A. Herlert, T. Iitaka, J. Mader, V. Kozlov, S. Roccia, G. Soti, M. Tandecki, E. Traykov, F. Wauters, C. Weinheimer, D. Zákoucký, and N. Severijns (2011). "Simbuca, using a graphics card to simulate Coulomb interactions in a penning trap". In: *Nuclear Instruments and Methods in Physics Research, Section A* 638.1, pp. 192–200. DOI: 10.1016/j.nima.2010.11.032.

Van Gorp, S. and P. Dupre (2013). "Improvements to the Simbuca trapped charged-particle simulation program". In: *AIP Conference Proceedings*. Vol. 1521. May, pp. 300–308. DOI: 10.1063/1.4796087.

Vanderslice, J. T., E. A. Mason, W. G. Maisch, and E. R. Lippincott (1959). "Ground State of Hydrogen by the Rydberg–Klein–Rees Method". In: *Journal of Molecular Spectroscopy* 3, pp. 17–29. DOI: 10.1016/0022-2852(59)90003-7.

Vargas, A. J. (2018). “Prospects for testing Lorentz and CPT symmetry with antiprotons”. In: *Philosophical Transactions of the Royal Society A* 376, p. 20170276. DOI: 10.1098/rsta.2017.0276.

Varshni, Y. P. (1957). “Comparative Study of Potential Energy Functions for Diatomic Molecules”. In: *Reviews of Modern Physics* 29.4, pp. 664–682. DOI: 10.1103/RevModPhys.29.664.

Walter, C. W., N. D. Gibson, Y.-G. Li, D. J. Matyas, R. M. Alton, S. E. Lou, R. L. Field III, D. Hanstorp, L. Pan, and D. R. Beck (2011). “Experimental and theoretical study of bound and quasibound states of Ce^-”. In: *Physical Review A* 84.3, p. 032514. DOI: 10.1103/PhysRevA.84.032514.

Walter, C. W., N. D. Gibson, D. J. Matyas, C. Crocker, K. A. Dungan, B. R. Matola, and J. Rohlén (2014). “Candidate for Laser Cooling of a Negative Ion: Observations of Bound-Bound Transitions in La^-”. In: *Physical Review Letters* 113.6, p. 063001. DOI: 10.1103/PhysRevLett.113.063001.

Walz, J., S. B. Ross, C. Zimmermann, L. Ricci, M. Prevedelli, and T. W. Hänsch (1995). “Combined Trap with the Potential for Antihydrogen Production”. In: *Physical Review Letters* 75.18, pp. 3257–3260. DOI: 10.1103/PhysRevLett.75.3257.

Wang, R., Y. Chen, P. Cai, J. Lu, Z. Bi, X. Yang, and L. Ma (1999). “Optical heterodyne velocity modulation spectroscopy enhanced by a magnetic rotation effect”. In: *Chemical Physics Letters* 307.5, pp. 339–342. DOI: 10.1016/S0009-2614(99)00562-X.

Warring, U., M. Amoretti, C. Canali, A. Fischer, R. Heyne, J. O. Meier, C. Morhard, and A. Kellerbauer (2009). “High–Resolution Laser Spectroscopy on the Negative Osmium Ion”. In: *Physical Review Letters* 102.4, p. 043001. DOI: 10.1103/PhysRevLett.102.043001.

Western, C. M. (2017). “PGOPHER: A program for simulating rotational, vibrational and electronic spectra”. In: *Journal of Quantitative Spectroscopy & Radiative Transfer* 186, pp. 221–242. DOI: 10.1016/j.jqsrt.2016.04.010.

Wineland, D. J., R. E. Drullinger, and F. L. Walls (1978). “Radiation–Pressure Cooling of Bound Resonant Absorbers”. In: *Physical Review Letters* 40.25, pp. 1639–1642. DOI: 10.1103/PhysRevLett.40.1639.

Wolfram Alpha LLC (2017). *Wolfram|Alpha*. URL: https://www.wolframalpha.com/ (visited on 04/22/2018).

Yzombard, P., M. Hamamda, S. Gerber, M. Doser, and D. Comparat (2015). “Laser Cooling of Molecular Anions”. In: *Physical Review Letters* 114.21, p. 213001. DOI: 10.1103/PhysRevLett.114.213001.

Zavitsas, A. A. (1991). “Energy–Distance Relationship in Chemical Bonding. Accurate Calculation of Potential Energy Curves”. In: *Journal of the American Chemical Society* 113.13, pp. 4755–4767. DOI: 10.1021/ja00013a008.

Zhelyazkova, V., A. Cournol, T. E. Wall, A. Matsushima, J. J. Hudson, E. A. Hinds, M. R. Tarbutt, and B. E. Sauer (2014). “Laser cooling and slowing of CaF molecules”. In: *Physical Review A* 89.5, pp. 2–6. DOI: 10.1103/PhysRevA.89.053416.

Zhou, J., E. Garand, and D. M. Neumark (2007). “Vibronic structure in C_2H and C_2D from anion slow electron velocity–map imaging spectroscopy”. In: *The Journal of Chemical Physics* 127.11, p. 114313. DOI: 10.1063/1.2768932.